

Graphene: Elastic properties, signatures of criticality induced by zero modes and multifractality near a quantum Hall transition

Zur Erlangung des akademischen Grades eines
DOKTORS DER NATURWISSENSCHAFTEN
von der Fakultät für Physik des
Karlsruher Instituts für Technologie

genehmigte

DISSERTATION

von

MSc. Soumya Bera

aus Garbeta, Indien

Tag der mündl. Prüfung: 24. Juni 2011

Referent: Prof. (apl.) Dr. Ferdinand Evers

Korreferent: Prof. Dr. Alexander Shnirman

to my mother

“How many roads a man must cross before you call him a man”

Contents

List of Figures	ix
List of Tables	xi
1 Introduction	1
1.1 Graphene: Electronic properties	3
1.1.1 Strain effects	6
1.1.2 Edge effects	7
1.2 Transport properties	8
1.2.1 Ballistic graphene	9
1.2.2 Disorder in graphene	11
1.2.2.1 Weak anti-localization	12
1.2.2.2 Disorder preserving chiral symmetry	15
1.2.3 Half-integer quantum Hall effect	16
1.2.3.1 Critical fluctuations of wavefunctions: Multifractality	18
1.2.3.2 Interaction effects	21
1.3 Fabrication methods	23
1.4 Overview of the thesis	24
2 Elastic properties of graphene flakes	27
2.1 Phenomenological theory of elasticity in graphene	29
2.1.1 Ground state energy	29
2.1.2 Phenomenological parameters	31
2.1.2.1 Isotropic strain	31
2.1.2.2 Shear Strain	33
2.2 Model and Method	34
2.3 Result: Phenomenological parameters of bulk graphene	35
2.3.1 Isotropic strain	35
2.3.2 Shear strain	42
2.3.3 Summary and Outlook	42
2.4 Result: Flake elastic properties	43
2.4.1 Homogeneous isotropic strain	44
2.4.2 Shear strain	45
2.4.3 Buckling induced strain	46
2.4.4 Summary and Outlook	48
2.5 Zero point motion	50

2.5.1	DFT calculations of Grüneisen parameters	52
2.5.2	Results and Discussion	53
2.5.3	Summary and Outlook	55
3	Graphene: Zero Modes and Transport	57
3.1	Electronic properties of vacancies	58
3.2	Density of States	61
3.2.1	Method	62
3.2.2	Clean graphene	64
3.2.3	Graphene with vacancy	65
3.2.4	Summary and Outlook	69
3.3	Transport properties of graphene with vacancies	70
3.3.1	Theoretical model and method	70
3.3.2	Result and discussion	71
3.3.3	Summary and Outlook	77
4	Integer Quantum Hall Transition: Interaction Effect	79
4.1	Experimental results	80
4.2	Analytical considerations	81
4.2.1	Dephasing length and short range interaction	83
4.3	The network model at the IQH critical point	83
4.3.1	Percolation picture	84
4.3.2	Network model	86
4.3.3	Method	87
4.4	Results and discussions	88
4.4.1	First order correction	88
4.4.2	Second order correction	90
4.4.3	Discussions	93
4.5	Summary and Outlook	93
5	Conclusion	95
A	Symmetry classification of disordered metals	99
A.1	Symmetry classification scheme	100
A.1.1	Wigner-Dyson classes	100
A.1.2	Chiral classes	100
A.1.3	Bogoliubov-de Gennes classes	101
A.2	Importance of the symmetry classifications	102
A.3	Symmetries in clean graphene	105
B	Density Functional Theory	107
B.1	Kohn-Sham formalism in a nutshell	108
B.1.1	Local density approximation	109
B.1.2	Generalized gradient approximation	110
B.1.3	Hybrid Functionals	111

C	Theory of transport in disordered graphene	113
C.1	Model and Method	113
D	Calculation of the dephasing rate	117
D.1	Model Hamiltonian	117
D.2	First order correction to the thermodynamic potential	118
D.3	Second order correction to the self-energy: Dephasing rate	120
E	Numerical implementation of the network model	123
E.1	Parallelization procedure	123
E.1.1	Parallelization of the disorder averaging	124
E.1.2	Parallelization of the linear solver	124
E.1.3	Simulation protocol and parameters	125
E.2	Computational performance	125
E.3	Summary and Outlook	127
	Bibliography	129

List of Figures

1.1	The two dimensional hexagonal lattice structure of graphene	3
1.2	Band structure of graphene as obtained within the tight binding approximation	5
1.3	Stereographic plot of the STM image of a corrugated graphene surface	6
1.4	Experimental verification of the ballistic conductivity	9
1.5	Experimental observation of the minimal conductivity of graphene .	10
1.6	Color map of spatial density variation of a graphene flakes	11
1.7	Numerical observation of the anti-localization and one parameter scaling in graphene	13
1.8	Schematic drawing of the β -function in two-dimensional disordered system	14
1.9	Schematic view of the Landau level structure in single layer graphene	17
1.10	Multifractal wavefunction	19
1.11	Scaling of the integer quantum Hall plateaus	22
1.12	AFM images of graphene flakes	23
2.1	Geometry of the $N \times N$ hydrogenated graphene flakes	28
2.2	Schematic view of applied strain in graphene	33
2.3	Bulk, surface and corner free energy of graphene flakes using DFT .	35
2.4	Dependency of the amplitudes $\phi^{i,e}$ describing the corrections in $1/N_{e,i}$ to the binding energy	37
2.5	Bulk, surface and corner free energy as a sum of atomic energy . . .	38
2.6	Change in the edge energy (E_{edge}) when applying homogenous, isotropic strain (ε) in graphene flakes	40
2.7	Change in the energy when applying a shear strain in graphene flakes	41
2.8	Flow of the excess energy generated by changing the bond length (isotropic strain)	43
2.9	Estimation of the sum of the Lamé parameters and finite size correction	44
2.10	Estimate for Lamé parameter μ_{el} determined from the excess energy	45
2.11	Buckling flakes of $N=5, 6$ with different central configurations of carbon atoms	47
2.12	Estimating the Lamé parameter κ determined from the excess energy ΔE of a bulging flake	48
2.13	Dependency of work-function on isotropic strain	50
2.14	Dependency of ΔF_{vib} on isotropic strain for system size $N=6$	52

2.15	Schematic diagram of vibrating modes that give rise to D(left) and G(right) peaks in Raman spectra of graphene.	53
2.16	Phonon density of states and flow of D-peak with in-plane strain in graphene	54
3.1	Pictorial representation of a vacancy in a graphene lattice	60
3.2	Phase diagram of the Cho-Fisher model	62
3.3	Density of states of a clean graphene lattice	64
3.4	DoS in the presence of vacancies	66
3.5	Evolution of zero-modes and sub-gap with vacancy concentrations	67
3.6	Flow of the eigenvalues in the presence of vacancies on one sub-lattice	68
3.7	DoS in the presence of vacancies	69
3.8	Ballistic sample used in transport calculation	71
3.9	Conductance distribution function at low concentration of vacancies	73
3.10	Conductance distribution function at high concentration of vacancy	74
3.11	Scaling of variance and mean value of conductivity	75
3.12	Dependence of mean conductivity with vacancy concentrations	76
4.1	Different experimental values of κ	80
4.2	Random potential landscape	84
4.3	Chalker-Coddington Network model	86
4.4	Scaling of the Hartree-Fock correction	88
4.5	Scaling of the correlation function \mathcal{K}_1	89
4.6	Scaling of the correlation function \mathcal{K}_2 as function of $1/R^2$	90
4.7	Scaling behavior of \mathcal{K}_2 as function of R/N for fixed different values of ρ/R	91
4.8	Scaling behavior of $(\rho/R)^{-2\mu_2}\mathcal{K}_2$ as function of R/N and the single parameter scaling curve	92
D.1	Feynman diagram for Hartree-Fock correction	118
D.2	Feynman diagrams for second order self energy correction	120
E.1	Speed up measurement of disorder averaging of CCNM	125
E.2	Benchmarking of the CCNM code	126

List of Tables

1.1	Symmetry classifications of disordered graphene	12
2.1	Survey of the minimum C-C bond lengths in graphene flakes	36
2.2	Phenomenological parameters for bulk energy	36
2.3	Phenomenological parameters for edge coefficients	36
2.4	Survey over the fitted total energy parameters and edge energy	39
2.5	Bulk and surface shear energy coefficients	42
2.6	Comparison of C-C-bond distance in bulk graphene, elastic constants , Poisson ratio and Young's modulus	46
2.7	Survey over the fitted Grüneisen parameters	53
A.1	Symmetry classifications of disordered systems	101

1

CHAPTER 1

Introduction

Graphene, a one atom thick sheet of carbon, has the reputation of being one of the most promising materials in the 21st century. This fact has been emphasized to a great extent by the Royal Swedish Academy of Sciences awarding the Nobel Prize in Physics to Andre Geim and Konstantin Novoselov “*for ground breaking experiments regarding the two-dimensional material graphene*” in 2010. Although earlier studies of graphene date back as far as 1859 to D. C. Brodie in the context of reduced graphite oxide, the fabrication of graphene as experimental and applied devices on a proper substrate was due to Geim and Novoselov in 2004[1]. Since then graphene has become the rising star in the field of material science, mesoscopic physics, and in general condensed matter physics during the second half of the last decade [1–6]. Not only from the perspective of experiments and applications, but also in view of fundamental physics graphene has been an important material from early on. Unlike in a two-dimensional electron gas, the low energy excitations in graphene follow a Dirac type dispersion relation. Among several other consequences this peculiar band structure has led to the observation of quantum relativistic phenomena in everyday tabletop experiments.

Producing a high quality large graphene sample has been one of the most challenging problem in recent experiments. For instance, certain experimental developments show that free standing graphene on a scaffold in vacuum or on a substrate shows surface corrugation even at relatively low temperature [7–9]. Their origin is thought to be due to the residual strain originating from experimental techniques. Strain can have various consequences on the electronic structure; for example calculations suggest that the isotropic strain displace the Dirac cone (\mathbf{K} point) along the ΓK line towards the $\Gamma(K = 0)$ point of the Brillouin zone of graphene [10]. It has also been proposed that in contrast to isotropic strain, an asymmetrical strain distribution in graphene can open up a gap exactly at the Fermi energy [11]. Consequently, an increased interest in the elastic properties of graphene has recently developed. Moreover, in experiments graphene samples are finite (*flakes*) with

edges that break the symmetry of the bulk. In particular, theoretical calculations show that the zigzag edges of graphene nano-ribbons (quasi 1d) introduce two flat bands at the Fermi energy, which induce magnetism. For elastic properties, also edge effects can be highly relevant. Hence studies of *flake* elastic properties are interesting in their own right. In the first part of the thesis, we investigate the interplay between edge and strain in finite size graphene flakes based on a phenomenological theory and density functional theory calculations including phonon effects.

Recently, experimental investigations aim to produce high carrier mobility graphene sample for future electronic devices. However, there are several possible candidates that act as a scattering center: ripple, ad-atoms, vacancies, different edge structures, topological lattice defects, cracks, strain, self-doping, to name a few. Among these, vacancies (or missing carbon atoms) in graphene, which often appear in sample preparation processes [12], play an important role in the transport properties at the Fermi energy. A single vacancy creates a “mid-gap” state exactly at the Dirac point. It has been shown that each vacancy enhances the ballistic conductivity by a value of the order of e^2/h . However, in experiments a finite concentration of vacancies is present that forms a narrow impurity band. Thus understanding the effects of such a narrow band in transport experiments are of fundamental importance. Our numerical investigation based on the full-counting statistics shows that with an increasing number of vacancies the ballistic conductivity increases, reaching a maximum value beyond which it starts to decrease until it eventually reaches zero in the percolation limit.

Our previous study indicates that in order to comprehend the effect of defects in transport experiments, it is necessary to consider more than one vacancies. Because at a finite concentration of vacancies electronic states form a complicated interference pattern that leads to the localization phenomenon. In the presence of a strong magnetic field such effects manifest themselves in the quantum Hall effect (QHE). Although, many aspects of the QHE were understood in the framework of a single particle picture, understanding the effect of the electron-electron interaction on the quantum Hall transition still poses a considerable amount of challenge. In this thesis we will consider the effect of dephasing, governed by the inelastic processes of electron scattering, on a quantum Hall critical point at finite temperature, T . In a usual two-dimensional electron gas the finite range interaction is irrelevant in a renormalization group sense; since, the interaction strength, λ , scales as $\lambda \propto L^{-\mu_2}$, where $\mu_2 > 0$ is the scaling dimension and L is the length of the sample. However the interaction can not be fully discarded as it generates a non-zero critical value of the longitudinal conductivity, σ_{xx} , and determines the nature of temperature and frequency scaling near the quantum Hall critical point. We will use a numerical approach to calculate the critical exponent μ_2 and then address the issue of the effect of finite range electron-electron interaction– which is a very generic feature of any quantum Hall critical point– on the integer quantum Hall transition as observed in a usual two-dimensional disordered metals.

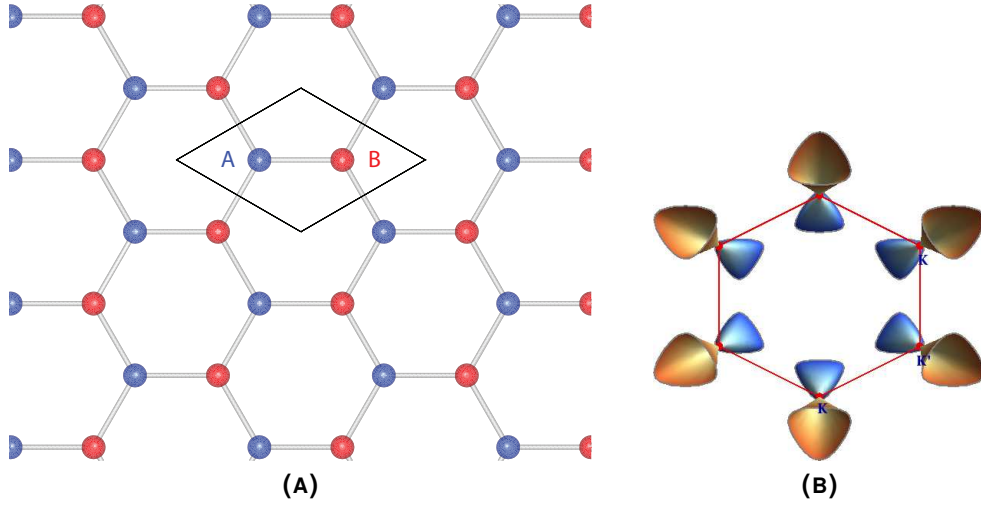


FIGURE 1.1: (A) A section of the two dimensional hexagonal graphene lattice structure. The closed region shows the two crystallographically different carbon atoms known as *A* (blue circle) and *B* (red circle) sub-lattices, respectively. (B) Shows the Brillouin zone of the graphene lattice with two inequivalent *K* points around which the energy dispersion becomes linear.

In the following sections we will provide a detailed introduction in the state of the art of the research in graphene related to this thesis.

1.1 Graphene: Electronic properties

Graphene is a two-dimensional sheet of carbon atoms arranged in a honeycomb lattice. The honeycomb lattice consists of two non-equivalent sub-lattices (see Fig. 1.1) denoted as *A* and *B*. It can be viewed as a triangular lattice with a basis of two carbon atoms per unit cell. The unit vectors are then given by [3],

$$\mathbf{a}_1 = \frac{a}{2}(3, \sqrt{3}); \quad \mathbf{a}_2 = \frac{a}{2}(3, -\sqrt{3}) \quad (1.1)$$

where $a = 1.42 \text{ \AA}$ is the lattice constant of the hexagonal lattice. The reciprocal lattice vector is defined with respect to the triangular lattice,

$$\mathbf{b}_1 = \frac{2\pi}{3a}(1, \sqrt{3}); \quad \mathbf{b}_2 = \frac{2\pi}{3a}(1, -\sqrt{3}). \quad (1.2)$$

The first Brillouin zone (BZ) contains two inequivalent points in reciprocal space which are particularly important for the low energy properties of graphene. These two points, denoted as \mathbf{K} and \mathbf{K}' , are known as the Dirac points,

$$\mathbf{K} = \left(\frac{2\pi}{3a}, \frac{2\pi}{3\sqrt{3}a} \right); \quad \mathbf{K}' = \left(\frac{2\pi}{3a}, -\frac{2\pi}{3\sqrt{3}a} \right). \quad (1.3)$$

The low energy physics of graphene is centered around those Dirac points in BZ; they play an important role in the transport properties of graphene which we will discuss in subsequent chapters. In order to fully comprehend the Dirac nature of the charge carriers in graphene, it is important to understand the atomic structure and nature of bonding of the carbon atoms in the honeycomb lattice.

Carbon has the atomic number six. Four out of these six electrons are valence electrons that take part in the atomic bonding with neighboring carbon atoms. In a hexagonal lattice carbon atoms are sp^2 hybridized as the three electrons per carbon atom make strong covalent σ -bonds with three neighboring carbon atoms. The other valence electron takes part in the de-localized π -electron clouds above and below the sheet, which are responsible for graphene's linear dispersion. The tight binding model that represents hopping of the π -electrons in a graphene lattice has the form,

$$H = -t \sum_{\langle i,j \rangle} (a_i^\dagger a_j + \text{h.c.}) - t' \sum_{\langle\langle i,j \rangle\rangle} (a_i^\dagger a_j + b_i^\dagger b_j + \text{h.c.}) \quad (1.4)$$

where a_i (a_i^\dagger) is the annihilation (creation) operator that annihilates (creates) an electron at site R_i with t being the hopping amplitude for the nearest neighbor; similarly, t' is the hopping amplitude for next nearest neighbor carbon atom within the same sub-lattices. Accurate band-structure calculations yield a value of $t \simeq -3$ eV for the nearest neighbor hopping amplitude and for the next nearest neighbor $t' \simeq 0.1t$. The band structure of the Hamiltonian, Eq. (1.4), was found to be [13],

$$E_{\pm}(\mathbf{k}) = \pm t \sqrt{3 + f(\mathbf{k})} - t' f(\mathbf{k})$$

$$\text{where, } f(\mathbf{k}) = 2 \cos(\sqrt{3}k_y a) + 4 \cos\left(\frac{\sqrt{3}}{2}k_y a\right) \cos\left(\frac{3}{2}k_x a\right). \quad (1.5)$$

The ' \pm ' sign in Eq. (1.5) represents two energy bands that connect exactly at the Dirac points. The '+' sign refers to the upper (or conduction) band which is known as the π band; similarly, the '-' denotes the lower (or valence band, π^*) of the band-structure of the graphene (see Fig. 1.2). The tight-binding spectrum ($t' = 0$) is symmetric around zero energy signifying the presence of particle-hole symmetry in the system. However, for a finite next nearest neighbor hopping amplitude, t' , the situation changes due to broken particle-hole symmetry. The low energy long wavelength dispersion near the Dirac point including the next nearest neighbor hopping is given by,

$$E_{\pm}(\mathbf{q}) \simeq \pm \hbar v_F |\mathbf{q}| - \frac{9t'a^2}{4} |\mathbf{q}^2| + 3t' \quad (1.6)$$

where \mathbf{q} is the momentum measured relative to the Dirac points and v_F is the energy independent Fermi velocity $v_F = 3ta/2\hbar$, which is 300 times smaller than the

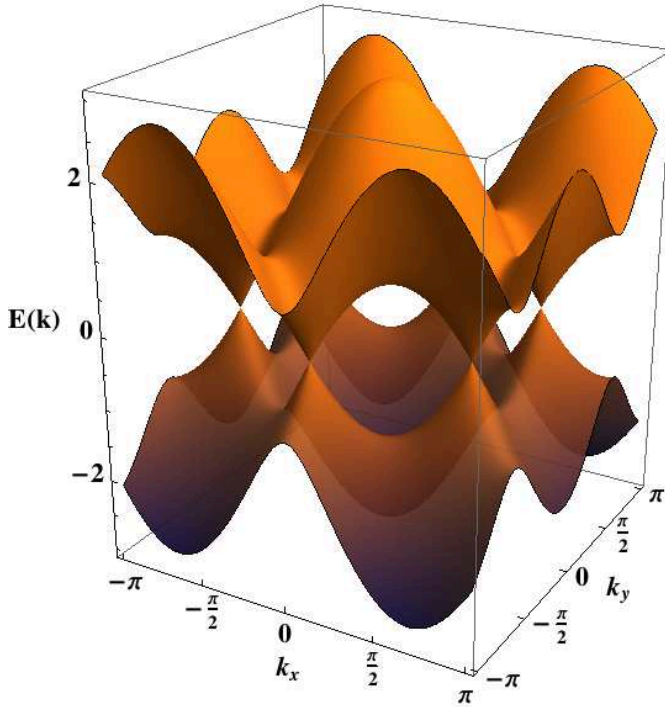


FIGURE 1.2: Band structure of graphene as obtained within the tight binding approximation (Eq. (1.5)) using $t = 1$ and $t' = 0$. The upper band is the conduction band (π^* band); the lower is the valence band (π) that touches with the conduction band exactly at the Dirac points where the dispersion is linear as described in the text. The Fermi level is situated at the point where the conduction band touches the valence band.

velocity of light with a value $\approx 10^6$ m/s. The most interesting part of the energy band structure of graphene lies near the K points, where the energy-momentum relation is linear, $E_{\pm}(\mathbf{q}) = \pm \hbar v_F |\mathbf{q}|$ and is obtained ignoring the next nearest neighbor hopping in Eq. (1.6). Now, following Ref. [3] it is a straight forward exercise to derive the massless relativistic Dirac equation that describes the low energy effective two-dimensional continuum theory for the charge carriers of graphene around each of the K points. In the sub-lattice space it has the form,

$$-i\hbar v_F \begin{pmatrix} 0 & \partial_x - i\partial_y \\ \partial_x + i\partial_y & 0 \end{pmatrix} \begin{pmatrix} \Psi_A \\ \Psi_B \end{pmatrix} = E \begin{pmatrix} \Psi_A \\ \Psi_B \end{pmatrix} \quad (1.7)$$

where, the two components Ψ_A, Ψ_B of the spinor wavefunction represent the wavefunction amplitude at A and B sub-lattices, Fig. 1.1, respectively. In order to differentiate the contribution from K and K' points it is necessary to introduce the iso-spin (or pseudo-spin) quantum number, which can be encoded in the four-dimensional spinor representation of the wavefunction as,

$$\Psi = \begin{pmatrix} \Psi_A^K \\ \Psi_B^K \\ \Psi_A^{K'} \\ \Psi_B^{K'} \end{pmatrix}. \quad (1.8)$$

The existence of the chiral pseudo-spin quantum number is a natural consequence of the graphene lattice structure comprising of two non-equivalent, independent sub-lattices. The complete effective continuum two-dimensional Hamiltonian of

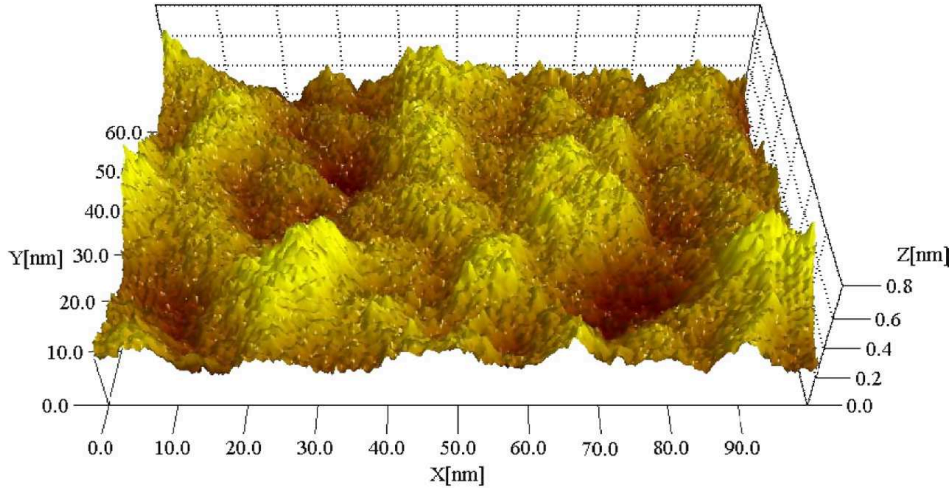


FIGURE 1.3: Stereographic plot of the scanning tunneling microscope (STM) image of a corrugated graphene surface on a silicon dioxide (SiO_2) substrate. Adapted from Ref. [9].

graphene in momentum space is then given by,

$$\begin{aligned}
 H &= v_F(\mathbf{q} \cdot \boldsymbol{\sigma}) \tau_z \\
 &= v_F \begin{pmatrix} 0 & q_x - iq_y & 0 & 0 \\ q_x + iq_y & 0 & 0 & 0 \\ 0 & 0 & 0 & -q_x + iq_y \\ 0 & 0 & -q_x - iq_y & 0 \end{pmatrix} \quad (1.9)
 \end{aligned}$$

where $v_F \mathbf{q}$ is the linear momentum defined with respect to the corner of the BZ and σ , τ_z are the Pauli matrices acting on the AB and KK' subspaces. Note so far the real spins of electrons have been ignored. It would add an extra spinor structure to graphene's wave-functions as it doubles the dimension of the Hamiltonian in Eq. (1.9). Dirac points are special in the BZ of graphene. In a sense that they are “topologically” protected to any small perturbations by the discrete symmetries (spatial inversion and time reversal) of the Hamiltonian (Eq. (1.9)) [14].

1.1.1 Strain effects

Nevertheless perturbations due to some types of disorder, such as topological lattice defects, strain, ripples, exist naturally from experimental preparation techniques. For instance, experiments show surface corrugation or ripple (see Fig. 1.3) in samples of suspended graphene in vacuum [7, 8] or in a substrate [9] or even in samples that are grown on metallic substrates [15]. Their origin is believed to be due to residual strain in the experiments. Importantly, these perturbations act as

an effective gauge field [16] which is related to the strain $(u_{ij})^1$ as,

$$\begin{aligned}\mathcal{A}_x(\mathbf{r}) &= \frac{\beta}{a}(u_{xx}(\mathbf{r}) - u_{yy}(\mathbf{r})) \\ \mathcal{A}_y(\mathbf{r}) &= -2\frac{\beta}{a}u_{xy}(\mathbf{r})\end{aligned}\quad (1.10)$$

where, $\beta \sim -\partial\log(t)/\partial\log(a)$ is a dimensional parameter of order unity and a is the lattice constant. Here we assume the perturbations change slowly on the lattice scale, such that it avoids any inter valley mixing. Consequently, the effective magnetic field induced by the gauge field protects the overall time reversal symmetry of the system because it acquires different sign at the different Dirac points, $\mathcal{A}^{\mathbf{K}}(\mathbf{r}) = -\mathcal{A}^{\mathbf{K}'}(\mathbf{r})$, unlike a real magnetic field; nevertheless, it leads to the Landau quantizations of energy levels and the observation of quantum Hall physics without any external magnetic field [17].

Building a high carrier mobility clean graphene sample, which can be used as a possible electronic device, is still one of the hottest topic in this field of research. However, being a zero-gap semiconductor, graphene can not be used directly as an electronic device, such as a field effect transistor (FET). Among many other possibilities, strain is one of the promising candidates for tuning the band structure at the Fermi energy [18, 19]. In fact, calculations show opening of a band gap at the Dirac points due to an asymmetrical strain (shear strain) distribution in a graphene lattice [11, 17, 20, 21]. Moreover, some external probe such as patterned substrate or clamping (or/and folding) of the sheet allows for the modulation of the intensity of the local strain and thus the band structure. Although many works have been done in strain *engineering* the band structure of graphene, the feasibility of mass production of graphene based electronic devices still remain an open question in the field of research.

1.1.2 Edge effects

While epitaxial methods allow to achieve relatively large clean graphene samples, chemical technologies (e.g. chemical vapor deposition) open up the possibility of mass production of smaller graphene *flakes*. However, in this process the presence of uncontrolled edges has notable consequences in the electronic structure, since the edges encounter a different symmetry structure as opposed to the bulk. For instance, the electronic properties of finite size graphene flakes or ribbons are quite different from its infinite size counterpart. In particular, calculations suggest that zigzag edge terminated graphene nano-ribbons (GNR) have two degenerate flat bands at the Fermi energy, which are localized near the edges (surface states) of

¹In two dimension the strain tensor is defined as, $u_{ij} = \frac{1}{2}\left(\frac{\partial u_i}{\partial x_j} + \frac{\partial u_j}{\partial x_i} + \frac{\partial h}{\partial x_i}\frac{\partial h}{\partial x_j}\right)$, where \mathbf{u} being the two dimensional displacement vector with components u_x, u_y and h denotes the transverse direction of bending of a sheet.

the GNR. Consequently, in these dispersion-less bands, the electrons move slowly, giving rise to an interaction induced instability in the system that eventually leads to magnetism in the zigzag GNR [22–27]. In contrast to zigzag GNR, in certain classes of armchair GNR the electronic spectrum acquires a spectral gap that typically scales with the inverse of the width of the sample, W . Moreover, different edge structures (and terminations) also lead to strain in the system which is reflected via change in the carbon-carbon (C-C) bond distances in the bulk with respect to the edge bonds. Thus an increased interest in the elastic properties of graphene has recently developed.

Although there are many independent studies of edges and strain effects in graphene (or in GNR) [28–30], further study is required to understand the interplay between different edge structures and strain in small graphene flakes. For instance, how different edge terminations systematically modify the *interior* modes of a ribbon or affects the transport properties has remained largely unexplored. More importantly, in order to explore the possibility of an all graphene electronic circuit (graphene electronics) in future applications, further investigations and experiments have to be done.

1.2 Transport properties

Transport measurements are a very unique way of probing the low energy electronic properties of any electronic systems. In graphene, it also plays an important role in determining its unusual band structure and its material quality. For instance, observation of the famous Klein tunneling² [36] was one of the experimental confirmations of the chiral nature of the Dirac particles [3]. The quantum Hall effect also played a similar role in detecting the material quality of graphene and also the unique nature of its charge carriers [37]. To show the theoretical advances

²For relativistic particles the transmission probability, T , through a square potential barrier (V_0) with height larger than the energy of the incoming particle, E , depends weakly on the barrier height; in the limit of infinitely high barrier, the transmission becomes perfect. This is an essential feature in quantum electrodynamics (QED), because the electronic states with positive and negative energies are conjugated and are described by the different components of a single wavefunction. As the charge carriers in graphene follow the Dirac equation it becomes possible to observe Klein tunneling in everyday laboratory experiments [31, 32]. For any such barriers the essential condition to have the Klein tunneling is mode matching [2, 33], i.e. the electron states outside the barrier need to match with the hole states (wavefunctions) inside the barrier. Therefore, the larger the height of the barrier becomes and the better the mode matching between electrons and holes states, the greater the transmission through the barrier. Thus through an infinite barrier the transmission amplitude becomes unity [34]. Moreover, theoretical work suggests for the normal incidence angle of the particle the transmission amplitude through a graphene p-n-p (and p-n) junction is unity [31, 35]. This is because of the absence of pseudo-spin flip processes (i.e. pseudo-spin conservation) in the Dirac fermions. The incoming electron states and the reflected electron states of opposite chirality diminish the probability of reflection at the normal angle, thus resulting in perfect transmission. At other angles of incidence the transmission amplitude in the high barrier limit, $V_0 \gg E$, is

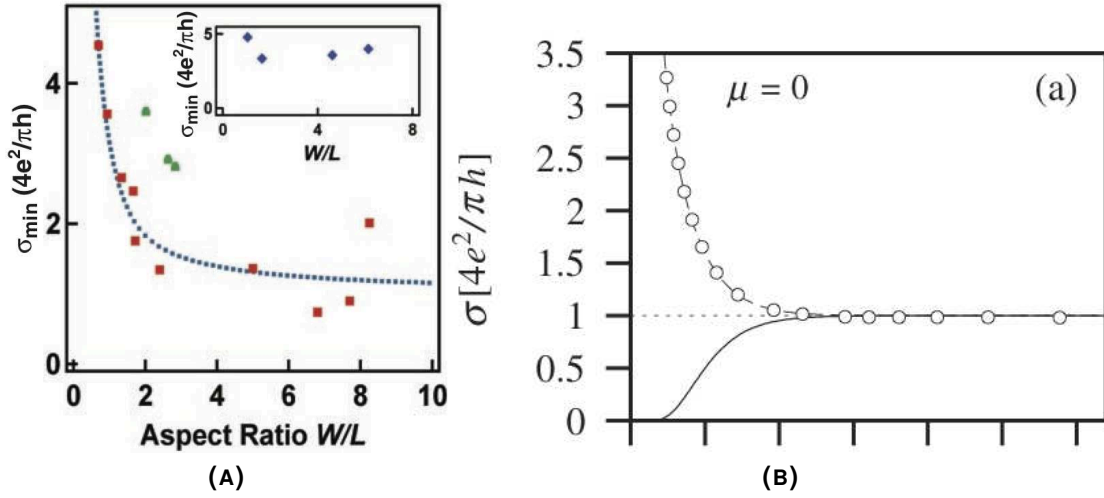


FIGURE 1.4: (A) Experimental verification of the ballistic conductivity with aspect ratio, W/L using a two probe measurement close to Dirac point. For $W/L \gg 1$ the minimal conductivity value approaches $4e^2/\pi h$ as theory predicts in the ballistic regime. Adapted from Ref. [38]. (B) Dependency of graphene minimal conductivity with aspect ratio as seen in a numerical simulation. Again in the large aspect ratio regime the conductivity converges to its minimal value, $4e^2/\pi h$ as mentioned in Eq. (1.12). Adapted from Ref. [39].

made in this field in understanding the low energy physics of graphene, here we will discuss a few of its interesting transport properties that are relevant to this thesis.

1.2.1 Ballistic graphene

The conductivity of a ballistic clean graphene could be understood by considering a specific experimental setup consisting of two leads that are heavily doped, while in the middle the graphene could be doped or pinned at the Dirac point (charge neutrality point). The situation is similar to the one we discuss earlier in the context of the Klein tunneling, where due to chiral nature of the electrons the transmission is always finite at specific angles through a p-n-p or n-n-n junction. Here we will consider a clean graphene sample in the ballistic regime, such that the electron mean free path, l is much larger than the sample length (lead to lead

given by the following asymptotic form of T ,

$$T(\phi) = \frac{\cos^2(\phi)}{1 - \cos^2(q_x D) \sin^2(\phi)} \quad (1.11)$$

where ϕ is the angle of incidence, D is the barrier width. $q_x = \sqrt{(V_0 - E)^2/v_F^2 - k_y^2}$ with k_y being the wave vector component and v_F is the Fermi velocity. So only for certain values of Dq_x , when $Dq_x = n\pi$ with $n \in 0, \pm 1, \pm 2, \dots$, the barrier becomes transparent.

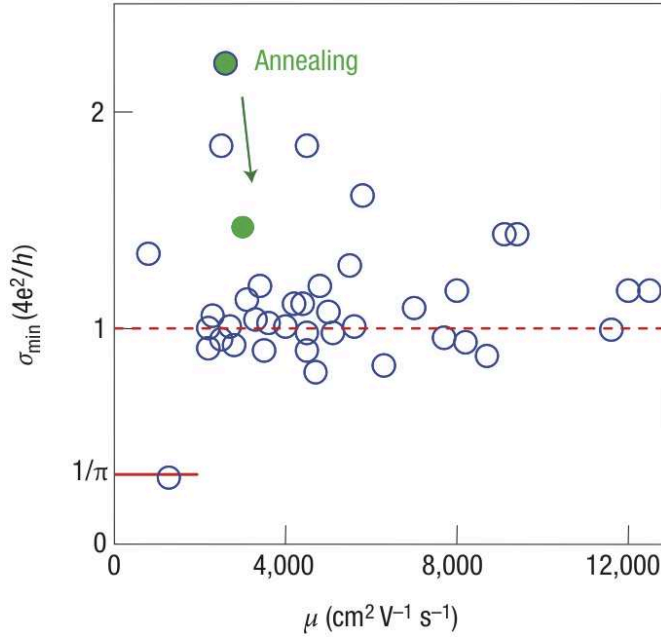


FIGURE 1.5: Experimental observation of the minimal conductivity of graphene. Independent of their carrier mobility, μ , different graphene devices show approximately similar minimal conductivity, $\sim 4e^2/h$, except one low carrier density sample which is rather unusual. It has been proposed that the deviation of the minimal conductivity in low carrier density sample could be due to the charge inhomogeneity at the Dirac point; although it still remains an unsolved mystery. Figure is taken from Ref. [4].

distance), L . Now, by solving the non-interacting Dirac equation in this limit one arrives at the conductivity of this setup, which is given by the evanescent modes, as $\sigma = (L/W)(4e^2/h) \sum_{n=1}^{\infty} T_n$, where $T_n = |1/\cosh(q_n L)|^2$ is the transmission probability with q_n being the transverse wave vector. For a specific boundary condition depicting the two probe measurement setup with highly doped leads, the Landauer conductivity becomes,

$$\sigma = \frac{4e^2}{h} \frac{L}{W} \sum_{n=0}^{\infty} \frac{1}{\cosh^2[\pi(n + 1/2)L/W]} \xrightarrow{W \gg L} \frac{4e^2}{\pi h} \quad (1.12)$$

where W is the width of the sample. In order to derive the above formula we have used the twisted boundary condition as considered in the reference [39], $\Psi(y=0) = \sigma_x \Psi(y=0)$ and $\Psi(y=W) = -\sigma_x \Psi(y=W)$ where σ_x is a component of the Pauli matrix. This particular boundary condition mimics the massless Dirac fermions inside the graphene sample but infinitely massive Dirac fermions in the leads. Now the above formula in the wide sample ($W \gg L$) limit converges to an universal value, $4e^2/\pi h$ which is known as the quantum limited conductivity of the graphene in the clean limit. The limited value of the quantum conductivity has been confirmed by experiments as well as by numerical simulation as shown

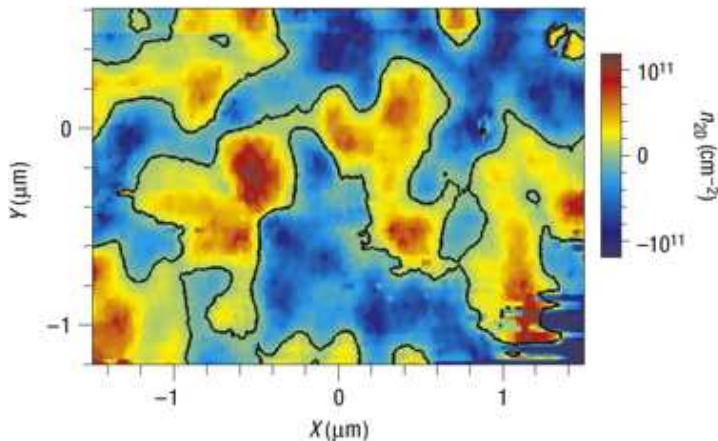


FIGURE 1.6: Color map of spatial density variation of a graphene flakes at charge neutrality point. Blue region corresponds to hole and the red denotes the electrons. The black line corresponds to the zero density contour. Adapted from Ref. [45].

in Fig. 1.4.

It is worth mentioning at this point that a finite impurity concentration changes the situation completely. It has now become clear in the last couple of years that graphene’s minimal conductivity at low carrier density is controlled mostly by the presence of disorder in the sample. For instance experiments (see Fig. 1.5) show a value for the conductivity [34, 39] that is ‘ π ’ times larger than what is usually proposed in several theories [34, 39–41]. The mystery of ‘ π ’ is still in the process of much debate.

There are several predictions for this disagreement over the minimal conductivity in experiments and in theories. One such prediction indicates towards the charge inhomogeneity [42] of the sample at the Dirac point. Charge inhomogeneity plays a significant role in transport [43, 44] because the density fluctuations induced by the electron-hole puddles [45] become much larger than the average charge carrier density, which is similar to the situation of the two-dimensional semiconductor. To summarize, the minimal conductivity of graphene not only depends on the sample geometry but also on the quality of the sample.

Before going in to the details of transport properties in the presence disorder, it will be helpful to understand the consequences of disorder in a general framework of electron systems. Here, we will briefly overview the symmetry classifications of disordered graphene, which will be useful to identify the underlying microscopic model that governs the behavior of the physical observable in transport experiments. For a general symmetry classification scheme of two-dimensional disordered metals please see the Appendix A.

1.2.2 Disorder in graphene

Following the symmetry classification of two-dimensional disordered metals (see Appendix A) the disorder in graphene can also be classified. Here, we will present an almost identical structure as tabulated in Tab. A.1 for possible types of dis-

Disorder	Cartan-nomenclature	Symmetries	Minimal conductivity	con-	Field theory
Vacancies	BDI	C_z, T_0	$\approx 4e^2/\pi h$		Gade
Vacancies+ RMF	AIII	C_z	$\approx 4e^2/\pi h$		Gade
Dislocations	CI	C_0, T_0	$4e^2/\pi h$		Gade
Dislocations+ RMF	AIII	C_0	$4e^2/\pi h$		Gade
Ripple, RMF	2×AIII	Λ_z, C_0	$4e^2/\pi h$		WZW
Charge impurities	2×AII	Λ_z, T_\perp	$(4e^2/\pi h)\ln L$		$\theta = \pi$
Random Dirac mass	2×D	Λ_z, CT_\perp	$4e^2/\pi h$		$\theta = \pi$
Charged impurities + (RMF, ripples)	2×A	Λ_z	$4\sigma_u^*$		$\theta = \pi$

TABLE 1.1: Symmetry classifications of disordered graphene. First column: Possible disorder in graphene. Second column: Cartan nomenclature of the symmetry classes. The factor 2 in the last four rows signifies that in the presence of a specific disorder (long range) the system splits into two copies (decoupled valleys) where each of them shares the same symmetry class. Third column: Presence of the corresponding symmetries (See appendix for terminology). Fourth column: Value of the minimal conductivity, which depends on the presence of a particular symmetry. Fifth column: Associated field theories for different type of disorder model. Adapted from Ref. [46].

order in graphene, which is necessary to identify the localization properties and criticality in such systems.

Although all possible disorder types are listed in Tab. 1.1, some experimental situations allow for the breaking of all imaginable symmetries in graphene. In that case, it has been shown that the RG flow is towards the fixed point of the usual Wigner-Dyson unitary (A) class. In the presence of only TR symmetry the conventional localization of the Wigner-Dyson class (AII) takes place. An interesting situation arises when the chiral symmetry is preserved or the valleys remain decoupled. Here, we will discuss one such situation in the presence of long range disorder in the symplectic class.

1.2.2.1 Weak anti-localization

At sufficiently low temperature and low magnetic field in a usual two-dimensional disordered electron gas, such that the electrons remain coherent over a large part of the sample, quantum interference effects become important. They lead to one of the localization phenomena. The observation of localization relies on the positive interference of two oppositely traversed closed electronic paths, due to which the probability of an electron to go back to its starting point is enhanced. Because of the positive quantum interference of the paths the conductivity decreases and

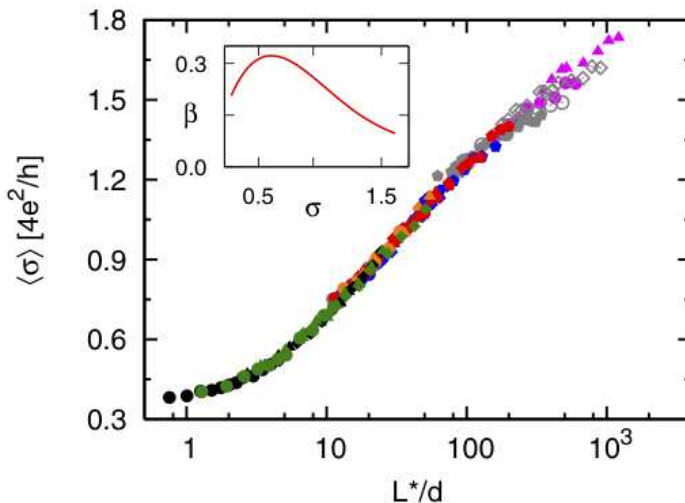


FIGURE 1.7: Numerical observation of the anti-localization and one parameter scaling in graphene at the Dirac point. Main panel shows scaling of conductivity, σ , with effective system size (L^*/d) for different disorder strength (K_0). Data collapsing on a single curve demonstrates the one parameter scaling mentioned in the text. Inner panel shows the resulting β -function. Figure is adapted from Ref. [47].

thus leads to the observation of conventional localization in a normal metal in the unitary (A) or in the orthogonal (AI) symmetry class.

However, in the presence of time reversal symmetry in the conventional Wigner-Dyson symplectic class (AII) in two-dimension without any topological term in the σ -model action a new unstable fixed point appears, $\sigma_{\text{sp}} \approx 1.4e^2/h$ [48]; thus it exhibits a metal-insulator transition. If the conductivity is below the critical value (σ_{sp}) then usual localization drives the system into the insulating phase, while if it is larger the system shows anti-localization. Similarly in graphene, in the presence of long-range disorder and TR invariance two valleys become decoupled; thus the σ -model action acquires a topological $\theta(=\pi)$ -term. Then the Q matrix is an 8×8 matrix with an additional constraint related to charge conjugation, $Q = \bar{Q}$. The θ -term provides a “topological protection” of the localization when the conductivity is small, which allows the system to flow towards the “super-metal” fixed points [41, 47, 49].

In this situation a more intuitive picture can be given. Due to the chiral nature of its charge carriers in graphene, the motion of electrons along a closed path in the presence of long range disorder introduces an extra phase. It changes the sign of the amplitude of one path with respect to its time reversed one. Because of the extra phase the interference becomes destructive; hence, the localization effect get suppressed (see Fig. 1.7)³. For instance, it has been shown numerically that the Dirac fermions, near the charge neutrality point, in the absence of inter-valley

³Numerical simulation shown in the Fig. 1.7 is performed with the Gaussian correlated long-range disorder, which acts as a random scalar potential in single flavor graphene.

$$\langle U(\mathbf{r})U(\mathbf{r}') \rangle = K_0 \frac{(\hbar v)^2}{2\pi\xi^2} e^{-|\mathbf{r}-\mathbf{r}'|^2/2\xi^2} \quad (1.13)$$

where ξ is the correlation length. Due to no mixing of the valleys, it falls into the AII symmetry class that allows for a topological θ -term in the action.

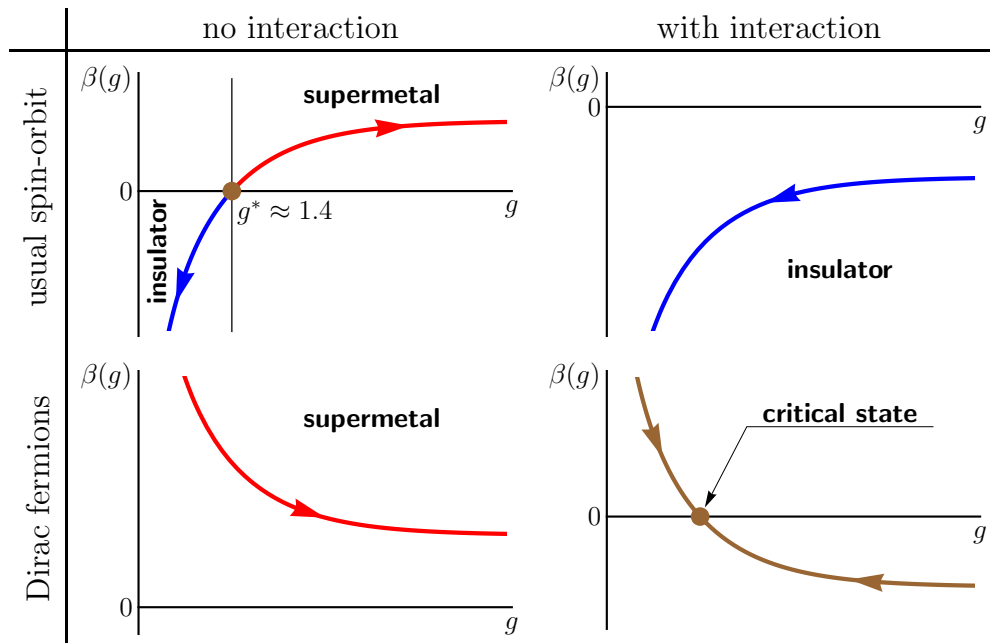


FIGURE 1.8: Schematic drawing of the β -function in two-dimensional disordered system in the class AII. Upper panel shows the usual spin-orbit systems which does not have any topological protection thus including interaction it shows complete localization (right hand side of the upper panel). The lower panel shows the appearance of the interaction induced critical point in Dirac fermions that have “topological protection” from the θ -term in the σ -model action. Adapted from Ref. [51].

scattering show weak anti-localization where the β -function, Eq. A.10, remains always positive [41, 47]. It suggests that with increasing system size the conductivity increases; consequently, the system flows to the “super-metal” fixed point, $\sigma \rightarrow \infty$.

The field is still in its nascent state. Many transport experiments are needed to verify all the claims. For instance, in a certain field theory that belongs to the symplectic class, AII, and represents graphene with long-range scalar disorder, the existence of another fixed point has been proposed [50]. Moreover, the very existence of the new point is supported by the topological term in the σ -model in class AII. However, presently the proposed critical point, σ_{sp}^* , has been ruled out by numerical simulations presented previously [47].

Similar situation arises in the surface of a three-dimensional topological insulator. The topological insulators are bulk insulators with the property that the surface modes are non-localizable metal states (gap-less) [52]. In the presence of a random scalar potential the surface states (two-dimension) behave like a single species of massless Dirac fermions in the class AII, which is similar to graphene Hamiltonian with decoupled valleys. Without any electron-electron interaction, the β -function

($\beta = N/2$, where N is the number of degenerate species, e.g. spins, flavors etc.) shows the super-metallic behavior as mentioned earlier. Now, with the electron-electron interaction there is a competing mechanism that allows for localization of electronic states in two-dimension and leads to a logarithmic correction to the conductivity [53]. The resulting β -function from the one-loop RG calculation for the symplectic class and not too strong interaction ($r_s \sim e^2/\hbar v_F \lesssim 1$) in the large conductance limit ($g \gg 1$) is given by [54],

$$\beta(g) = \frac{N}{2} - 1 + (N^2 - 1)\mathcal{F} \quad (1.14)$$

where, \mathcal{F} is the multiplet interaction parameter. The -1 is induced by the interaction in the large conductance ($g \gg 1$) limit. In usual graphene the number of species are $N = 4$ (spin and valley) thus the resulting β -function is positive suppressing the interaction effect. However, in the surface of a three-dimensional topological insulator in the presence of a long range disorder the $N = 1$; therefore, the β -function is negative giving rise to an instability in the system. The combined effect at large (interaction effect) and small (topological protection) g drives the system to an intermediate critical point (see Fig. 1.8), which is identified as the “*self-organized quantum criticality*” [51]. Further experimental and numerical investigations are required to verify such critical phenomenon in real materials.

1.2.2.2 Disorder preserving chiral symmetry

Gade-Wegner criticality: The chiral classes (AIII, BDI, and CII) are special in a sense that these classes support a critical fixed point in two-dimension. This classes of the σ -models allow an extra term (known as the Gade term) that accounts for the fluctuations of $\det Q$ [55]. These theories are characterized by a line of fixed point with non-universal conductivity. The remarkable feature shows up in the density of states, which is strongly diverging [56],

$$\rho(E) \sim \frac{1}{E} \exp(-c|\ln(E/\Delta)|^{1/x}) \quad (1.15)$$

where, x is the dynamical exponent and Δ is the mean level spacing. The situation is similar to an one-dimensional wire in the chiral class, where it exhibits the Dyson singularity of the form, $1/E |\ln E|^{1/3}$. However, in one-dimension the pile up of zero modes is sensitive to the boundary condition; hence the singularity can only be observed within the energy interval of the order of the mean level spacing, Δ . By contrast, in two-dimension the singularity shows up at much higher energy which is smaller than the band width but larger than the Thouless energy ⁴.

⁴The Thouless energy is defined as the inverse of the time that an electron needs to feel the boundary of a disordered sample after entering the system.

Vacancies in graphene: Vacancies are an important kind of disorder in graphene that preserves the chiral symmetry and dominates the physical properties with the material aspects of the sample. Vacancies (i.e, missing carbon atoms from the hexagonal lattice) are also a very natural form of disorder that often appear in sample preparation processes [12]. Moreover, a vacancy can also be realized approximately by adding an atom or a functional group to a carbon atom that breaks the sp^2 -hybridization of the π orbitals, with an on-site energy larger than the energy bandwidth. The vacancy that belongs to the chiral symmetry class (BDI) introduces an extra zero-energy electronic state (zero mode) that has anomalous topological properties. For instance, it has been shown using an index theorem that the number of zero modes is given exactly by the difference $N_A - N_B$, where $N_A(N_B)$ is the number of vacancies in sub-lattice A (B) [57]. More importantly, these linearly independent wave-functions (zero modes) are localized on one of the sub-lattices and remain unperturbed by modifications in other sub-lattice. The above statement holds as long as the perturbations in other sub-lattice preserve the chiral symmetry of the Dirac Fermions. The density of states (DoS) of the class BDI has the same diverging feature as seen in other chiral classes (Eq. 1.15),

$$\rho(E) \sim \frac{1}{E} \exp(-c|\ln(E/\Delta)|^{2/3}) \quad (1.16)$$

The value of c depends on the model microscopic. For instance, for two flavor Dirac fermions subjected to a chiral random mass (g_m) and random vector potential (g_A) the value of c has been calculated exactly, $c = 3g_m^{-1}$, in the RG framework in the diffusive limit where σ -model is valid and g_A is larger than unity (the strong coupling limit) [58]. For graphene in the presence of vacancies one expects the same remarkable feature in the density of states as it also belongs to the same symmetry class BDI. A detailed numerical investigation of the DoS is needed to understand this behavior.

Furthermore, transport experiments are very sensitive to these vacancies as finite concentration of vacancies form a very narrow impurity band exactly at zero energy (Fermi energy). In particular, how the width of the impurity band depends on the concentration of vacancies and system size is still an open question in the community. A part of this thesis will delve more into this matter where we will show that for the vacancies that are evenly distributed over the two sub-lattices, the observable quantity such as conductivity saturates at a constant value unlike the long range impurity potential in the class AII, where it reaches infinity in the limit of infinite system size.

1.2.3 Half-integer quantum Hall effect

The quantum Hall effect (QHE) in graphene is among the most interesting manifestation of the Dirac nature of the massless relativistic quasi particles. Indeed

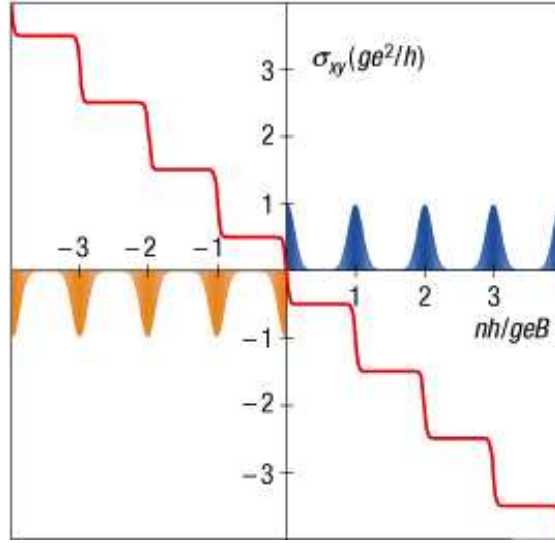


FIGURE 1.9: Schematic view of the LL structure in single layer graphene as a function of carrier concentration, n . Blue and orange for different charge carriers with electrons and holes character respectively. Plateaus of Hall conductivity, σ_{xy} is also shown in red in the unit of e^2/h . Adapted from Ref. [64].

the QHE was among the first transport experiment that helped to identify the material quality of graphene in the early days of its discovery. Interestingly, it has been observed at much higher temperature and lower magnetic fields than the usual two-dimensional electron gas⁵.

Theoretically the effect of a magnetic field, B , on graphene has been studied quite rigorously, specifically in the presence of disorder [60–63]. It has been shown, for instance, that the linear dispersion manifests itself in a special Landau level (LL) structure giving rise to a different kind of quantum Hall physics. In the presence of a perpendicular magnetic field a single LL evolves continuously from the upper and the lower Landau levels at zero energy that separates states with electron and hole characters (Fig. 1.9). Importantly the lowest LL has half of the degeneracy than the other levels. The Hall conductivity is given by,

$$\sigma_{xy} = 4 \left(n + \frac{1}{2} \right) \frac{e^2}{h} \quad (1.17)$$

⁵The energy levels in graphene in the presence of a magnetic field, B , scales with the Landau level (LL) index as $\sqrt{n|B|}$ unlike the two-dimensional electron gas where energy scales linearly with the LL index. Consequently, the energy spacing can be relatively large between two LL ($\Delta_n = E_{n+1} - E_n$) compared to the Zeeman splitting at low energies. Since, the observation of the quantization of σ_{xy} relies on the condition that at some given temperature the cyclotron gap should be large enough so that no excitations across the gap are possible (i.e, $\Delta_n \gg k_B T$); thus the QHE in graphene can be observed at much higher temperature than in a usual QHE two-dimensional metals. The fact has been confirmed, even at room temperature by several experiments [59].

where n is the integer that defines the LL index. The pre-factor “4” comes from the spin (2) and the valley (2) degeneracies of the graphene lattice structure. The additional $1/2$ in the Eq. (1.17) is the hallmark of the chiral nature of the Dirac fermions. Thus, it is known as the half integer quantum Hall transition unlike the usual integer quantum Hall transition in two dimensional electron gas. The half integer behavior has also been confirmed by several experimental studies in recent years [37, 59, 65]. The system falls into the usual Wigner-Dyson unitary symmetry class (A) as the TR invariance is broken by the external magnetic field. In this class the σ -model allows for a topological θ -term, which becomes energy dependent. However, at the zero energy ($\varepsilon = 0$) the vanishing Hall conductivity $\sigma_{xy} = 0$ allows the topological term to remain unchanged, $\theta = \pi$. Consequently, the half-integer Hall effect emerges with a plateau transition point exactly at the charge neutrality point (or Dirac point, $\varepsilon = 0$). From an alternative point of view, the appearance of $1/2$ in Eq. (1.17) can be understood by considering the Berry phase that the electrons, which are chiral, acquire while completing a closed orbit in a perpendicular magnetic field (cyclotron motion). This additional phase shift by ‘ π ’ in the QHE limit (high magnetic field) leads to a half-step shift in the LL structure of graphene [4].

1.2.3.1 Critical fluctuations of wavefunctions: Multifractality

“Multifractality” characterizes the strong fluctuations of wavefunctions at the Anderson transition; such as the quantum Hall criticality mentioned earlier. It is an important concept in a sense that it can be used to identify several other fixed points. From the σ -model perspective fluctuation of the wavefunctions reflect themselves in the Q matrices; thus the σ -model is capable of signaling a transition. The presence of multifractality also implies the presence of infinitely many operators. Multifractal structures are characterized by an infinite set of exponents describing the scaling of the moments of some distribution [56, 66].

Inverse participation ratio: The moments of the wavefunctions amplitude, $|\psi(\mathbf{r})|^2$, known as the *inverse participation ratio* (IPR) distinguish the metal, insulator, or the multifractal nature of the wavefunctions. The IPR is a function of normalized wavefunctions with argument q (real) and is defined as,

$$P_q = \int d^d \mathbf{r} |\psi(\mathbf{r})|^{2q} \quad (1.18)$$

At the critical point the P_q shows an anomalous scaling behavior with the system size, L ,

$$\langle P_q \rangle = L^d \langle |\psi(\mathbf{r})|^{2q} \rangle \sim L^{-\tau_q} \quad (1.19)$$

where, $\langle \rangle$ denotes the ensemble averaging over disorder realizations and τ_q is a set of continuous exponent. Often one defines another set of exponents by splitting

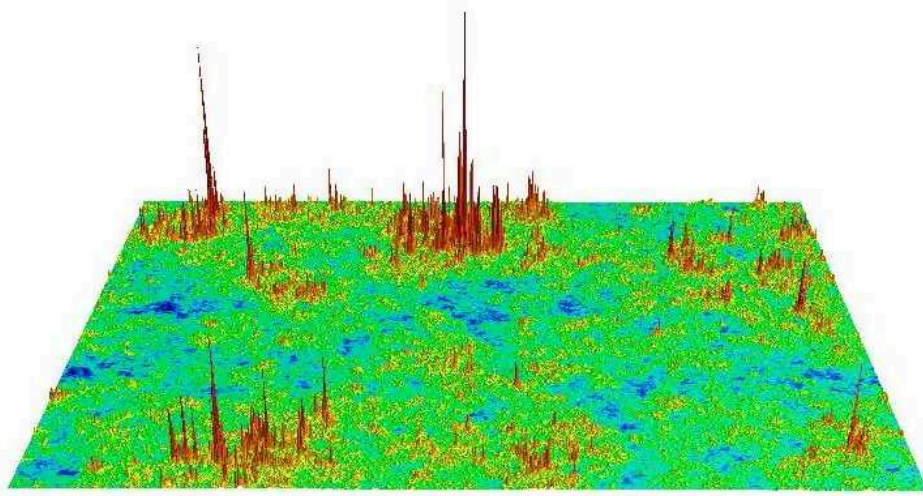


FIGURE 1.10: Wavefunction fluctuations illustrating the multifractal behavior at the quantum Hall transition. Numerical calculation was done on the Chalker-Coddington model network model (Mildenberger and Evers, unpublished).

off the normal part, which is known as the anomalous dimension, Δ_q ,

$$\tau_q = d(q - 1) + \Delta_q \quad (1.20)$$

where, $d = 2$ for a two-dimensional system. The anomalous dimension plays a key role in determining the scale dependence of the wavefunction correlations in general. For instance, Δ_2 describes the spatial correlation of the intensity, $|\psi(\mathbf{r})|^2$,

$$L^{2d} \langle |\psi_i^2(\mathbf{r}) \psi_j^2(\mathbf{r}')| \rangle \sim \left(\frac{\mathbf{r} - \mathbf{r}'}{L_\omega} \right)^{-\Delta_2} \quad (1.21)$$

where, $\omega = E_i - E_j$ and $L_\omega \sim (\rho\omega)^{-1/d}$ with ρ being the density of states (DOS). Product of the two point correlation function (Eq. (1.21)) can be expressed in terms of the Green's functions averages, which may be calculated with the σ -model. It turns out that the diffusion propagator that appears in the σ -model, scales exactly in the same way with the same scaling exponent [66]. We will come back to this issue later in this thesis.

The $f(\alpha)$ -spectrum: Further insights of multifractality can be gained by studying the distribution function, \mathcal{P} , of the wavefunction amplitudes. The probability distribution is formulated in the following way,

$$\mathcal{P}(|\psi|^2) \sim \frac{1}{|\psi|^2} L^{-1+f(\alpha)} \quad (1.22)$$

Now, it is a straight forward calculation to relate the distribution function, \mathcal{P} , with the exponents, τ_q ,

$$\langle P_q \rangle \sim \int d\alpha L^{-q\alpha+f(\alpha)} \quad (1.23)$$

where $\alpha = -\ln |\psi|^2 / \ln L$. The exponents are related by a simple Legendre transformation,

$$\tau_q = q\alpha - f(\alpha) \quad (1.24)$$

with $q = f'(\alpha)$ and $\alpha = \tau'_q$. Just to get a feeling for the $f(\alpha)$ one needs to consider the following: for a metal the fluctuations in the wavefunction amplitude is small or negligible; therefore the distribution of α (hence the $f(\alpha)$) will peak sharply around one particular point ($\alpha_0 = d$). For insulator the wavefunction is localized at a point in space thus distribution function is broad and not bounded in width. Clearly, for the critical wavefunctions the situation is in between and is characterized by some non-trivial $f(\alpha)$, which we discuss in the following section.

Weak multifractality and parabolic spectrum: In the limit of weak multifractality (PRBM model with $b \gg 1$, see Ref. [66]) the spectrum of τ_q can be evaluated analytically, where the critical point is close to the metallic fixed point. In this case the spectrum is given by,

$$\tau_q \simeq d(q-1) - \gamma q(q-1); \quad \gamma \ll 1 \quad (1.25)$$

The anomalous dimension is $\Delta_q = \gamma q(q-1)$. Here, it is important to note that the definition of Δ_q and the wavefunction normalization restrict the functional dependence of Δ_q on q i.e. $\Delta_{0,1} = 0$. The parabolic spectrum in Eq. (1.25) is an exact result in some situations, e.g. in a model of Dirac electrons with random vector potential in symmetry class AIII. The parabolicity also manifests itself in the $f(\alpha)$ spectrum, which is related by the Legendre transformation to τ_q as,

$$f(\alpha) \simeq d - \frac{(\alpha - \alpha_0)^2}{4(\alpha_0 - d)}; \quad \alpha_0 = d + \gamma \quad (1.26)$$

In some situation, for instance, in the model of random vector potential in class AIII the exact parabolicity is limited by q -values. It has been shown that τ_q has a discontinuity in the second derivative at $q_c \equiv f'(\alpha)|_{\alpha \rightarrow 0}$ and is strictly constant, $\tau_{q_c} = -f(0)$, above the critical point q_c . This behavior is known as ‘termination’ of the multifractality spectrum [66].

It has been proposed that the conformal field theory for the quantum Hall problem has the form [67],

$$S[g] = \frac{1}{8\pi t} \int d^2x \text{Str} \partial_\mu g^{-1} \partial_\mu g + iS_{WZ}[g] \quad (1.27)$$

where, $iS_{WZ}[g]$ is the Wess-Zumino term (Eq. (A.14)) and the corresponding model

is known as the Wess-Zumino-Witten model [68]. The model propose an exact parabolic spectrum, i.e. $\Delta_q = \gamma q(q - 1)$. While the parabolicity of Δ_q and $f(\alpha)$ for IQHE has recently been discouraged [69, 70] by numerical simulation using the Chalker-Coddington network model [71], it has also came to light recently that the network model suffers from large finite size correction [72]. Thus further careful analysis is required to reach any definite conclusion regarding the critical theory of the integer quantum Hall transition.

1.2.3.2 Interaction effects

While, many aspects of the low-temperature transport in the context of QHE have been understood in the framework of a single particle picture, understanding the effect of the electron-electron interaction on the integer quantum Hall transition still poses a considerable amount of challenge. Interaction manifests itself in low-temperature transport experiments mainly in two ways: a) renormalization and b) dephasing.

Renormalization: The problem of interaction by itself is a rich and difficult problem to analyze. Renormalization effects are mainly due to the virtual process induced by the electron-electron interaction. For instance in a one-dimensional system, which serves as a paradigmatic example of strong Anderson localization (Luttinger liquid), interaction induced renormalization effects are extremely important. It has been shown that strong attractive interaction can lead to delocalization of the electrons [53]. In two-dimensional systems the effects become even more interesting. In order to deal with the problem, Finkelstein et. al. [73] developed a RG approach based on the σ -model, which is particularly interesting because it made possible to analyze the critical behavior at the localization at $2 + \epsilon$ dimension in the situation when SR invariance is broken due to spin-orbit coupling, magnetic field, or in the presence of magnetic impurities. However, it has been shown that in the presence of SR invariance systems develop a magnetic instability that leads to an interaction induced “metal-insulator” transition for strong interaction [73], where interaction destabilizes the disorder induced localization. Some recent experiments on low-density two-dimensional structures (Si MOSFETs) seem to support the claim at low temperatures [74].

Dephasing: The effect of dephasing is governed by inelastic processes of electron scattering, at finite temperature, T . For a long time the effect of dephasing has been studied in the framework of weak localization, where dephasing provides a natural cutoff for the localization phenomenon [53]. Similarly, dephasing also contributes to the smearing of the phase transitions at finite T that occurs at the Anderson transition, which is a prototype of quantum phase transition at $T = 0$. For instance, experimental investigations show that the width of the

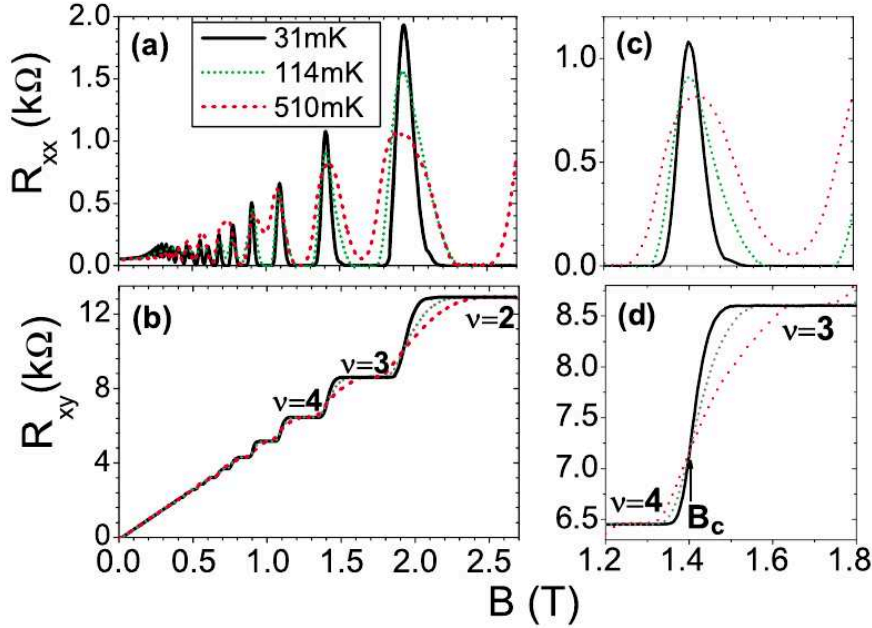


FIGURE 1.11: (a) Experimental evidence of the temperature dependence of the longitudinal resistivity illustrating the change in the width with increasing temperature. Experiment was performed on the $\text{Al}_x\text{Ga}_{1-x}\text{As} - \text{Al}_{0.33}\text{Ga}_{0.67}\text{As}$ heterostructure for different Al concentration, where it was claimed that the dominant contribution to disorder is from the short-range potential fluctuations. (b) Temperature dependence for the Hall plateaus. (c) (or (d)) Shows one peak (or plateau) of the same plot in the left. Adapted from Ref. [75].

critical region at the integer quantum Hall transition scales with the temperature as, $\Delta B \propto T^\kappa$ where, $\kappa = 0.42 \pm 0.04$ [75, 76]. However, the situation is not clear, as there are other studies that favors slightly larger value of the exponent, $\kappa = 0.56 \pm 0.02$ [77, 78]. It was proposed that the smaller value indicates the presence of short-range disorder when true integer quantum Hall critical point can be achieved; the larger value, however, points towards a possible “impurity clustering” in the sample [75].

In a usual two-dimensional electron gas the finite range interaction is irrelevant in a renormalization group sense; since, the interaction strength, λ , scales as $\lambda \propto L^{-\mu_2}$, where $\mu_2 > 0$ is the scaling dimension and L is the length of the sample. It signifies, for instance, that the effective interaction becomes weaker with the increasing size of the system, so that the non-interacting fixed point remains unaffected by the presence of finite range interaction. The interaction, however, can not be discarded fully. As it turns out that at finite temperature without the dephasing induced by the interaction, the conductivity would be zero.

In this thesis, we will use a numerical approach to address the issue of the effect of finite range electron-electron interaction, which is a very generic feature of any

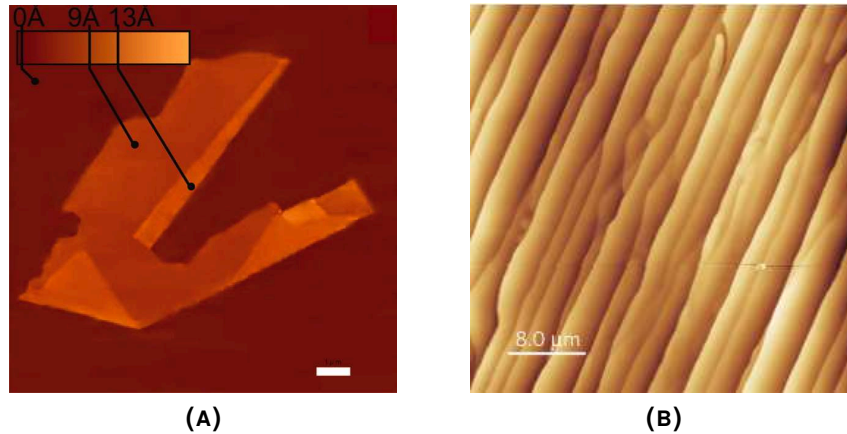


FIGURE 1.12: (A) Atomic force microscopy (AFM) image of few layers of graphene crystal on top of an oxidized Si wafer. The graphene was extracted using the micro-mechanical cleavage technique mentioned in the text. Figure is adapted from Ref. [5]. (B) AFM image of epitaxial graphene on 6H-SiC (0001) substrate. Adapted from Ref. [80].

quantum Hall critical point, on the integer quantum Hall transition as observed in a usual two-dimensional disordered metals.

1.3 Fabrication methods

For a long time, the existence of a perfect two-dimensional (2D) crystal was thought to be thermodynamically unstable and could not exist in nature. Because of strong atomic vibrations (long wavelength phonons) at finite temperature, any true long range ordering in low dimensional crystal lattice is nonexistent. The argument was first proposed by Landau and Peierls about 70 years ago and was later extended by Mermin and Wagner in the context of isotropic Heisenberg model [79].

As technology has steadily changed in last few years, so has the scientific research. In 2004 Geim and Novoselov were able to isolate graphene, a single layer of carbon atoms packed in a hexagonal lattice, using a cutting-edge technique called micro-mechanical cleavage [1, 5]. The weak van der Waals interaction between three-dimensional graphite layers (out-of-plane) played the major role in the method. It is much smaller than the covalent bond strength between the carbon atoms in the 2D plane of graphene. The method, i.e. peeling off a single layer of graphene from the graphite surface, is also known as the exfoliation technique, is not only economical but can also produce graphene crystal as large as $\sim 1\text{mm}^2$. Since its fabrication has become technologically feasible, the study of graphene has been the most active field of research in theoretical and experimental condensed matter community in the last decade.

From the point of view of electronic devices, another approach of manufacturing graphene has also emerged in last couple of years. Here, the graphene is grown on single crystal silicon carbide (0001 or $000\bar{1}$ surface of SiC) substrates [80–85] in an ultra high vacuum where crystals are heated upto about 1300 °C. The advantage is similar to those employed earlier for silicon-based electronic devices where high quality layers were grown on a large substrate (see Fig. 1.12). Moreover, this process directly allows to use the epitaxial graphene as a high quality electronic device or in a circuit with micro-electronics patterning. However, the epitaxial graphene is more prone to disorder, for example charge inhomogeneity, than the exfoliation technique because of a possibility of a charge transfer from the bulk SiC to the closet graphene layer.

Building a high carrier mobility clean graphene sample, which can be used as a possible electronic device, is still the most important topic in this field of research. The preparation of a clean sample so that it is free from any structural defects, using the previously mentioned experimental techniques seems difficult. For instance, in the micro-mechanical cleavage method often the sample is rippled or is folded along a certain direction (see Fig. 1.12a). In the epitaxial growth technique, it has been observed that the graphene layer that sits close to the SiC substrate is charged due to charge transfer from the bulk of the substrate; although, this particular growth technique allows to have relatively large clean samples when compared to other growth methods.

Another attractive approach is chemical vapor deposition (CVD) which is capable of producing relatively large graphene samples without very intensive chemical and mechanical treatments. In this process carbon is absorbed into a metal surface at high temperature and then precipitated out in the lowest energy state (graphene) at room temperature. The common features in all those experiments are a) the presence of uncontrolled edge structures, b) the fact that graphene and its substrate/scaffold have different thermal expansion coefficients; therefore, residual strain in the sample is a natural consequence of the preparation techniques. Hence, an increased interest in the elastic properties of graphene has developed recently.

1.4 Overview of the thesis

In this section we will give a small overview of the main results and organization part of this thesis.

In the first part we will address the issue of elasticity of small graphene flakes by means of density functional theory (DFT) calculations as implemented in the TURBOMOLE package. Here, our main focus is on the influence of graphene edges (zigzag) on bulk observables, i.e. elastic constants. In particular, we calculate the flake's free energy and disentangle the surface, bulk, and corner contributions. The

study shows that the surface contribution exerts a pressure which substantially diminishes the carbon-carbon distance in the flake's interior. We also compute all the elastic constants ("Lamé parameters") including bending rigidity in the DFT framework. By considering the contribution of zero point vibrations (phonons), we determine the quantum corrections in the elastic energy. Here, we will show that the phonon contribution is most significant in the bending rigidity, κ , which decreases by $\sim 26\%$ from its classical value ($\kappa = 1.2\text{eV}$).

In the second part of the thesis we investigate the effect of disorder (vacancies) on the transport properties of large graphene flakes. As mentioned previously, the presence of disorder plays an important role in determining the electronic and the transport properties of graphene. Indeed, when introducing vacancies that preserve the chiral symmetry something interesting happens, namely a single vacancy introduces a zero energy state at the boundary between the conduction and the valence band of graphene band structure. We find that with the increasing number of vacancies the ballistic conductivity increases, reaching a maximum value beyond which it starts to decrease until it eventually reaches zero in the percolation limit. Although common wisdom suggests that impurities tend to decrease conductivity in usual two dimensional electron gas, in graphene a finite concentration of vacancies form a very narrow ("impurity") band exactly at the zero energy that enhances the charge transport. Our calculation suggests that this increase in the conductivity not only depends on the vacancy concentrations but also on the distribution of vacancies over the two sub-lattices.

In the third part of the thesis we address the problem of the quantum Hall transition in the presence of electron-electron interaction. The quantum Hall effect in graphene was the very first transport experiment to determine the chiral nature of its charge carriers. Unlike a usual two dimensional electron gas, "disordered" graphene shows the half-integer quantum Hall transition in the presence of strong magnetic field. While many aspects of the Hall transition may be addressed in the framework of single particle physics, the role of electron-electron interaction at criticality stills lack full understanding. At the quantum Hall critical point, the wavefunction amplitude, $|\psi(\mathbf{r})|^2$, shows strong spatial fluctuations unlike the periodic nature (Bloch states) in a regular crystal lattice, which is characterized by the multifractality, Eq. 1.19. The multifractal structure of the wavefunction, which is a very generic feature of any quantum Hall transition, manifests itself in all correlation functions as well. We encounter, for instance, such correlation functions while calculating the interaction matrix elements in the perturbation theory at the criticality. It so happens that in the first order of the perturbation theory in interaction, the interaction matrix elements scale with the "sub-leading" multifractal exponent; because the Hartree and the Fock correlation, having the same leading scaling exponent, cancel each other. Our results have a profound impact on the understanding of the quantum Hall transition, as it supports that the short range interaction is irrelevant from the point of view of the renormalization group, since the dephasing due to interaction does not destroy the critical fixed

point.

2

CHAPTER 2

Elastic properties of graphene flakes

Although the electronic properties of graphene are outstanding in its own vigor but also the mechanical stability of the graphene lattice, with Young modulus close to 1Tpa and hardness higher than the diamond, makes it a state-of-the-art candidate for the applications in nano technology [86]. However, being a zero-gap semiconductor, graphene can not be used directly as an electronic device, such as field effect transistor (FET). Among many other possibilities, strain is one of the promising candidate for tuning the band structure at the Fermi energy of graphene [18, 19]. In fact, calculation shows opening of a band-gap at the Dirac points due to asymmetrical strain (shear strain) distribution in a graphene lattice [11, 17, 20, 21, 87]. Strain in graphene comes with many consequences, in particular, it induces a gauge field that can generate a pseudo magnetic field of magnitude as large as 10T [17, 88]. Although the strain induced magnetic field does not break the overall time reversal symmetry of the system, which is because the gauge field acquires different sign at the Dirac points, $\mathcal{A}_{\mathbf{K}} = -\mathcal{A}_{\mathbf{K}'}$, it leads to the Landau quantizations of energy levels and observation of the quantum Hall effect without an external magnetic field [17].

Strain can be produced in many different ways. Besides by externally applied mechanical strain, sometimes it is present due to experimental preparation technique as a residual strain. Different edge structures, edge functionalizations, ad-atoms, structural defects can lead to strain and have different consequences in the electronic properties. In order to further emphasize the importance of strain let us also mention that a finite size flakes, which play an important role in device application, can acquire strain because of the edges. Thus understanding the interplay between the strain and the edge structure in graphene is a leading research topic in the community; consequently, an increased interest in the elastic properties has developed recently [28–30, 89–95]. In order to address the issue of strain a detailed

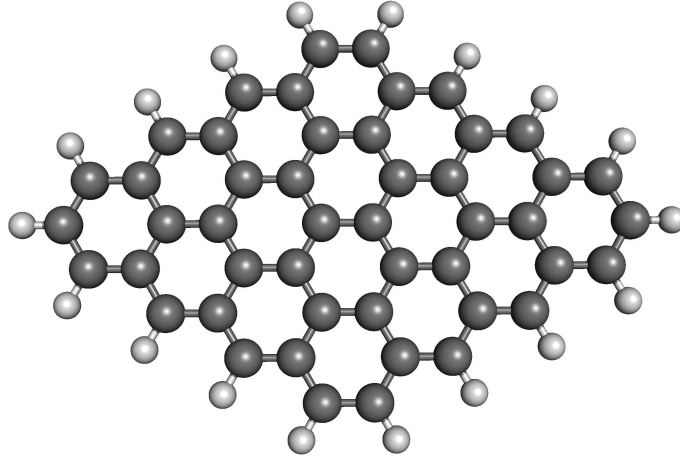


FIGURE 2.1: Geometry of the $N \times N$ hydrogenated graphene flakes (here $N=4$), that we have used for the density functional calculations.

study of the *elastic* properties of graphene is required. Also for elastic properties, edge effects can highly be relevant. For this reason, *flake* elastic properties are certainly interesting in their own right.

In this chapter our aim is threefold: first we will present a detailed study of the ground state energy of $N \times N$ hydrogenated zig-zag graphene flakes (depicted in Fig. 2.1) using the density functional theory (DFT) as implemented in a quantum chemistry package, TURBOMOLE. In finite size systems, the surface can give a sizable contribution to the free energy. We will show, that the different chemical nature of C-C bonds at the hydrogenated edge as compared to the bulk leads to an nearly homogeneous compression, i.e. strain. As a consequence, the average C-C-distance in a 3×3 flake is reduced by a substantial amount, 0.3%; for comparison, strain as achieved in typical experimental setup does not usually exceed values $\sim 1\%$ [93, 96, 97].

Second, we will investigate the elastic properties of such a flake in the presence of edges. It is particularly interesting because the presence of the surface induced strain leaves various traces in the flakes' interior observable. For instance, the flakes elastic constants, i.e. the Lamé parameters, are enhanced as compared to the value in the bulk. For isotropic strain in smallest flakes (3×3), the (inverse) compressibility $\mu + \lambda$ ¹ increases by 30%; for shear forces the increase is even bigger, almost a factor of 2.

And finally, we will address the issue of the phonon spectrum and will estimate the contribution of the atomic zero point motion to the elastic constants of the graphene flakes. Under bond compression the inter-atomic forces typically in-

¹ μ and λ are the Lamé coefficients that appears in the general definition of the free energy of a deformed isotropic body, $F = F_0 + \frac{1}{2}\lambda u_{ii}^2 + \mu u_{ik}^2$, where u_{ik} is the strain tensor. See Eq. (2.2).

crease, so that even the short wavelength vibrations, in particular the optical phonons, exhibit a “blue shift” of their frequencies with decreasing flake sizes. This flow can be seen in the variation of the Raman spectra with strain [97–102] and can be described in a standard manner by Grüneisen parameters. The values that we find here of Grüneisen parameters, agree reasonably well with previous reports [97, 100, 103].

The remainder of the chapter is organized as follows. In the first Section, we introduce the basic phenomenological theory of the ground state energy of the homogeneous planar flakes. Section two describes the basic methodology of our work, namely basics of DFT. And finally, we present the results along with the discussions and outlook of the work. The following work has been published in Ref. [104].

2.1 Phenomenological theory of elasticity in graphene

2.1.1 Ground state energy

In general, the total energy of a graphene flake such as the one depicted in Fig. 2.1 is a sum of local contributions of the bond energies. In principle, these may be thought of as contributions per bond or per atom. Here, we will focus on a representation in terms of bond energies valid for flakes with a homogeneous carbon-carbon-distance (C-C), d . The ground state energy of such a flake as a function of the bond length, d , is then given by,

$$F_N(d) = N_i\Psi(d) + N_e\psi(d) + N_c\psi^c(d) + \frac{\phi^e(d)}{N_e} + \frac{\phi^i(d)}{N_i} \quad (2.1)$$

where N_i denotes the number of internal C-C-bonds with an associated binding energy Ψ , N_e denotes the number of edge located C-C-bonds with energy ψ and ψ^c includes the corner contributions, where N_c is the number of bonds linking the ten corner atoms, $N_c=4$ in Fig. 2.1. The coefficients $\phi^{e,i}$ are further expansion parameters. The binding energy per C-C-CH edge group is close to 2ψ but not identical to it. For instance, ψ also includes corrections of internal bonds, that still “feel” the presence of the surface (edge). Similarly, $N_c\psi^c$ is approximating the binding energy of the corner groups (two HC-CH groups and two C-CH-C groups).

The representation (Eq. (2.1)) of the ground state energy is slightly simplified in the following sense. In general, the shape of the boundary of a given flake, e.g as shown in Fig. 2.1, does not share the hexagonal symmetry of the honeycomb lattice. For this reason, in flakes with a fully relaxed atomic structure bond lengths and

bond angles are not strictly all the same. Our DFT-calculations indicate, however, that such distortions, though clearly detectable, give only small corrections to those phenomenological parameters that we are mostly interested in.

The *continuum* theory of $2d$ -membranes has been devised for an inhomogeneous flake with neighboring bonds exhibiting slowly (in space) varying bond distances, $d(\mathbf{r})$, and angles. In this formulation the elastic energy is represented by the functional [105],

$$E = \frac{\kappa}{2} \int_{\mathcal{A}} d^2\mathbf{r} (\nabla^2 h)^2 + \frac{\mu + \lambda}{2} \int_{\mathcal{A}} d^2\mathbf{r} (u_{xx} + u_{yy})^2 + \frac{\mu}{2} \int_{\mathcal{A}} d^2\mathbf{r} [4u_{xy}^2 + (u_{xx} - u_{yy})^2]. \quad (2.2)$$

The flake coordinates are given with respect to a planar reference state with area \mathcal{A} , that lives in the $\mathbf{r}=(x, y)$ -plane; accordingly, the *in* plane coordinates constitute the displacement vector, $\mathbf{u}(x, y)$, that measures the translation of each membrane point (x, y, z) with respect to the reference state,

$$u_i = x'_i - x_i \quad (2.3)$$

where x_i is the coordinate of a point before the displacement and x'_i is the coordinate after the displacement. The *out of* plane distortions define the height field $h(x, y)$; for the planar case $h = 0$. \mathbf{u} and h together constitute the strain tensor ($i, j = x, y$),

$$u_{ij} = \frac{1}{2} \left[\frac{\partial u_i}{\partial x_j} + \frac{\partial u_j}{\partial x_i} + \frac{\partial h}{\partial x_i} \frac{\partial h}{\partial x_j} + \frac{\partial u_l}{\partial x_i} \frac{\partial u_l}{\partial x_j} + \dots \right], \quad (2.4)$$

The above expression describes the change in an element length when a body is deformed. We will only consider small deformations of the flake, therefore we will neglect all (nonlinear) higher order gradient terms. Note that the structure of the strain tensor (u_{ij}) defined in Eq. (2.4) is symmetric,

$$u_{ij} = u_{ji}. \quad (2.5)$$

The symmetric construction of the u_{ij} with respect to the spatial derivatives of \mathbf{u} ensures invariance under in plane rotations. Such infinitesimal rotations correspond to $\mathbf{u} \propto (y, -x)$ and hence the strain must be invariant under such displacements \mathbf{u} .

The total elastic energy Eq. (2.2) is a sum over contributions which resemble local oscillators in the membrane plane. The first term is proportionate to the curvature $\nabla^2 h$ and introduces the bending rigidity κ . It describes the energy cost for bending the membrane without changing the bond lengths or in plane bond angles. Here we left out certain effects related to the thickness of the graphene sheet in Eq. (2.2). For example, a linear displacement field ($h(\mathbf{r}) = x, \mathbf{u} = 0$) has no energy cost, because the description assumes, that such a conformation is equivalent to a rotation. However, this ignores that a rotation gives the π_z

orbitals a new direction in space, while the lifting up of atoms mediated by the linear displacement field does not. In the latter case, there is an additional energy cost $\propto |\nabla h|^2$ related to the fact, that the overlap of π_z -orbitals changes, which is not included in Eq. (2.2). Similarly, global rotational invariance is given only for free flakes. It can be broken due to experimental boundary conditions, e.g. the attachment of contacts. Also this may produce gradient terms $(\nabla h)^2$ in the functional Eq. (2.2).

The Lamé parameters, λ and μ , appearing in the second and third term of Eq. (2.2) describe the in plane rigidity. The elastic energy in Eq. (2.2) is constructed in such a way that the second term accounts for the isotropic deformation of the body, while the third term only survives in the presence of shear stress.

For homogeneous, planar membranes the elastic theory (Eq. (2.2)) may be considered as a continuum approximation to Eq. (2.1) which does not make explicit reference to boundary terms. It is important to note, that the feedback of the edge into the bulk is difficult to describe in a continuum theory. The reason is, that such theories (at least the conventional versions) by construction operate on the assumption that geometry and phenomenological parameters can be decoupled; thus the elastic constants are independent of shape and size of the sample. For this reason, a feedback of the edge into the elastic parameters is generically ignored. Edges, for instance, can be accounted only in the boundary conditions and (possibly) in a dependency of the Lamé parameters on the position with respect to the edge. Usually not included in (Eq. (2.2)) is the fact that this spatial dependency supports long range terms, $\sim 1/\text{flakesize}$. They modify the Lamé parameters appearing in Eq. (2.2) even inside the flake's interior.

2.1.2 Phenomenological parameters

In this section we will describe how the phenomenological parameters (Eq. (2.1)) relate with the elastic constants defined in Eq. (2.2).

2.1.2.1 Isotropic strain

In order to illustrate the cooperative effect between surface and bulk, we consider an expansion of the ground state energy in terms of the variable $\varepsilon = (d - d_0)/d_0$; ε quantifies the strain inside the flake. The bulk energy per bond has an expansion,

$$\Psi = \Psi_0 + \frac{1}{2}\Psi_2 \varepsilon^2 + \frac{1}{6}\Psi_3 \varepsilon^3 + \frac{1}{24}\Psi_4 \varepsilon^4 \dots \quad (2.6)$$

where the bulk bond length d_0 is to be determined at $N_{i,e} \rightarrow \infty$ with $\Psi_{0,1,2,\dots}$ are the expansion coefficients. The surface energy may also be expanded about a minimum bond length, d_0^e , but in general $d_0^e \neq d_0$. After all, in the limit $N_{i,e} \rightarrow \infty$, just the

first term in Eq. (2.1) contributes to the energy per area ($\mathcal{A}_{\text{flake}}^L = (3\sqrt{3}/2) d_0^2 N_L^2$: membrane area in the reference plane, $\mathbf{r} = (x, y)$; d_0 : minimum bond length) and therefore d_0 needs to minimize Ψ , only. Hence, we introduce the relative deviation of surface and bulk optimal bond lengths, $\mathfrak{d} = (d_0 - d_0^e)/d_0$, so that we have an expansion

$$\begin{aligned} \psi &= \bar{\psi}_0 + \frac{1}{2}\bar{\psi}_2 (\varepsilon + \mathfrak{d})^2 + \frac{1}{6}\bar{\psi}_3 (\varepsilon + \mathfrak{d})^3 + \frac{1}{24}\bar{\psi}_4 (\varepsilon + \mathfrak{d})^4 \dots \\ &\equiv \psi_0 + \psi_1 \varepsilon + \frac{1}{2}\psi_2 \varepsilon^2 + \frac{1}{6}\psi_3 \varepsilon^3 + \dots \end{aligned} \quad (2.7)$$

where the coefficients in the second line are defined in terms of the expansion coefficients of the above line, where we absorb the relative deviation of bulk and surface bond length, \mathfrak{d} , in the new definition of ψ . The elastic properties of the flake, i.e. the elastic constants (μ, λ), are now solely determined by the expansion parameters $\Psi_{2,3,4}, \psi_{1,2,3}$.

For any finite size flake $N_{i,e}$, optimization must also include the boundary (i.e. surface) terms and therefore the optimal value of ε , ε_N , is non-vanishing in this case; specifically,

$$\begin{aligned} \varepsilon_N &= -\frac{\psi_1 N_e}{\Psi_2 N_i} \\ &\approx -\mathfrak{d} \frac{\bar{\psi}_2 N_e}{\Psi_2 N_i} \end{aligned} \quad (2.8)$$

In order to calculate the feedback of this shift into the elastic parameters, we expand $F_N(d)$ in the vicinity of its minimum, ε_N , to the fourth order in $\varepsilon - \varepsilon_N$. At this point we recall that the isotropic strain corresponds to $\mathbf{u}(\mathbf{x}) = \varepsilon \mathbf{x}$. Now comparing the result with Eq. (2.2) after expanding Eq. (2.8) close to its minimum to leading order in N_e/N_i one gets,

$$\mu + \lambda = \frac{1}{4} \left(\Psi_2 + \frac{N_e}{N_i} \psi_2 \right) + \frac{1}{4} \Psi_3 \varepsilon_N + \frac{\varepsilon}{12} \left(\Psi_3 + \frac{N_e}{N_i} \psi_3 + \Psi_4 \varepsilon_N \right). \quad (2.9)$$

The above expression relates the elastic constants with the phenomenological expression defined in Eq. (2.1) in a finite size flake in the presence of isotropic strain. The first term in the rhs-expression of $\mu + \lambda$, Eq. (2.9), simply accounts for the separate, additive contributions of bulk and surface (i.e. edge) free energies. The edge contribution, that appears here, could formally be accounted for in a generalized version of Eq. (2.2) where one adds a boundary term. Note, that as the system size goes to infinite $N_i \rightarrow \infty$ the boundary vanishes; thus only the bulk terms contribute in Eq. (2.9). Similarly, by allowing for a dependency of the Lamé parameters on strain itself, one could also include additive an-harmonic effects, second bracket first two terms. In either case, the phenomenological parameters are universal in the sense, that they are the same for each flake size and geometry.

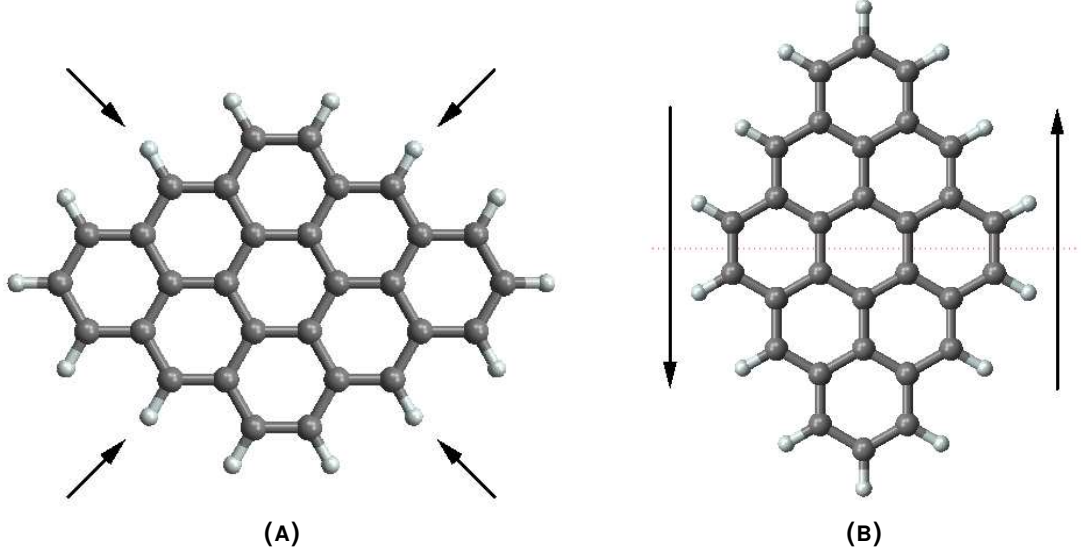


FIGURE 2.2: (A) Schematic view of the applied isotropic strain (ε) in a graphene flake. (B) Schematic view of the shear strain (ε_s) as applied in our DFT calculation. The dotted line represents the symmetry axis in the middle.

The interesting pieces are the terms in ε_N , which are mixing surface and bulk parameters: $\Psi_3 \varepsilon_N \sim \psi_1 \Psi_3 / \Psi_2$. They encode the “cooperative” effect between boundary induced strain and bulk anharmonicities. It is due to them, that the flakes elastic parameters need to be adjusted in principle for every geometry separately.

2.1.2.2 Shear Strain

An analogous analysis as for the isotropic strain also applies to shear forces. The expansion is even in the shear strain $\mathbf{u} = (0, \varepsilon_s x)$. The bulk energy per bond has an expansion,

$$\Psi = \Psi_0 + \frac{1}{2} \tilde{\Psi}_2 \varepsilon_s^2 + \frac{1}{24} \tilde{\Psi}_4 \varepsilon_s^4 + \dots \quad (2.10)$$

Due to the mirror symmetry of the graphene flake (see Fig. 2.2) along perpendicular axis of the applied strain, only even terms in ε_s appears in the bulk energy expansion. Similarly the surface energy is given by,

$$\psi = \psi_0 + \frac{1}{2} \tilde{\psi}_2 \varepsilon_s^2 + \frac{1}{24} \tilde{\psi}_4 \varepsilon_s^4 + \dots \quad (2.11)$$

The new expansion parameters, $\tilde{\Psi}_i, \tilde{\psi}_i, i = 2, 4, \dots$, are, in general, dependent on the flake geometry. Again, by comparing to Eq. (2.2) we find another elastic

constant in terms of the phenomenological parameters as,

$$\mu = \tilde{\Psi}_2 + \tilde{\psi}_2 + \frac{1}{12}\varepsilon_s^2 \left(\tilde{\Psi}_4 + \tilde{\psi}_4 \right). \quad (2.12)$$

Here, surface and bulk energies give strictly additive contributions in zeroth as well as in higher order in ε_s , and a cooperative effect does not emerge.

In the next section we present the calculation details for the elastic constants and the corresponding method used here.

2.2 Model and Method

We describe our calculation method for the ground state properties of the finite size flakes. Density functional theory (DFT) is an effective method to calculate the ground state energy, work function and several other properties of interacting many-body system. In the appendix (B) we give a small introduction in to the basic formalism of DFT. Here, we only present the basic calculational steps for elastic constants relevant to our study.

In Fig. 2.1 we display the geometry of the $N \times N$ -graphene flake that is employed in our calculations. For such a flake with N benzene rings at each side, the number of internal bonds $N_i = (N-1)(3N-1)$, and edge bonds $N_e = 8(N-1)$. Electronic structure calculations have been performed for a given atomic configuration (C-C distance, flake geometry etc.) on the basis of the density functional theory as implemented in the quantum chemistry package TURBOMOLE [106]. We are comparing GGA functionals (BP86 [107, 108], PBE [109, 110]) with a hybrid functional (B3LYP [111]) and use a minimal basis set (SVP [112]). Specifically, we are working at zero temperature and approximate the ground state energy, Eq. (2.1), by the DFT estimate for the total binding energy of the flake:

$$F_{\text{el}}(N, d) := E_{\text{el}}(N, d) - E_{\text{free}}(N). \quad (2.13)$$

with,

$$E_{\text{free}}(N) = N_{\text{H}}E_{\text{H}} + N_{\text{C}}E_{\text{C}} \quad (2.14)$$

where $E_{\text{H/C}}$ denote the DFT energies of a free charge neutral hydrogen/carbon atom and $N_{\text{H/C}}$ denotes the number of hydrogen/carbon atoms in the flake.

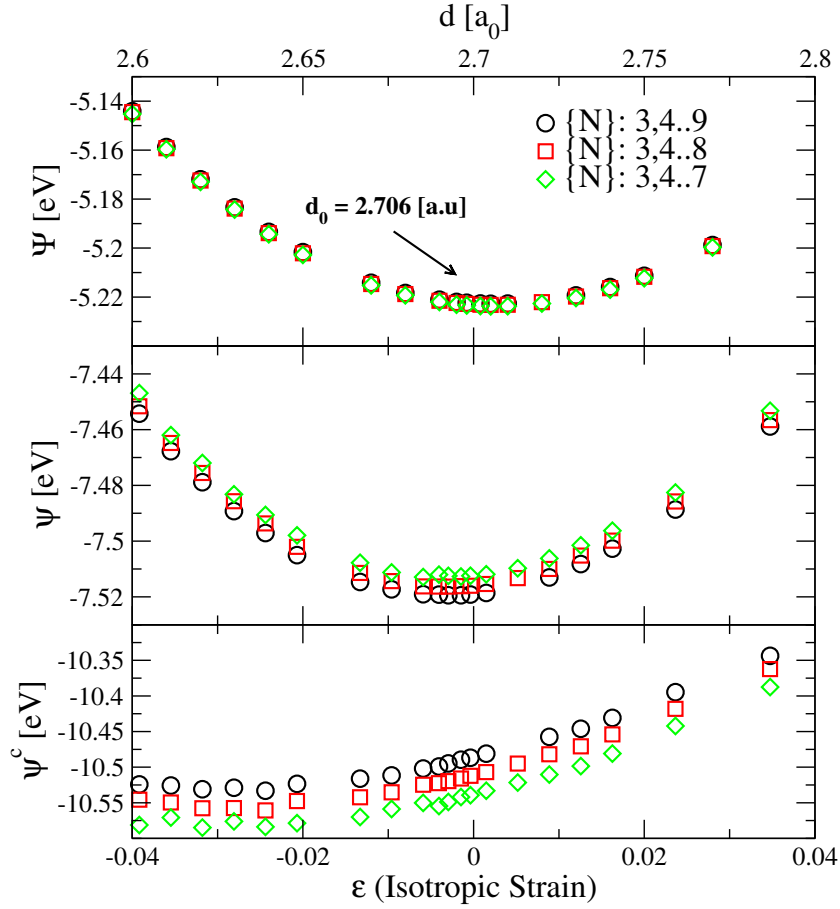


FIGURE 2.3: Bulk (Ψ), surface (edge, ψ) and corner (ψ^c) energy per carbon bond in the graphene flakes, Fig. 2.1, calculated with density functional theory (BP86-functional). Data based on the evaluation of three sets of flake sizes ranging from $\{N\}=3\dots 9$, and a 5 parameter fit to Eqs. (2.1,2.13) per d values. ($a_0:= 0.529$ Å.)

2.3 Result: Phenomenological parameters of bulk graphene

2.3.1 Isotropic strain

Bond energy representation: In this paragraph we present the result of our DFT calculation for phenomenological parameters in terms of bond energy. An alternative approach can be taken by considering the energy per atom, which we present in the next section.

A sequence of DFT calculations has been performed for $N=3\dots 9$ and different values of the C-C distance, d . For each distance, $F_{el}(N, d)$ has been calculated. In

DFT functional	d_0 [Å]	d_0^e [Å]
BP86	$1.432^{\pm 0.002}$	$1.427^{\pm 0.001}$
B3LYP	$1.426^{\pm 0.001}$	$1.421^{\pm 0.002}$
PBE	$1.431^{\pm 0.001}$	$1.426^{\pm 0.005}$

TABLE 2.1: Minimum C-C bond length as extracted from bulk energy and surface energy correspondingly (see Fig. 2.3, upper and middle panel). The distance in d_0 and d_0^e leads to a nearly homogeneous pressure on the flake that modifies elastic and electronic-structure properties. Data is shown for three different functionals used in our DFT calculations.

DFT functional	$-\Psi_0$ [eV]	$\frac{1}{2}\Psi_2$ [eV]	$-\frac{1}{6}\Psi_3$ [eV]
BP86	$5.223^{\pm 0.001}$	$46.301^{\pm 0.082}$	$128^{\pm 2}$
B3LYP	$5.008^{\pm 0.001}$	$47.7^{\pm 0.4}$	$154^{\pm 32}$
PBE	$5.373^{\pm 0.004}$	$45.57^{\pm 0.43}$	$187^{\pm 25}$

TABLE 2.2: Bulk energy coefficients as defined in Eq. (2.6). These coefficients are extracted from fitting Eq. (2.6) to the data in Fig. 2.3, upper panel.

order to extract the expansion coefficients of Eq. (2.1), $\Psi(d)$, $\psi(d)$, $\psi^c(d)$, $\phi^e(d)$, $\phi^i(d)$, we have performed five parameter fits on sets of raw DFT data. These fits were applied to three data sets consisting of $\{N\}=3, \dots, 7$, $\{N\}=3 \dots 8$ and $\{N\}=3 \dots 9$. The results for the surface, bulk and corner energy have been displayed in Fig. 2.3. The scatter between the fitting parameters belonging to different data sets is relatively small, which illustrates the stability of the fit.

The lattice constant of bulk graphene is estimated from the minimum position of $\Psi(d)$ Fig. 2.3, upper panel as $d_0=2.706a_0$, where $a_0=0.529\text{Å}$ denotes the Bohr radius. Comparing this position to the minimum of the edge (surface) energy, Fig. 2.3, center panel, $d_0^e=2.694a_0$, we find $\delta=0.44\%$. This indicates clearly the compression of the C-C bond length near the edge. The shift of the minimum position to lower values becomes even more pronounced near the corners, i.e. in $\psi^c(d)$, see Fig. 2.3, lower panel.

DFT functional	$-\psi_0$ [eV]	ψ_1 [eV]	$\frac{1}{2}\psi_2$ [eV]	$-\frac{1}{6}\psi_3$ [eV]
BP86	$7.515^{\pm 0.006}$	$0.285^{\pm 0.015}$	$44.93^{\pm 0.43}$	$113^{\pm 19}$
B3LYP	$7.187^{\pm 0.006}$	$0.261^{\pm 0.015}$	$45.6^{\pm 2.2}$	—
PBE	$7.63^{\pm 0.01}$	$0.308^{\pm 0.011}$	$47.5^{\pm 1.1}$	—

TABLE 2.3: Edge (surface) coefficients as defined in Eq. (2.7). These coefficients are extracted from fitting Eq. (2.7) to the data in Fig. 2.3, middle panel.

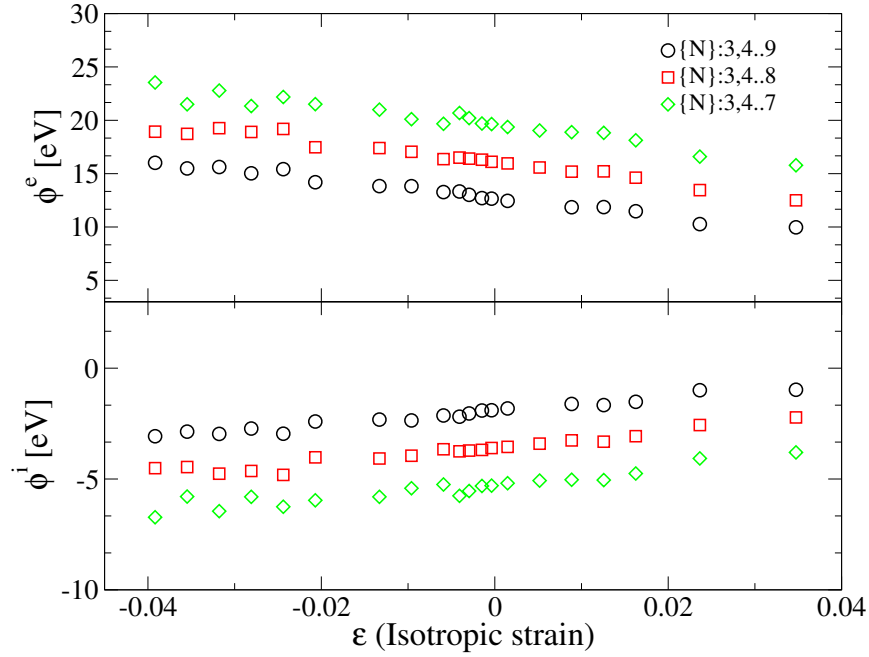


FIGURE 2.4: Dependency of the amplitudes $\phi^{i,e}$ describing the corrections in $1/N_{e,i}$ to the binding energy $\Delta F_{el}(N)$. Data were obtained by the 5 parameters fit, already underlying the traces shown in Fig. 2.3.

To obtain also the other phenomenological parameters, a second (polynomial) fit of the traces $\Psi(d), \psi(d)$, Fig. 2.3, according to Eqs. (2.6,2.7) has been performed; all fitting parameters are summarized in Tab. 2.1,2.2 and 2.3.

When fitting the raw data to get Ψ, ψ, ψ^c the terms in $1/N_{i,e}$ could not be neglected for the system sizes, that we considered. The corresponding amplitudes are displayed in Fig. 2.4. Unlike it was the case with the previous data, Fig. 2.3, the amplitudes $\phi^{i,e}$ of the $1/N_{i,e}$ -corrections still exhibit a considerable variation with increasing system size, which is due to even order terms that have been neglected in the expansion Eq. (2.1). Interestingly, while the magnitude of $\phi^{i,e}(\varepsilon)$ is still shifting the slope and perhaps also the sign of the two functions have converged, already. Under this assumption we may conclude, that both amplitudes flow closer to zero values when ε increases. This behavior is compatible with the simple expectation, that the main effect incorporated in the $1/N_{i,e}$ -corrections is the discreteness of the flake's electronic spectrum with level spacings $\Delta_{i,e}$ for bulk and surface modes. With increasing ε the bandwidth decreases and so do $\Delta_{i,e}$ and $\phi^{i,e}$.

Atomic energy representation: In the next paragraph we have repeated the analysis for a representation of the free energy as a sum of atomic contributions, Eq. (2.15). The representation of free energy in terms of a sum of atomic con-

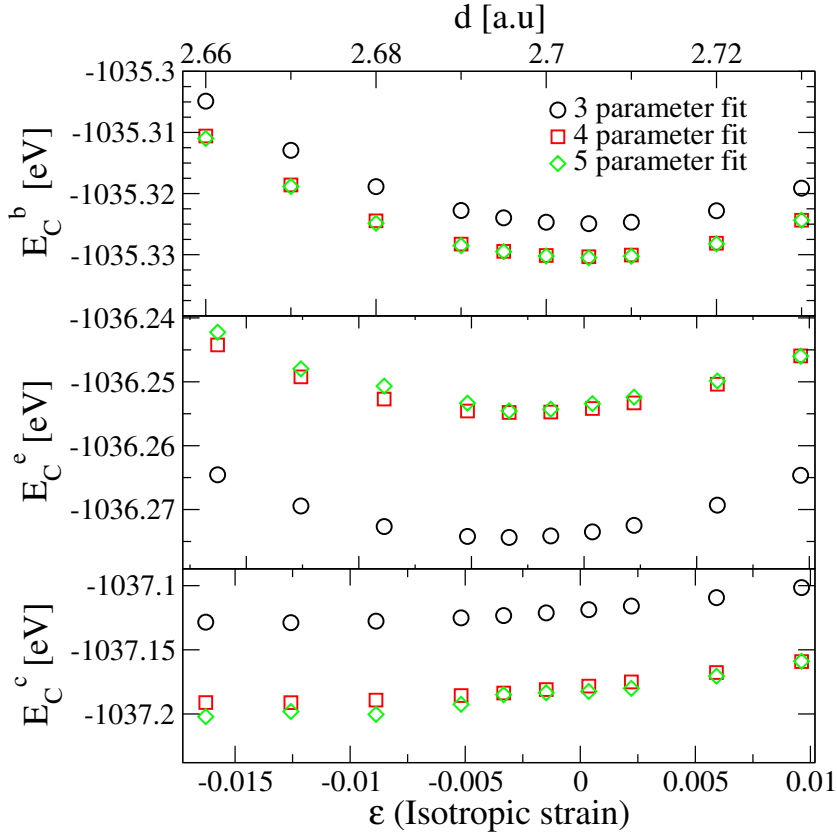


FIGURE 2.5: Bulk (E_C^b), surface (edge, E_C^e) and corner (E_C^c) energy as extracted from Eq. (2.16) using density functional theory (PBE-functional). Data based on the evaluation of flake sizes ranging from $\{N\}=4\dots 8$ per d values ($a_0:=0.529$ Å.). (\circ) denotes data from a 3 parameter fit to first three terms of Eq. (2.16) ignoring the correction terms. (\square) and (\diamond) are the data with four and five parameter fit of Eq. (2.16) including the correction terms. The scattering between the data sets that include the finite size correction terms is relatively small, which shows the stability of the fitting procedure.

tribution is particularly important to account for the finite size effects in small graphene flakes. The results are equivalent, of course, but the detailed comparison of the results based on our phenomenological theory with earlier findings for bulk systems, which we have relegated in the previous section, is simplified in this way. In a nutshell, our extrapolation scheme recovers the known values for the surface free energy (per Å) and the edge stress with excellent accuracy, see Tab. 2.4 and below Eq. (2.18).

In order to compare our basic results with previous authors here we perform a consistency check by evaluating the bond energies. We have a binding energy $\Psi(d_0)=-5.22\text{eV}$ for bulk carbon bonds. It translates into an energy per bulk C-atom (cohesive energy) $3\Psi(d_0)/2\approx-8.06\text{eV}$ which compares favorably well with an

Energy	PBE functional	prev. calc.
E_c^b [eV]	-1035.33±0.01	
E_c^e [eV]	-1036.25±0.02	
E_c^c [eV]	-1037.18±0.06	
E_{edge} [eV/Å]	0.114±0.001	0.106 [114, 115]

TABLE 2.4: Survey over the fitted total energy parameters and edge energy as defined in Eqs. (2.16, 2.15). Data extracted at zero strain, where the bulk C-C bond distance is minimum, $d_0 = 1.431\text{Å}$ (see Tab. 2.1).

earlier estimate [113] -7.9eV. For the edge energy we use the earlier definition [114, 115],

$$E_{\text{edge}} = \frac{1}{L} \left(E_{\text{tot}} - N_C E_C^b - \frac{N_H}{2} E_{H_2} \right) \quad (2.15)$$

where N_C is the total number of carbon atoms and E_C^b denotes the energy of a carbon atom in bulk graphene. $E_{H_2} = -31.496$ eV is the energy of a hydrogen molecule and N_H is the total number of hydrogen atoms that terminate the graphene edge of total length L . In order to estimate E_C^b we parameterize the total energy in full analogy with Eq. (2.1),

$$E_{\text{tot}} = N_C^b E_C^b + N_C^e E_C^e + N_C^c E_C^c + N_H E_H + \frac{\phi^e}{N_C^e} + \frac{\phi^b}{N_C^b} \quad (2.16)$$

with,

$$N_C = N_C^b + N_C^e + N_C^c. \quad (2.17)$$

where, N_C^b denotes the number of bulk carbon atoms (having only C-atoms as nearest and next nearest neighbours) with an associated energy E_C^b , N_C^e denotes the number of edge carbon atoms with energy E_C^e and N_C^c is the number of corner carbon atoms with energy E_C^c (CH-groups with at least one more CH-group as nearest neighbor; $N_C^c = 10$ in our case). $\phi^{b,e}$ are further expansion coefficients. $N_H = (N_C^e - 4)/2 + N_C^c$ is the total number of hydrogen atoms with energy per atom $E_H = -13.568$ eV in vacuum which is calculated separately. In order to estimate the bulk carbon energy we have performed a three, four, and five parameter fit on the raw DFT data. The fit is stable against the number of fitting parameters with data set consisting of $N = 4 \dots 8$, as shown in Fig. 2.5. Our estimate of the bulk energy E_C^b , edge energy E_C^e and corner energy E_C^c per carbon atom are listed in Tab. 2.4.

Finally, using these estimates we calculate the edge energy per unit length and its variation with homogenous, isotropic strain, ε , (Fig. 2.6). The result at zero strain, 0.114 ± 0.001 eV/Å, compares well with earlier works 0.106 eV/Å [114, 115]. Fur-

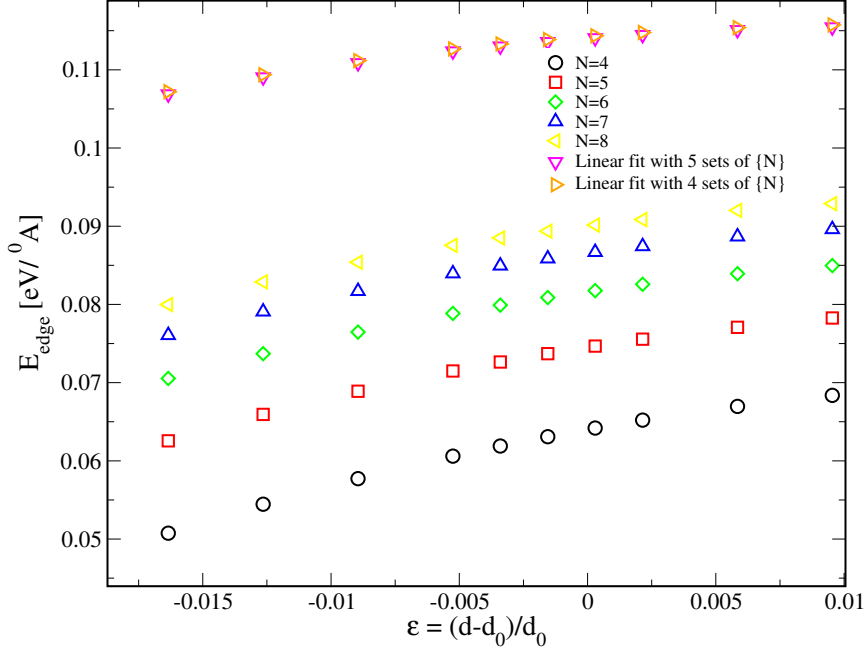


FIGURE 2.6: Change in the edge energy (E_{edge}) as defined in Eq. (2.15) when applying homogenous, isotropic strain (ε) in graphene flakes. Data sets are calculated using PBE functional for system sizes $\{N\}=4\dots 8$. $d_0=1.431\text{\AA}$, see e.g, Tab. 2.1. (∇) and (\triangleright) show the extrapolated value of E_{edge} at $N_C^c/L \rightarrow 0$ limit per d value using five ($\{N\}=4\dots 8$) and four system sizes ($\{N\}=5\dots 8$), respectively. Almost no scattering between these two data sets illustrates the convergence of the fit.

thermore, we extract the edge stress, τ_e , following the conventional definition [114],

$$\tau_e = \frac{dE_{\text{edge}}}{d\varepsilon}. \quad (2.18)$$

Our value, $\tau_e=0.26 \text{ eV}/\text{\AA}$, is significantly enhanced compared to the values reported for uniaxial strain, $\tau_e^{\text{ua}} = -0.01 \text{ eV}/\text{\AA}$ [114, 115], that have been obtained in a ribbon geometry. The lower sensitivity on homogenous uniaxial strain is not a surprise, since in that case a considerable part of the elastic energy cost for longitudinal stretching can be released by the transverse contraction. With homogenous isotropic strain the surface unit cell experiences stretching in all directions and there is no partially compensating relaxation process. In order to understand the relative smallness of the edge energy, E_{edge} , of the hydrogen terminated graphene flakes we rewrite Eq. (2.15) after substituting E_{tot} from Eq. (2.16),

$$E_{\text{edge}} = \frac{N_C^e}{L}(E_C^e - E_C^b) + \frac{N_C^c}{L}(E_C^c - E_C^b) + \frac{1}{2} \frac{N_H}{L} E_{\text{H}_2}^b + \frac{\phi^e}{LN_C^e} + \frac{\phi^b}{LN_C^b} \quad (2.19)$$

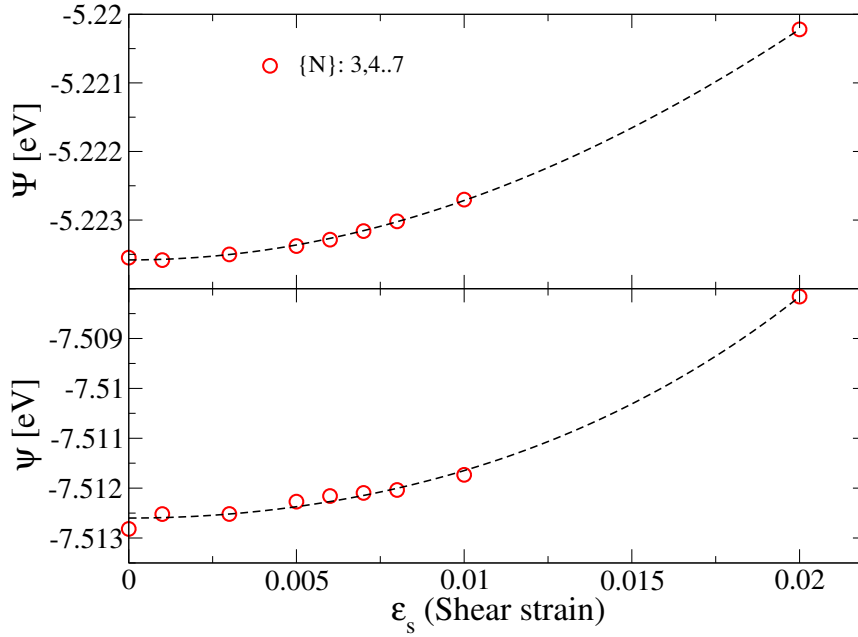


FIGURE 2.7: Change in the energy when applying a shear strain in graphene flakes. Upper panel shows the change in bulk energy per interior C-C bond; lower panel exhibits change in surface (edge) energy per C-C bond. Data sets are for system sizes $\{N\}=3\dots7$ and extracted from an expression analogous for shear to Eqs. (2.1,2.13). The lines indicate the polynomial fit according to Eqs. (2.10,2.11) with parameter given in Tab. 2.5.

with,

$$L = \sqrt{3}d \frac{N_C^e + 4}{2} + \frac{8d}{\sqrt{3}} \quad (2.20)$$

where N_C^e denotes the total number of edge C-atoms of a graphene flake and $E_{H_2}^b = 2E_H - E_{H_2} \approx 4.36\text{eV}$ is the binding energy of a hydrogen atom. Now, considering the limit $L \rightarrow \infty$, Eq. (2.19) reduces to

$$\lim_{L \rightarrow \infty} E_{\text{edge}} = \frac{E_C^e - E_C^b + E_{H_2}^b/4}{\sqrt{3}d/2}. \quad (2.21)$$

Using the above mentioned estimate, $E_C^e - E_C^b \approx -0.92$, we see that difference in bulk and edge binding energy is largely compensated by the additional binding energy averaged over two edge C-atoms contributed by the H_2 molecule, $E_{H_2}^b/4 \approx 1.09$.

Functional	$\frac{1}{2}\tilde{\Psi}_2[\text{eV}]$	$-\frac{1}{24}\tilde{\Psi}_4[\text{eV}]$	$\frac{1}{2}\tilde{\psi}_2[\text{eV}]$	$\frac{1}{24}\tilde{\psi}_4[\text{eV}]$
BP86	$8.4^{\pm 0.4}$	$871^{\pm 50\%}$	$9^{\pm 3.3}$	$5237^{\pm 60\%}$

TABLE 2.5: Bulk and surface shear energy coefficients as extracted from fitting Eq. (2.10) (Eq. (2.11)) to the data in Fig. 2.7 upper panel (lower panel).

2.3.2 Shear strain

A largely analogous method as was adopted for the isotropic strain, has also been applied for the calculation of phenomenological parameters in the presence of shear forces. In this case, the convergence of the DFT calculations turned out to be considerably more difficult, so that the investigated system sizes range from $\{N\}=3 \dots 7$, only; also investigation of different functionals turned out to be much more difficult than in other situation. From our fitting procedure we could determine the response of the bulk and surface energy to the shear strain, ε_s , as shown in Fig. 2.7. The parameters entering Eqs. (2.10,2.11) can be extracted and are listed in Tab. 2.5.

2.3.3 Summary and Outlook

Let us summarize at this point what has been achieved so far with the above study. Additionally, we will also provide an outlook for further study. Firstly, the different contributions to the ground state energy made by the flake's interior, its edges and corners are carefully disentangled within the DFT framework using different functionals. As a consequence, an understanding of the impact of the surface on the internal structure of the flake has been achieved. These insights are valuable for further investigations, such as charging energies and work-functions of small flakes.

At this point it is important to note that we only consider the leading order correction in $\mu + \lambda$ in the parameter N_i/N_e (see Eq. 2.9). In principle the analysis of higher order terms ($\sim (N_i/N_e)^2$) in the Lamé coefficients could be done, where one needs to be more careful about the contribution originating from the corners of the flake. A further study is required in this direction to understand the non-linear effects on the elastic properties of graphene.

Apart from higher order corrections, the correction terms in $1/N_e$ and $1/N_i$ has not been investigated in its full glory. Particularly, this corrections terms have significant implications for finite sized samples. Within the available numerical resources we were able to confirm the sign of the amplitudes (ϕ_i, ϕ_e). Additionally, our study also confirms the flow of the amplitudes close to zero with the system size and increasing applied strain. It reflects the essential physics of these two

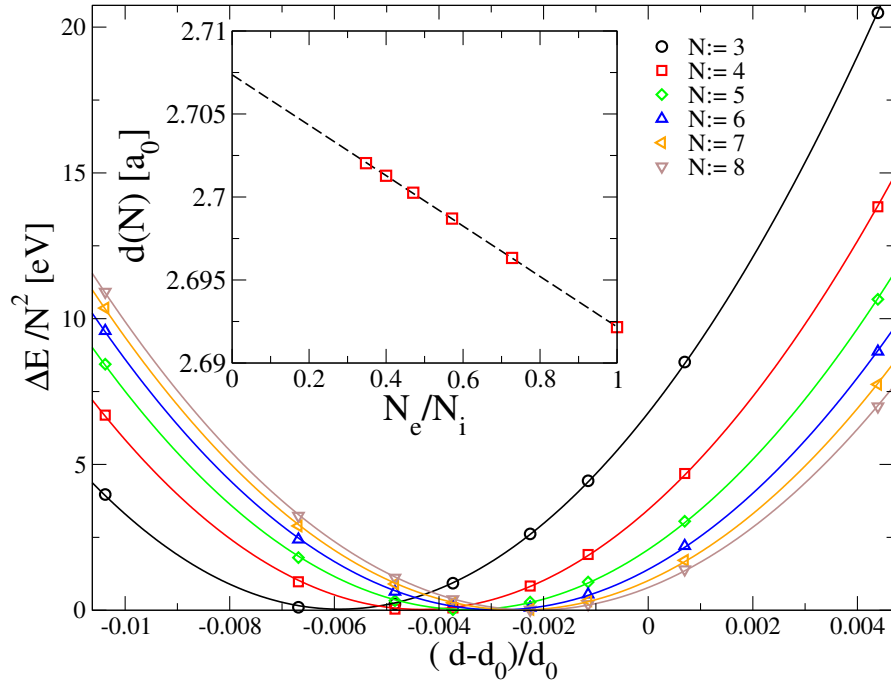


FIGURE 2.8: Excess energy ΔE per unit cell generated by rescaling all bond length, d , (homogeneous, isotropic strain). ΔE exhibits flow of the equilibrium bond length with the linear flake size N . Main panel: ΔE over bond length d employed in the simulation. d is measured relative to the bulk bond length. The lines serve as a guide to the eyes. Inset: Extrapolating the equilibrium bond length $d(N)$ into the bulk limit: $d_0 = 2.707 \pm 0.001$.

terms, which is the discreteness of the electronic spectrum of a finite size flake. Although the convergence of the amplitude with respect to the system size has not been achieved within our DFT study.

2.4 Result: Flake elastic properties

In the previous subsection, the focus was on the behavior of the energy on the flake size under isotropic and shear strain. In this section, we discuss and illustrate what our previous findings imply for the elastic properties of a single flake with a fixed size, N . Partly, we are considering the same set of data again, but now plotting observables directly for N fixed. Here we will explicitly calculate the elastic constants for different finite size flakes. Moreover, we will also present a finite size analysis of the Lamé parameters and show that our finite size analysis recover the correct value in the bulk limit of such a flake.

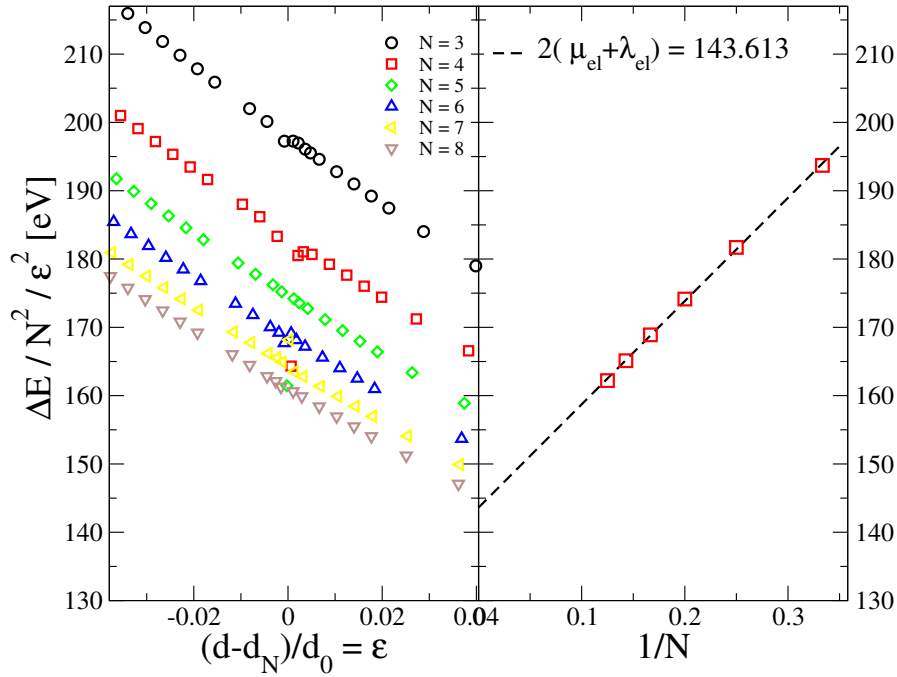


FIGURE 2.9: Estimating the sum of the Lamé parameters $\mu_{\text{el}} + \lambda_{\text{el}}$ and the boundary correction (offset of traces) from ΔE displayed in the previous Fig. 2.8. Left: Data for curvature exhibit a slope which indicates the linear dependency of the Lamé parameter λ_{el} on strain. (Linear terms in μ_{el} do not appear, see Fig. 2.12.) Right: extrapolating the curvature at $\varepsilon = 0$ into the bulk limit.

2.4.1 Homogeneous isotropic strain

Fig. 2.8 shows, how the excess energy per unit cell grows under increasing strain for different flake sizes N . It is readily seen from this plot, that there is a shift of the equilibrium lattice constant $d(N)$ to smaller values. In the light of the previous section, this shift is the expected consequence of the surface induced strain ε_N . The inset shows, the scaling with N_e/N_i .

In addition, we also extract the flake elastic constant $\mu + \lambda$ from the parabolic shape of the curves, Fig. 2.8. To this end, we replot the data in Fig. 2.9 left, so as to highlight the curvature and its strain dependency. On the basis of Eq. (2.9) we can conclude, that the offset of the curves is a consequence of (a) the presence of the surface and the extra energy required for its compression (term N_e/N_i in Eq. (2.9)) and (b) the feedback of the surface strain ε_N into the bulk C-C distance. Extrapolating the zero strain values into the limit, $N \rightarrow \infty$, we find $\mu_{\text{el}} + \lambda_{\text{el}} \approx 71$ per benzene ring matching well our result $\Psi_2/4 \approx 23.5$ per (bulk) bond derived in the previous section, Tab. 2.2, since each ring contributes 3 bonds. This check is displayed in Fig. 2.9, right. The plot also reveals, that the deviation of elastic parameters from their bulk values in small flakes may not be very small. For our

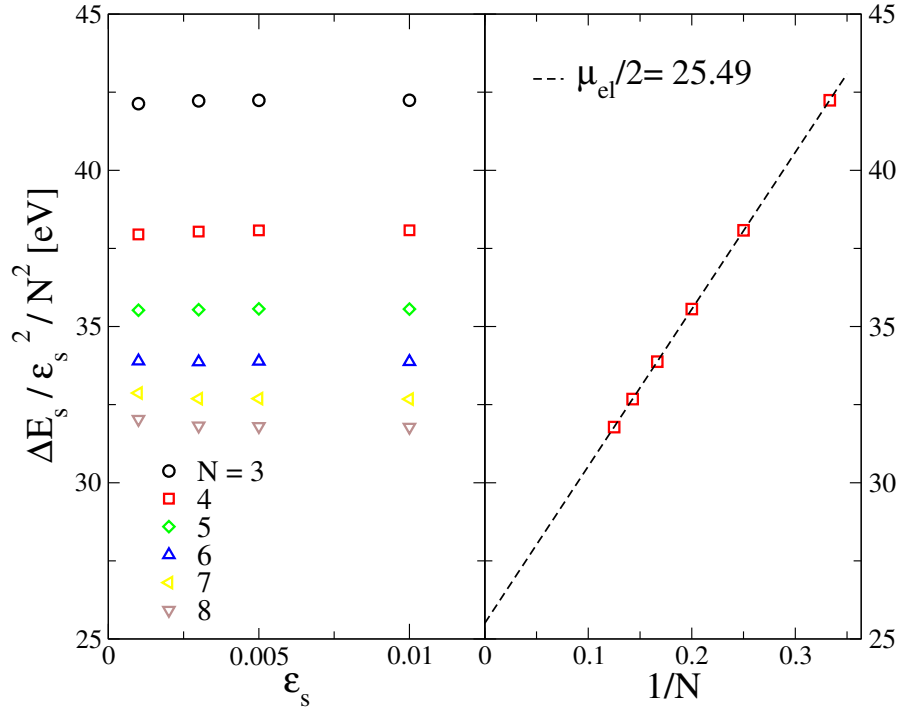


FIGURE 2.10: Estimate for Lamé parameter μ_{el} determined from the excess energy ΔE_s per unit cell under pure shear strain with strength ϵ_s . (Procedure similar to previous Fig. 2.9.) Left panel: dependency of curvature of $\Delta E_s(\epsilon_s)$ on the linear flake size N . Due to mirror symmetries of the unit cell, linear corrections do not appear for the shear parameter μ_{el} . Right: extrapolating the curvature into the bulk limit.

smallest flakes, $N=3$ it reaches almost 30%.

Additional information can be extracted from Fig. 2.9 left, about anharmonicities which manifest themselves in the slope of the curves displayed. This pre-factor of the an-harmonic term (linear in ϵ) in Eq. (2.9) admits the following interpretation. The slope changes with increasing N since the contributions of the surface (ψ_3 -term) and the surface induced bulk compression ($\Psi_4\epsilon_N$ -term) diminish. A non-vanishing value of $\Psi_3/12$ for the slope will remain however even in the bulk limit.

2.4.2 Shear strain

Following the same strategy as we did before with Fig. 2.9, we plot in Fig. 2.10 the excess energy ΔE_s induced by pure shear strain, $\mathbf{u}(\mathbf{x}) = \epsilon_s(0, x)$. Again, the plot emphasizes the curvature in this quantity, μ , and how it evolves with the flake size. Since ΔE_s is even in the shear strain, only positive values of ϵ_s are given. Also, for the same reason an-harmonic terms exist only in the quartic order, so that the

	$d_0[\text{\AA}]$	$\mu_{\text{el}} + \lambda_{\text{el}}[\text{eV}]$	$\mu_{\text{el}}[\text{eV}]$	ν	$Y[\text{N/m}]$
BP86	$1.432^{\pm 0.001}$	$70.715^{\pm 0.011}$	$50.95^{\pm 0.01}$	0.162	356.23
B3LYP	$1.427^{\pm 0.001}$	$71.21^{\pm 0.12}$	-	-	-
PBE	$1.431^{\pm 0.002}$	$69.027^{\pm 0.012}$	-	-	-
Prev. calc.	1.42 [116, 117]	66.571 [117]	49.45 [117]		346 [117]
	1.41 [29]			0.173 [20]	307 [95]
	1.45 [118]			0.16 [118]	336 [118]
				0.31 [89]	312 [89]
				0.149 [119]	345 [119]
				0.179 [120]	341 [120]
Expt. (Graphene)	-	-	-	-	342[[93]]
Expt. (Graphite)	1.421 [121]	-	-	0.165 [122]	371 [123]
	1.422 [123]				

TABLE 2.6: Comparison of C-C-bond distance in bulk graphene, elastic constants, Poisson ratio ($\nu = \lambda/(2\mu + \lambda)$) and Young's modulus ($Y = 2(\mu + \lambda)(1 - \nu)/\mathcal{A}_{\text{ring}}$) as extracted from Fig. (2.8,2.9,2.10) respectively by extrapolating the values in bulk limit ($N \rightarrow \infty$) with previous works. Data is shown for three different functionals we used in DFT calculation. The area of a benzene ring is estimated as $\mathcal{A}_{\text{ring}} = 3\sqrt{3}d_0^2/2$. For the comparison with graphite we assuming graphene thickness of 0.335 nm.

displayed data traces have zero slope. Similar to the previous case of isotropic strain, we also witness here a very strong dependency of the elastic constant on the flake size. In fact, for shear strain it reaches almost 70% for the small system sizes that we are considering.

2.4.3 Buckling induced strain

We present results from an additional DFT study, where we investigate the transverse stiffness of the graphene flake that gives rise to the elastic parameter κ . To this end we employ the following strategy. Each flake has a center pair or center ring of carbon atoms, see Figs. (2.1,2.11). To create a transverse probing field $h(\mathbf{r})$, we lift the center atoms by the distance h_0 over the reference plane. After this, the atomic structure of the flake is relaxed under the constraint, that the set of *edge atoms* (H-atoms and edge C-atoms) can move only within the reference plane; edge

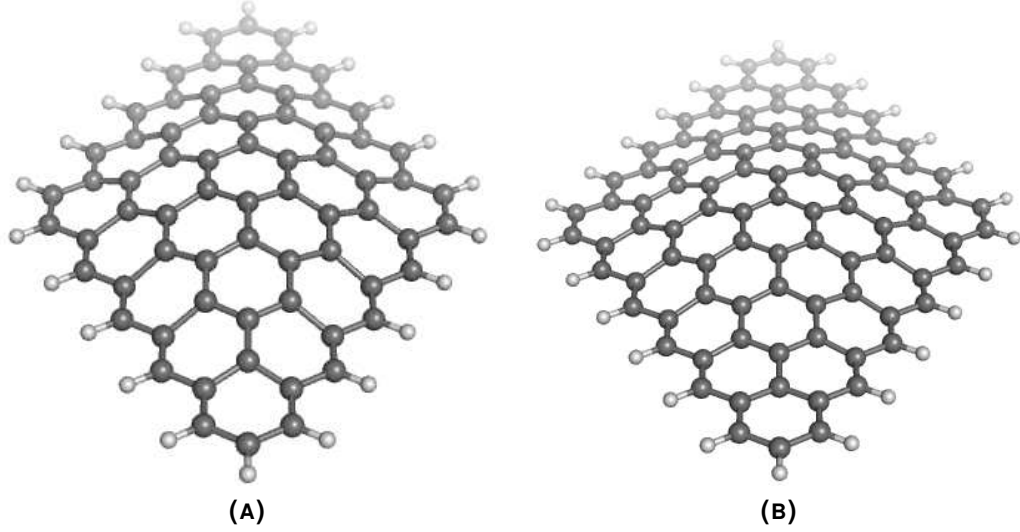


FIGURE 2.11: Buckling flakes of $N=5, 6$ with different central configurations of carbon atoms. The atomic configuration of C atoms is relaxed under the constraint that the center atoms remain at a given height h_0 above the ground plane, while edge atoms (H and C) remain sitting within this plane ($h = 0$).

atoms cannot shift in h -direction². In this way, a flake is equipped with a single ripple while at the same time the associated strain field $\mathbf{u}(\mathbf{x})$ remains negligibly small. In order to estimate the integrated curvature we numerically compute the bi-variate function which interpolates the scattered data values ($h(\mathbf{r})$ -field) at any predefined smooth mesh. We then use this interpolated function to perform the second order numerical derivative at any arbitrary precision.

Fig. 2.12 displays how the excess energy ΔE_h associated with the ripple grows with the increased integrated curvature,

$$I_\kappa = \frac{1}{2} \int d^2\mathbf{r} (\Delta h(\mathbf{r}))^2 \quad (2.22)$$

The increase is linear, as expected from Eq. (2.2) with a slope that is only weakly dependent on the flake size, see inset Fig. 2.12, this implies that nonlinearities remain small as long as the ratio of the ripples amplitude and wave length, h_0/L , does not exceed $\sim 5\%$. The bending rigidity thus found is $\kappa_{el} = 1.24$ eV which is well consistent with the value 1.1eV obtained by Fasolino, Los and Katsnelson[124].

Notice, that there is a significant scattering of almost 20% in earlier theoretical

²The motion of edge atoms in the plane is further restricted in the sense that only conformations have been considered, which can be obtained by a homogenous rescaling of all C-C edge bond lengths.

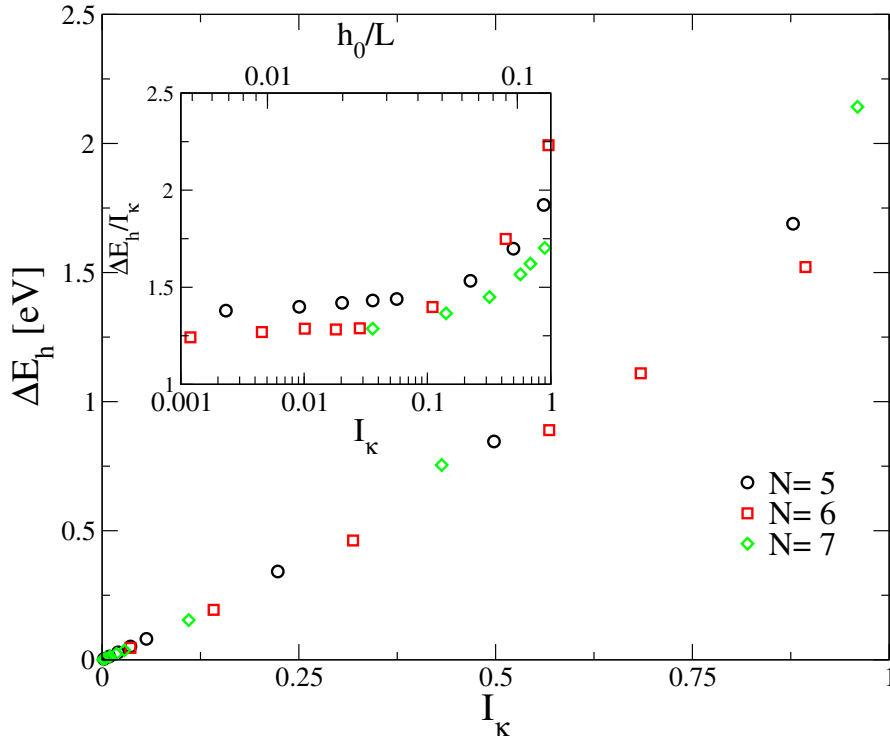


FIGURE 2.12: Estimating the Lamé parameter κ determined from the excess energy ΔE of a bulging flake with maximum height at h_0 over the unperturbed (flat) plane (see Fig. 2.11). Main panel: Change of energy ΔE with the integrated curvature $I_\kappa = \int d^2\mathbf{r} (\Delta h(\mathbf{r}))^2$ for different flake sizes N . Inset: The ratio $\kappa = \Delta E/I_\kappa$ depend on N due to the effect of edge compression.

estimates for κ and derived quantities, see Tab. 2 in Ref. [125]. Discrepancies appear because different theoretical techniques are being employed, e.g. empirical potentials [94] and density functional theory, but also because of modeling artefacts. For example, extracting κ from the elastic energy of carbon nano-tubes (radius R) requires a very careful extrapolation in $1/R$. If sub-leading terms are ignored, there is a pronounced tendency for overestimation, e.g. $\kappa = 1.46$ eV in Ref. [119]. These authors used nano-tubes with smaller tube radius, hence bigger curvature, where nonlinear effects become important. We can check the bending rigidity using the same curvature in Fig. 2.12 (inset) as reported in Ref. [119] and find a reasonable agreement with their value.

2.4.4 Summary and Outlook

In this part we performed an analysis of the elastic properties of small graphene flakes in the DFT framework using different functionals. We show how to extrapolate our results into the macroscopic limit and obtain – where reliable values are

available – good agreement with earlier calculations. Importantly, due to methodological issues, physical quantities calculated based on these methods (DFT) do not always agree with each other. It has been shown that for small two-atomic molecules the error in binding energy for GGA functional reduces by a factor of 5 when comparing to LDA. Thus a careful comparison of results obtained with different functionals, in particular with the hybrid B3LYP, which was until very recently not available in standard band structure codes, is needed. Moreover, we show that for small flakes the value of elastic constants differ considerably from its bulk value, almost 30% for $N=3$.

What has not been investigated systematically in this work is again the higher order effects in elastic constants ($\mu+\lambda$). For instance, in the presence of isotropic strain the higher order terms manifest itself in the slope of the curves displayed in left panel of Fig. 2.9. For shear strain these non-linear effects are not present in the first order of strain because of symmetry, but for large values of strain these effects become extremely important in determining the elastic properties of small flakes.

Further nonlinearities has been observed for the buckling induced strain, i.e. in bending rigidity. Inset of Fig. 2.12 shows the evidence of such nonlinear effect when the ratio h_0/L exceed $\sim 5\%$. A more detailed study is required along these lines in order to understand such non-linear behavior of elasticity in graphene.

Work-function: An extensive progress has been achieved for the fabrication and characterization of graphene in the last few years. Due to its high conductivity and low optical absorption, graphene is also an attractive candidate for transparent conductive electrodes in the field of nano-electronics. However, for effective carrier (electrons or holes) injection by aligning the bands at the Fermi energy between electrodes and semiconducting material, the electrodes need to have a highly tunable work-function. Recently, there have been some proposals about tuning the work-function of graphene by applying electric field or by chemical doping [126, 127]. However, these methods suffer from high flexibility. For instance, by chemical doping with AuCl_3 the work-function of a graphene electrode can be tuned only up to $\sim 0.5\text{eV}$. Although, by applying electric field the flexibility restores but it affects the conductivity of the graphene sample considerably and also the fabrication process becomes less favorable to device application. Strain, however, often appears in sample preparation techniques can be used to modulate the work-function. Our initial analysis suggests that without external strain the deviation of the work-function from large flake of size $N=6$ to small flake, $N=3$, is as large as $\sim 0.4\text{eV}$.

Fig. 2.13 shows the dependence of work-function (ϵ_{HOMO} , HOMO: Highest Occupied Molecular Orbital) with strain for different system sizes. It is readily seen that with increasing system sizes the work-function increases and at larger system sizes it saturates to a constant value near zero strain. The dependency with

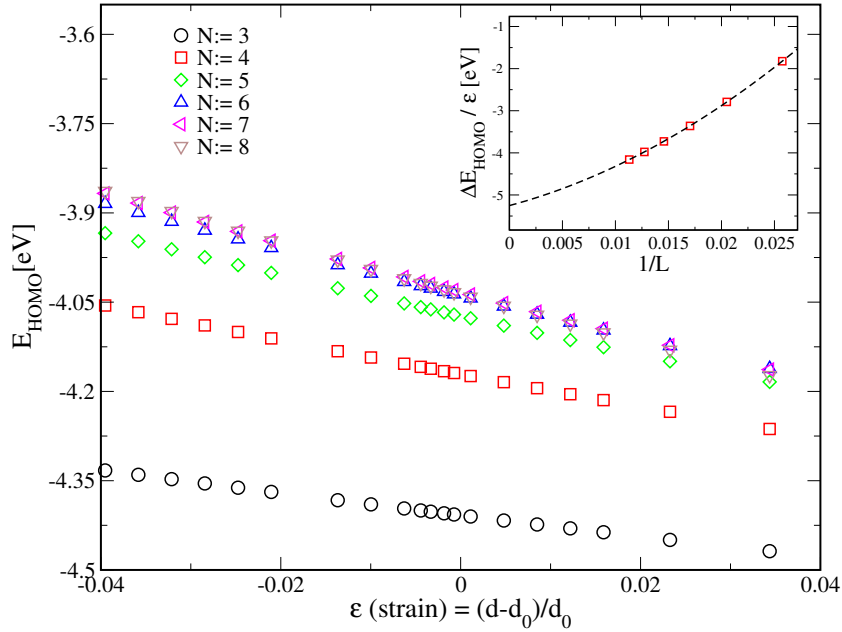


FIGURE 2.13: Main panel: Dependence of the work-function on isotropic strain for different system sizes, N . Data exhibit a slope, which indicates the linear dependency of work-function on isotropic strain, ϵ . Inset: Shows the dependency of the slope with the length of the boundary, L , of the flakes. It shows that the slopes, which measure the sensitivity of the work-function with strain, change significantly from their bulk values in small flakes.

applied strain is also clearly visible from the plot. It indicates a change in the work-function by $\sim 7\%$ by applying a strain of $\sim 1\%$.

In the inset we observe a strong dependency of the slope, $\Delta E_{\text{HOMO}}/\epsilon$, of the work-function on the length of the boundary of the flakes, L , which has been defined in Eq. (2.21). A more thorough study along this line is required to understand this huge sensitivity of work-function with system sizes. Furthermore, it suggests that edges have an important role in determining the work-function of small graphene flakes. A systematic analysis of different edge structures and edge terminations is needed to determine the nature of work-function in small graphene flakes.

2.5 Zero point motion

In this section we extend our analysis of flake elastic properties and take also the zero point motion of the atom cores into account, that constitute the hexagonal lattice. The zero point motion that we consider here is the energy associated with the quantum oscillator motion of the atom cores in its ground state. Now, the energy acquires a second term for every configurations of flake size, N , and bond

distance, d ,

$$F(N, d) = F_{\text{el}}(N, d) + F_{\text{vib}}(N, d) \quad (2.23)$$

with

$$F_{\text{vib}} = \frac{1}{2} \sum_p \hbar \omega_p(N, d) \quad (2.24)$$

where p labels all the flake's vibrational modes. The vibrational excess energy associated with stretching the flake is given by,

$$\Delta F_{\text{vib}} = \frac{\hbar}{2} \sum_p \omega_p(N, d) - \omega_p(N, d(N)) \quad (2.25)$$

where $\omega(N, d(N))$ denotes the vibration energies in the absence of strain and $d(N)$ the equilibrium bond length, see inset Fig. 2.8. Also ΔF_{vib} can be expanded in terms of the slow elastic modes,

$$\Delta F_{\text{vib}}[h, \mathbf{u}] = \frac{1}{2} \int_A d^2\mathbf{r} \gamma_h (\Delta h(\mathbf{r}))^2 - \int_A d^2\mathbf{r} \sum_{ij} \gamma_u^{ij} u_{ij}(\mathbf{r}), \quad (2.26)$$

with expansion parameters γ_h, γ_u that represent averages of Grüneisen parameters over all vibrational modes. Specifically, we have in isotropic media

$$\gamma_h = \hbar \sum_p \omega_p \Gamma_p^h, \quad \gamma_u^{ii} = \hbar \sum_p \omega_p \Gamma_p^{ii} \quad (2.27)$$

where $\Gamma_p^h = \partial \ln \omega_p / \partial h^{ii}$ and $\Gamma_p^{ii} = \partial \ln \omega_p / \partial \varepsilon^{ii}$. In a two-dimensional sample³ with a mirror symmetry one expects $\gamma_u^{xy} = \gamma_u^{yx} = 0$; the change in phonon frequencies should be even in the shear strain, ε_s . Combining Eq. (2.26) with an expansion of ΔF_{el} in full analogy with Eq. (2.2) and after completing the square, we find,

$$\begin{aligned} \Delta F_{\text{el+vib}}(N, d) = & \frac{\kappa_{\text{el}} + \gamma_h}{2} \int_A d^2\mathbf{r} (\nabla^2 h)^2 + \frac{\mu_{\text{el}} + \lambda_{\text{el}}}{2} \int_A d^2\mathbf{r} \left(u_{ii} - \frac{\gamma_u^{ii}}{\mu_{\text{el}} + \lambda_{\text{el}}} \right)^2 \\ & + \frac{\mu_{\text{el}}}{2} \int_A d^2\mathbf{r} (u_{xx} - u_{yy})^2 + u_{xy}^2. \end{aligned} \quad (2.28)$$

For clarity, we have indicated in this expression the bare electronic coefficients (i.e. with frozen atomic cores) by $\kappa_{\text{el}}, \mu_{\text{el}}, \lambda_{\text{el}}$. Likewise, the displacement field $\mathbf{u}(\mathbf{x})$ is defined with respect to the optimum flake geometry ignoring vibrational terms.

In this way we can observe two facts. (i) Vibrations modify the bare transverse stiffness κ_{el} in Eq. (2.28), $\kappa = \kappa_{\text{el}} + \gamma_h$. (ii) Vibrations also affect interatomic distances. The effect can be understood as an effective strain, which stretches the bare C-C distances: $\gamma_u^{ii} / (\mu_{\text{el}} + \lambda_{\text{el}})$. (iii) The change in the C-C bond lengths

³Recall that due to the presence of edge the symmetry group of our sample is lower (D_{2h}) than the one of the unperturbed hexagonal unit cell (D_{6h}).

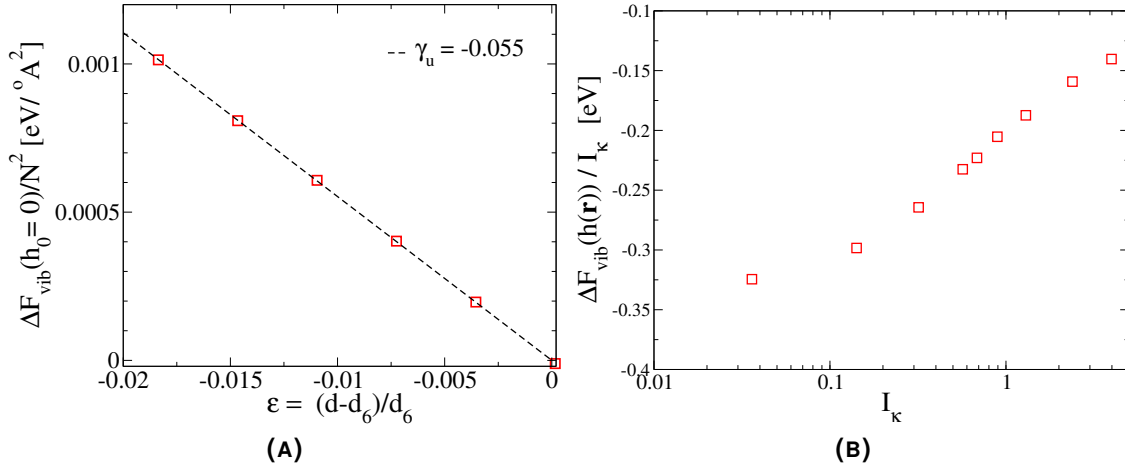


FIGURE 2.14: Left: Dependency of ΔF_{vib} on isotropic strain for system size $N=6$. The slope defines γ_u as in Eq. (2.26). Right: Dependency of ΔF_{vib} on integrated curvature, $I_\kappa = \int d^2\mathbf{r} (\Delta h(\mathbf{r}))^2$, as in Fig. 2.12.

eventually feeds back into all elastic coefficients. Therefore, in a more complete treatment of higher order terms also modifications in $\mu_{\text{el}}, \lambda_{\text{el}}$ would occur.

2.5.1 DFT calculations of Grüneisen parameters

In order to estimate the Grüneisen parameters, γ_h, γ_u , we should calculate the vibrational spectrum of flakes with and without applied strain. To this end we adopt the following procedure. For every flake size, N , we find the atomic geometry with the optimal electronic energy, see e.g. Fig. 2.1. This constitutes the set of freely relaxed “parent states”. The relaxation ensures the Hessian, that characterizes interatomic forces, to become a positive definite matrix.⁴ In the present study we focus on the impact of phonons on the bulk elastic constants. There we may eliminate contributions of surface vibrations by assigning an infinite mass to the surface H and C atoms. Other than this, the calculation of vibrational modes and frequencies for the relaxed flake is a standard procedure[128, 129]. Thereafter, each parent state thus obtained is used in order to create two new families. The first family is constructed to obtain γ_u . It derives by changing the bond length of edge C-C-pairs by a factor of $1 + \varepsilon$ keeping all atoms still inside the base plane ($h=0$). For each value ε the internal C-atoms are relaxed and the vibrational spectrum together with the average strain field, $I_u(\varepsilon) = \int d\mathbf{r} (u_{xx} + u_{yy})$, are recalculated. In this process it is important to have edge atoms at infinite mass. This ensures that the flake energy is in a (constrained) minimum so that all frequencies

⁴This relaxation process is the limiting computational step. For a flake with $N = 6$ it took several days on a single Opteron processor. For $N=6$ a single iteration takes about 1 day and for full convergence one needs typically 30-50 days depending on the flake size.

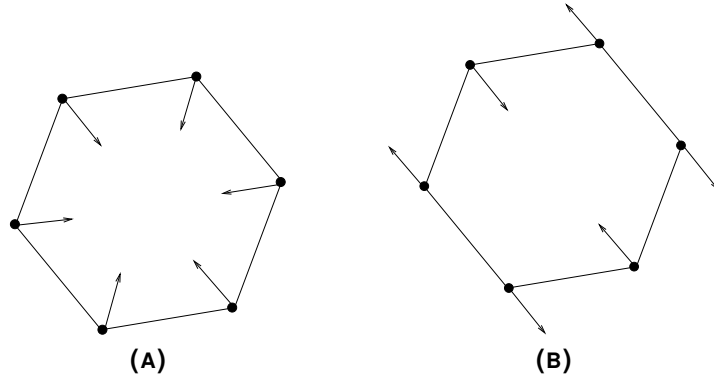


FIGURE 2.15: Schematic diagram of vibrating modes that give rise to D(left) and G(right) peaks in Raman spectra of graphene.

are real.

In order to determine γ_h a second family has been constructed. It consists of the buckled flakes, Fig. 2.11, that we have studied in the previous section in order to extract κ_{el} . Again, after assigning infinite mass to the edge atoms for each family member, the vibrational spectrum and the consecutive modification of the zero point energy can be calculated.

2.5.2 Results and Discussion

In Figs. 2.14 the change in the zero point energy, ΔF_{vib} , is plotted over the integrated strain fields. The Grüneisen parameters are given by the slope near zero strain; their numerical values are listed in Tab. 2.7. For a discussion of our results we first recall, that the vibrational spectral density of states of the carbon sheet has a strong peak in the optical frequency regime, c.f. Fig. 2.16, near 1600 cm^{-1} . It is the “G-peak”, that corresponds to an in-plane mode, where neighboring atoms vibrate in opposite direction as depicted in Fig. 2.15 (right). This mode gives the

	BP86, $N=6$	Prev. calc.	Expt.
γ_u [eV/Å ²]	-0.055	-	-
γ_h [eV]	-0.32	-	-
$\gamma_u/(\mu_{el} + \lambda_{el})$	-0.004	-	-
γ_D	2.6	2.7 [116]	
γ_G	2.2	2.0 [130]	1.99 [97, 101]

TABLE 2.7: Survey over the fitted Grüneisen parameters extracted from the data Fig. 2.14 and Fig. 2.16 respectively. For the definitions of $\gamma_{u,h}$ see Eq. (2.27).

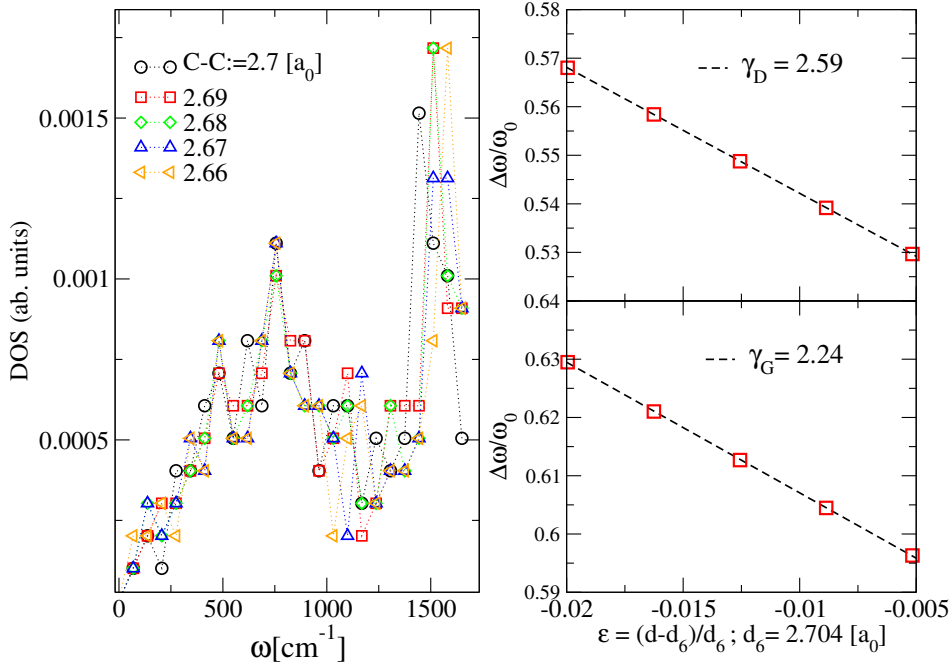


FIGURE 2.16: Left panel: Phonon density of states for the flake of size $N=6$. Data sets are shown for different C-C bond distances. Upper right panel shows the flow of D-peak with in-plane strain. Lower right panel shows the variation of Raman G-peak with strain, where ω_0 is the Raman band frequency ($\approx 2680 \text{ cm}^{-1}$)[100]. The corresponding vibration modes are shown in Fig. 2.15.

dominating contribution to the total zero point energy. Another significant contribution comes from the frequency range $500 - 1000 \text{ cm}^{-1}$, where one observes the mixing of out-of-plane modes with in-plane modes. A third important mode is the “D-peak” near 1350 cm^{-1} , that reflects the breathing mode as shown in Fig. 2.15 (left). This mode is particularly interesting when studying finite size(edge) effects in graphene flakes. The reason is that, in bulk graphene the coupling of the D-peak to the electromagnetic fields is suppressed, since the D_{6h} -symmetry of the hexagonal unit cell remains intact and inhibits the formation of the dipole moment. By contrast, in flake with an overall symmetry that is lower than D_{6h} , the D-peak is observable with a strength proportional to the inverse flake size.

Therefore, we can understand the sign of γ_h as a consequence of a softening of these modes in the sample regions with non-zero curvature $(\Delta h(\mathbf{r}))^2$. Similarly, γ_u is negative, indicating the increase of the atomic oscillator frequency that occurs when the interatomic distance is diminished. While the sign of $\gamma_{h,u}$ was not unexpected, it is noteworthy that the vibrational contributions to the phenomenological material parameters are actually not so small. The bare electronic bending rigidity, κ_{el} is reduced by as much as 26% down to $\kappa = \kappa_{el} + \gamma_h = 0.88 \text{ eV}$. Similarly, when expressing the effect of vibrations on the atomic lattice as an effective strain pushing the atoms to larger distances, then this strain reaches values up to 0.4%.

Here, we also calculate the Grüneisen parameters associated with individual modes (see Fig. 2.15). The right panel in Fig. 2.16 shows the flow of the Raman frequencies (upper half D, lower G) with the applied strain. The frequency decreases linearly (as described in Eq. (2.26)) with decreasing compression due to anharmonicity of the interatomic potential. The slope essentially estimates the Grüneisen parameters, γ_G and γ_D for the vibrations shown in Fig. 2.15. Our results for γ_G , γ_D are consistent with the earlier experiments and first principal calculations (see Tab. 2.7) available in literature[97, 101, 116, 130].

2.5.3 Summary and Outlook

In the last part of this work we studied the effect of zero-point motion on the elastic constants. We see that the effect of phonon manifests itself in two distinct way, a) it renormalizes the C-C bond distance by changing the effective strain in the system, and b) it renormalizes the bending rigidity, κ , significantly about 26%. Furthermore, we show in which way the phonon spectrum of small flakes differs from the bulk limit. Specifically, due to the edge induced compression of the flake's interior, the Raman-G-peak undergoes a blue shift that is indicative of the flake size (and in principle also its chemical edge termination).

Again the effect of higher order phonon contributions has been left out in this work. For instance, the G'-peak, which is the second order peak of zone boundary phonons (represented by the D-peak in the Raman spectra) and lies at around 2700 cm^{-1} has not been investigated. Moreover, experiment suggests that at larger values of uniaxial strain ($\sim 0.8\%$) the G-peak splits in two separate peaks, G^+ , G^- [97]. Further study is required to identify, for instance, the corresponding Grüneisen parameters and the effect on the elastic properties.

Another interesting aspect is the effect of “flexural” phonons (out-of-plane modes) on elastic properties of graphene. It is particularly interesting in the context of transport experiments, where it has been shown that the flexural phonons dominate the phonon contribution to the resistivity, $\rho \sim T^{5/2} \ln T$, below a crossover temperature, T_x [131]. It has been argued that the mixing of bending and stretching modes in such a scenario give rise to the logarithmic factor in the resistivity. In a similar spirit, the effect of such mixing at finite temperature in the elastic properties of graphene could be an interesting to study. Moreover, as observed in our study that the effect of edges can be highly relevant when considering elastic properties of flakes. Thus at finite temperature how the mixing of different phonon modes is affected in the presence of edges is certainly a new direction for further studies.

Finally, the finite size analysis of phonon spectra was not performed in our analysis due to excessive computational cost. As mentioned earlier that the phonon calculations are not only time consuming, it is also particularly difficult to achieve

convergence in larger flake size within standard DFT framework as it has a $O(N^4)$ scaling with system size, N . A different approach is required to address this issue in more detail.

3

CHAPTER 3

Graphene: Zero Modes and Transport

As discussed in the introduction, disorder in graphene plays a fundamental role in determining its transport properties. A ‘vacancy’, which may be realized by removing a carbon atom from a regular graphene lattice, belongs to a special class of disorder that introduces zero modes in the low energy spectrum of graphene. Other natural ways of realizing a vacancy approximately adding a strong on-site potential to a single carbon atom or by adding hydrogen (or molecules) ad-atoms that change the hybridization of carbon from sp^2 to sp^3 . A vacancy or resonant scatterer has many different consequences; for instance, it has been shown that in the presence of a perpendicular magnetic field it introduces extra states between two consecutive Landau levels [132]. Another aspect of vacancies that has been studied quite extensively is vacancy induced magnetism [133]. By combining a mean-field approach with a first-principles calculation it has been shown that the total magnetic moment of a graphene lattice in the presence of vacancies is essentially given by the difference of atoms in the two sub-lattices [134, 135].

Moreover, from the perspective of transport, the absence of localization in graphene (see Chapter 1) is believed to be due to either long range disorder or for disorder that preserves the chiral symmetry of graphene. One possible candidate for such disorder are vacancies, such that they preserve the chiral nature of the Dirac fermions. In this chapter we explore possible consequences of vacancies on the transport characteristics of graphene.

The chapter is organized as follows. In the first part we discuss in detail the effect of a vacancy on the low energy spectrum of graphene and the corresponding effects on its density of states (DoS). In this part we develop a numerical method based on the time evolution of the time-dependent Schrödinger equation, which is particularly suited to calculate the DoS of large systems. This part of the work is in

collaboration with a diploma student in our group, Victor Häfner [136]. Together with Victor we develop the code and analyze the data for the DoS. Because of this we present a part of our joint work in this thesis.

In the next part we collaborate with P. Ostrovsky [137], where he provides us the analytical model and a general theory of transport in graphene in the presence of a resonant scatterer. In this work we support his analytical model with numerical simulations, where he also provides an efficient numerical tool to calculate conductivity at large concentration of vacancies. Our numerical simulation yields the dependence of the conductivity for several vacancy concentrations in different sub-lattices at the charge neutrality point of graphene.

3.1 Electronic properties of vacancies

Chiral nature of Dirac fermions: As mentioned in section 1.1 the dispersion of graphene follows a linear energy-momentum relation, which is obtained formally by solving the two-dimensional massless Dirac equation. It is now easy to show that the low-energy effective Hamiltonian near the \mathbf{K} point in the AB space (sub-lattice space) has the following block structure,

$$H_{\mathbf{K}} = \hbar v_F \boldsymbol{\sigma} \cdot \mathbf{p} = -i\hbar v_F \begin{pmatrix} 0 & \partial_x - i\partial_y \\ \partial_x + i\partial_y & 0 \end{pmatrix} \equiv \begin{pmatrix} 0 & \mathbf{t} \\ \mathbf{t}^\dagger & 0 \end{pmatrix} \quad (3.1)$$

where, $\mathbf{t} = p_x - ip_y$, and $\boldsymbol{\sigma} = \{\sigma_x, \sigma_y\}$ acts on the AB space of the graphene lattice. v_F is the Fermi velocity. In order to distinguish from the real electron spin, the components of the Pauli matrices, σ_i , refer to the “pseudo-spin”. The pseudo-spin wavefunction of the corresponding Hamiltonian, Eq. (3.1), in the momentum space around the \mathbf{K} point is,

$$\psi_{\pm, \mathbf{K}}(k) = \frac{1}{\sqrt{2}} \begin{pmatrix} e^{-i\theta_k/2} \\ \pm e^{i\theta_k/2} \end{pmatrix} \quad (3.2)$$

where the \pm signs corresponds to two eigen energies of two different bands (π and π^*), $E = \pm v_F k$ (see Chapter 1), and $\theta_k = \arctan(k_x/k_y)$ is the angle in momentum space. The wavefunction corresponding to the other \mathbf{K}' point is related by the time reversal symmetry, $k \rightarrow -k$. This two-dimensional natures of the wave-function corresponds to the pseudo-spin symmetry intrinsic to graphene.

The pseudo-spin, $\boldsymbol{\sigma}$, has two eigenvalues corresponding to the operator, $\hat{\mathbf{h}} = \boldsymbol{\sigma} \cdot \mathbf{p}/p$. This is because the states, $\psi_{\mathbf{K}}$, are also eigenstates of the operator $\hat{\mathbf{h}}$ [3]:

$$\hat{\mathbf{h}}\psi_{\mathbf{K}}(\mathbf{r}) = \pm \frac{1}{2}\psi_{\mathbf{K}}(\mathbf{r}) \quad (3.3)$$

and a similar equation for $\psi_{\mathbf{K}'}(\mathbf{r})$. Positive chirality (i.e. eigenvalue of $\boldsymbol{\sigma}$ in the

direction of the momentum \mathbf{p} , ‘ \uparrow ’) signifies a particle state; similarly the negative chirality (antiparallel orientation, ‘ \downarrow ’) denotes a hole state in graphene. This particular property implies that the states near the Dirac point have a well defined *chirality* or helicity, which essentially reflects the sub-lattice structure of the graphene lattice. Chirality in graphene is a conserved quantity (good quantum number close to the Dirac points) in the asymptotic limit as the Hamiltonian commutes with the Pauli matrices. Furthermore, the chiral nature of the Dirac quasi-particles also appears in the energy dispersion of graphene, where two linearly independent energy branches touch each other at the Dirac point. Note that due to the presence of a next nearest neighbor hopping (t') or at larger energies the chirality no longer remains a good quantum number. Consequently, it breaks the particle-hole symmetry of the energy dispersion.

Another way of looking at the chirality is by considering the block representation of the Hamiltonian, Eq. (3.1). The eigenvalues of this Hamiltonian is given by the Schrödinger equation as,

$$\begin{pmatrix} 0 & \mathbf{t} \\ \mathbf{t}^\dagger & 0 \end{pmatrix} \begin{pmatrix} \phi_A \\ \phi_B \end{pmatrix} = E \begin{pmatrix} \phi_A \\ \phi_B \end{pmatrix} \quad (3.4)$$

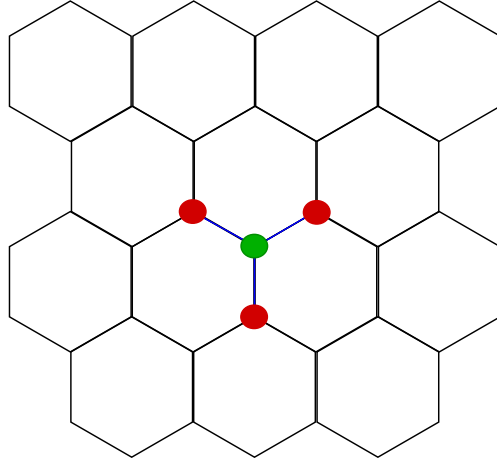
Rewriting the eigenvalue equation one gets,

$$\left. \begin{array}{l} \mathbf{t} \phi_B = E \phi_A \\ \mathbf{t}^\dagger \phi_A = E \phi_B \end{array} \right\} \Rightarrow \mathbf{t} \mathbf{t}^\dagger \phi_A = E^2 \phi_A \quad (3.5)$$

and therefore, the block structure of the Hamiltonian suggests a set of eigenvalues with energies E and $-E$. Thus chirality of the Dirac particles guarantees that the eigen-energies always come in pairs, i.e. particle-hole symmetry.

Single vacancy: A vacancy is a special kind of disorder that brings important consequences in the low energy physics of graphene. For instance, a single vacancy introduces a zero energy state in the electronic spectrum of graphene exactly at the boundary of the conduction and valence band. The emergence of the zero energy state can be understood by considering an atom in the regular tight-binding lattice, where hopping from the neighboring carbon atoms is forbidden (see Fig. 3.1). In such a situation the isolated carbon has a Hilbert space dimension of one with a predefined on-site energy (see Eq. (3.1)). With the unattached site (or vacancy) the new physical dimension of the Hilbert space is: $\dim_R(\mathcal{H}) = N - 1$, where $N = N_A + N_B$ with N_A (N_B) being the number of carbon atoms in A (B) sub-lattice. Let us start with a symmetric situation where number of carbon atoms are equal in both the sub-lattices, $N_A = N_B$. Upon removal of one atom from one of the sub-lattices one creates an imbalance between the sub-lattices; consequently it reduces the dimension of the old Hilbert space by one leaving the energy spectrum asymmetric. In such a scenario the particle-hole symmetry (chirality) of the energy spectrum guarantees an extra state ($N_A - N_B = 1$) that sits exactly at the zero

FIGURE 3.1: Pictorial representation of a vacancy in a regular graphene lattice. Green circle (●) represents an isolated carbon atom, which signifies the presence of a vacancy in graphene lattice. The blue line (—) denotes no hopping from neighboring carbon atoms to the isolated one.



energy.

Finite concentration of vacancies: For a finite concentration of vacancies the above situation changes depending on the distribution of vacancies between two sub-lattices. For example, when vacancies are distributed only in one of the sub-lattices the number of zero modes is exactly given by the number of vacancies. This can be understood from the intuitive argument that we have presented earlier for a single vacancy. For instance, let us consider a situation where we start with n number of atoms in both the sub-lattices, and after removal of atoms from one of the sub-lattice (B) we arrive with a situation when A sub-lattice contain n atoms and the sub-lattice B contains only m ($< n$) atoms. In this situation the block structure (Eq. (3.1)) of the Hamiltonian has the following form,

$$H_{\mathcal{K}} = \left(\begin{array}{c|c} & \begin{matrix} \vdots \\ 0 & \vdots & t \\ \vdots \\ \hline \vdots \\ t^\dagger & \vdots & 0 \end{matrix} \\ \hline & \end{array} \right) \left. \begin{array}{l} \} n \\ \\ \} m \end{array} \right) \quad (3.6)$$

where $n > m$. Using the above eigenvalue equation, Eq. (3.4), one gets two different equations with same set of eigen energies, E^2 , as,

$$\begin{aligned} t^\dagger t \phi_B &= E^2 \phi_A \Rightarrow \dim(n \times n) \\ t t^\dagger \phi_A &= E^2 \phi_B \Rightarrow \dim(m \times m) \end{aligned} \quad (3.7)$$

Now in order to construct a solution out of these above equations the minimum number of zero eigenvalues has to be $n - m$. In this way we can only prove the number of “minimum” zero eigenvalues originating from the imbalance between

the sub-lattices. A more formal proof can be given using the “index” theorem.

Similarly a different situation arises, when vacancies are distributed randomly (far from each other such that they do not hybridize) over the two sub-lattices, the number of zero modes is given by the sub-lattice imbalance, i.e. $N_A - N_B$ in the limit of an infinite system size, $N \rightarrow \infty$ (thermodynamic limit). In this situation the exact number of zero modes is confirmed by the symmetric nature of the energy spectrum (or chiral nature of the Dirac fermions) as discussed earlier. This intuitive picture of the origin of zero modes in graphene has been verified thoroughly by a theorem in linear algebra (‘index theorem’) by Castro Neto et. al. [138]. Furthermore, it has been shown that the exact analytical wavefunction associated with a zero mode has the following form [57],

$$\Psi(x, y) \propto \frac{e^{i\mathbf{K}' \cdot \mathbf{r}}}{x + iy} + \frac{e^{i\mathbf{K} \cdot \mathbf{r}}}{x - iy} \quad (3.8)$$

The wavefunction decays as $\sim \frac{1}{r}$ with the distance to the vacancy and thus is quasi-localized. Moreover, it has been shown that the wavefunctions are linearly independent and are localized only on the *majority* sub-lattice.

The above theorem as well as our intuitive argument based on the chiral nature of graphene quasi-particles excludes the existence of zero modes when vacancies are distributed equally in both the sub-lattices. However, our numerical simulation in a finite size graphene sample suggests that the zero modes survive even in the limit of small concentration of vacancies. The origin of zero modes in this scenario needs further clarification.

3.2 Density of States

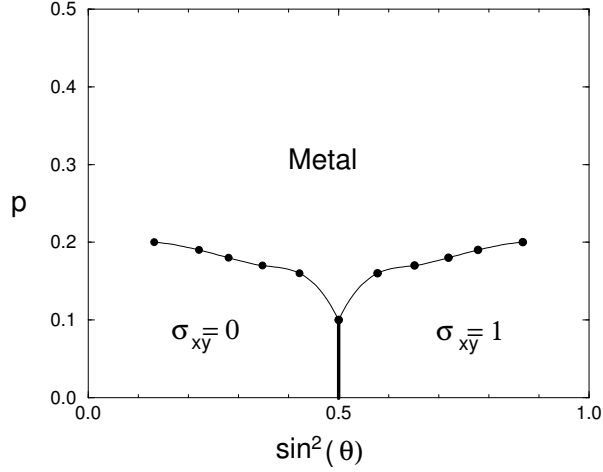
The density of states (DoS) of a system determines the number of states available within a given energy window, $E, E + dE$. It is an important concept in condensed matter physics; for instance, the DoS plays a significant role in analyzing critical properties of systems in different spatial dimensions.

For example, a two-dimensional disordered superconductor with broken time-reversal and spin-rotation invariance, e.g. $p_x + ip_y$ pairing, which exhibits plateaus of the thermal quantum Hall coefficients, is a possible representation of the class D (see Tab. A.1). The Cho-Fisher model ¹, being a generic model for the thermal

¹This is a generic model of symmetry class D. In order to obtain the model one starts with the ordered Chalker-Coddington Network model. From this model the Cho-Fisher model is obtained by allowing independent fluctuations of the node parameters, θ_i , with some distribution function $\mathcal{P}(\theta)$. In this particular situation the distribution function is given by

$$\mathcal{P}(\theta) = (1 - p)\delta(\theta - \theta_0) + \frac{p}{2}\delta(\theta + \theta_0) + \frac{p}{2}\delta(\theta + \theta_0 - \pi)$$

FIGURE 3.2: Phase diagram of the Cho-Fisher model depicting three phases as calculated numerically using transfer-matrix technique in Ref. [139]. p denotes the concentration of vortex disorder and $\sin^2 \theta$ measures the inter plaquette tunneling probability. Figure is adapted from Ref. [139].



quantum Hall effect established by Chalker *et al.* [139], indeed exhibits all the three phases as shown in Fig. 3.2. It has been shown by numerical simulation of the Cho-Fisher model that the DoS has a logarithmic divergence as $E \rightarrow 0$ for sufficiently large concentration of defects, p . This is the metallic phase as denoted in the phase diagram, Fig. 3.2. For small concentration of defects the DoS becomes finite at $E = 0$ indicating a phase transition into the localized regime [140]. In between these phases, the DoS vanishes as $E \rightarrow 0$ and agrees with the behavior $\rho(E) \sim |E| \ln(1/|E|)$, which is derived from the theory of Dirac fermions with random mass disorder. As seen that by analyzing the DoS it is indeed possible to describe different phases arising from different considerations; as seen in class D that the localized phases and the transition between them can be mapped out using the knowledge of DoS [66].

In the next subsections we show how in the presence of disorder the DoS of graphene modifies with respect to the clean DoS. In the first part we describe the method for our numerical simulation used to determine the DoS. Next we discuss the results along with an outlook of the work.

3.2.1 Method

We consider a nearest neighbor tight binding model to represent the de-localized π electrons of a graphene lattice,

$$H = -t \sum_{\langle i,j \rangle} \left(c_i^\dagger c_j + c_j^\dagger c_i \right)$$

where p is the disorder concentration. This amounts to flipping signs in $\sin \theta$ (or $\cos \theta$) associated with each node [66].

where, c_i (c_j^\dagger) represents the annihilation (creation) operator on site i of the lattice. In order to calculate the DoS we could diagonalize the Hamiltonian to acquire all the eigenvalues and the corresponding eigenvectors. However, the drawback of this method is that it is very much limited with the system size. For instance, to see the true bulk like behavior of the DoS, particularly in the presence of disorder, one needs to have an access to much larger system sizes than what full diagonalization can achieve, which is of the order of 10^4 sites only. In order to approach larger system sizes (at least 100 times larger, see Fig. 3.3) we employ a method based on time evolution of time-dependent Schrödinger equation (see Ref. [141] for detail) in collaboration with Häfner et. al. [136]. This is a very powerful numerical method which allows to propagate wave packets for long times. By observing these wave-packets one can calculate the electronic density of states and also the conductivity of the graphene sheet with greater accuracy and for bigger system sizes.

The main idea behind this method is to take a random superposition of eigenstates, $|\phi(0)\rangle$ as an initial state,

$$|\phi(0)\rangle = \sum_i a_i |i\rangle \quad (3.9)$$

where, $|i\rangle$ is the basis set and $\{a_i\}$ are the coefficients of random complex numbers. Next, we evolve the initial state in time according to,

$$|\phi(\delta\tau)\rangle = e^{iH\delta\tau} |\phi(0)\rangle \quad (3.10)$$

where, $\hbar=1$. Thereafter one calculates the correlation function at each time step, $\delta\tau$,

$$\mathcal{C}(\delta\tau) = \langle \phi(0) | \phi(\delta\tau) \rangle \quad (3.11)$$

Discrete Fourier transform of such a correlation functions at each time step gives the local DoS,

$$\varrho(\varepsilon) = \frac{1}{2\pi} \int_{-\infty}^{\infty} e^{i\varepsilon\tau} \langle \phi(0) | e^{iH\tau} | \phi(0) \rangle d\tau. \quad (3.12)$$

Now, in principle, to get the DoS averaging over the initial random vector is needed; however, for large enough system size ($\sim 10^6 - 10^8$ atoms in a lattice) the local DoS is essentially the DoS as it already contains sufficient number of eigenstates. Note that the observation time determines the resolution in the energy space. Thus a long observation time is required in the simulation in order to observe the true behavior of the DoS. For the result presented here, we choose the following parameters: the hopping amplitude $t = 1$, time resolution $\delta\tau = 0.05$, and total observation time, $\tau = 32000$ steps.

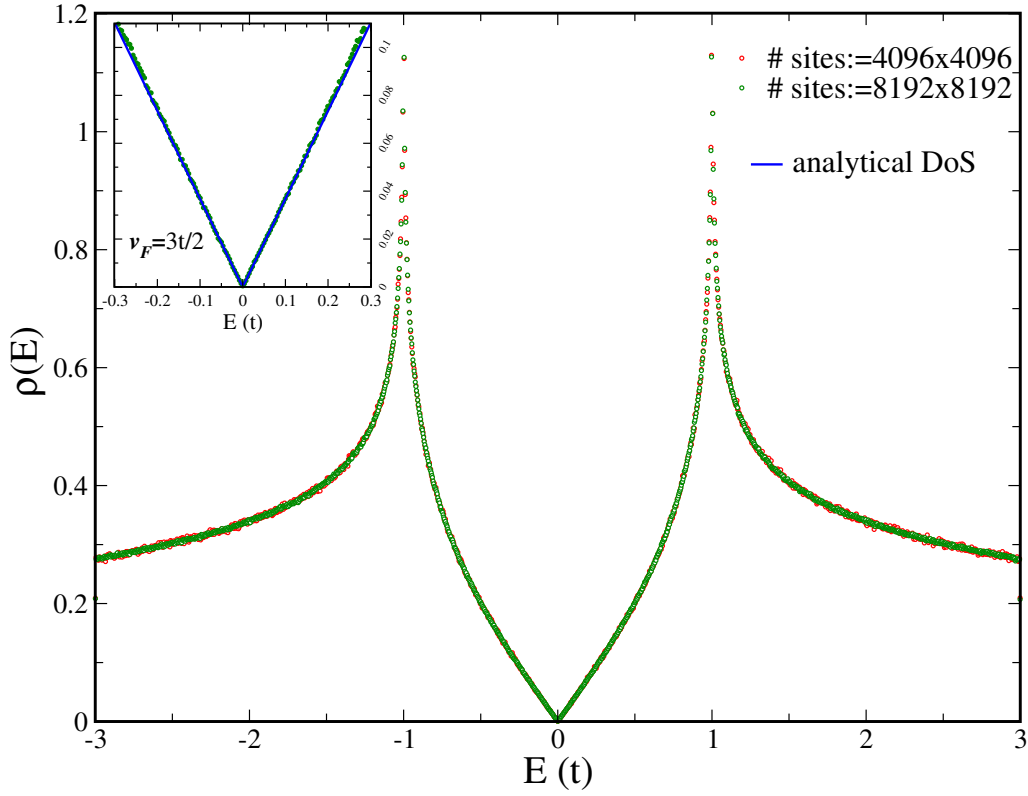


FIGURE 3.3: Density of states of a clean graphene lattice as a function of E (in units of t , where $t=1$ and lattice constant $a=1$). The DoS is calculated using a nearest neighbor tight binding model. Inset: Shows the linear behavior of the DoS close to the Dirac point. The solid line (—) shows the analytical DoS at low energies. Picture courtesy Häfner et al. [136].

3.2.2 Clean graphene

Deriving the DoS of clean graphene from its dispersion relation (Eq. (1.5)) is a standard exercise [3]. The analytical expression for the DoS per unit cell for $t' = 0$ is ,

$$\varrho(E) = \frac{4}{\pi^2} \frac{|E|}{t} \frac{1}{\sqrt{Z_0}} \mathbf{F} \left(\frac{\pi}{2}, \sqrt{\frac{Z_1}{Z_0}} \right) \quad (3.13)$$

where, $\mathbf{F}(\pi/2, x)$ is a complete elliptic integral of first kind. Following Ref. [3] Z_0 and Z_1 is give by,

$$Z_0 = \begin{cases} \left(1 + \left|\frac{E}{t}\right|^2\right) - \frac{\left(\left(\frac{E}{t}\right)^2 - 1\right)^2}{4}; & -t \leq E \leq t \\ 4\left|\frac{E}{t}\right|; & -3t \leq E \leq -t \vee t \leq E \leq 3t \end{cases}$$

$$Z_1 = \begin{cases} 4\left|\frac{E}{t}\right|; & -t \leq E \leq t \\ \left(1 + \left|\frac{E}{t}\right|^2\right) - \frac{\left(\left(\frac{E}{t}\right)^2 - 1\right)^2}{4}; & -3t \leq E \leq -t \vee t \leq E \leq 3t \end{cases} \quad (3.14)$$

The DoS of a graphene lattice containing $\sim 6 \times 10^7$ sites obtained from the numerical simulation is shown in Fig. 3.3. Near the Dirac point the dispersion becomes linear,

$$E(k) \simeq v_F k + \mathcal{O}(k^2) \quad (3.15)$$

where, $v_F = 3t/2$ is the Fermi velocity. Finally, in this limit the DoS per unit cell including spin and valley degeneracy is given by,

$$\varrho(E) = \frac{2\mathcal{A}_c |E|}{\pi v_F^2}. \quad (3.16)$$

where, $\mathcal{A}_c = 3\sqrt{3}a^2/2$ is the area of a unit cell (hexagon). The linear behavior of the DoS is shown in the inset of Fig. 3.3, which confirms our numerical investigation. Another aspect of the DoS that is also clearly visible in the numerical simulation, Fig. 3.3, is the Van Hove singularity, which is due to appearance of critical points in energy dispersion near the Brillouin zone boundary.

3.2.3 Graphene with vacancy

In this section we investigate the DoS in the presence of a finite concentration of vacancies in a graphene lattice. In this context at least two situations are possible: vacancies distributed in only one sub-lattice ($n_A = n_{\text{imp}}, n_B = 0$) and vacancies distributed equally in both of the sub-lattices ($n_A = n_B = n_{\text{imp}}/2$). Intermediate situations appear when a finite number of vacancies is distributed unequally in both the sub-lattices. Below we only discuss the former situations leaving out the later for further investigation.

Vacancies in one of the sub-lattices: According to the argument based on a single vacancy in this situation the number of zero modes due to a finite concentration of vacancies is exactly equal to $n_A - n_B$, where n_A (n_B) is the number of vacancies in sub-lattice A (B). Thus in the DoS we observe a peak at the zero energy corresponds to the number of zero modes in the low energy spectra. Fig. 3.4 shows the evolution of DoS with different vacancy concentrations. The inset of Fig. 3.4 shows the evolution of a sub-gap close to the Dirac point.

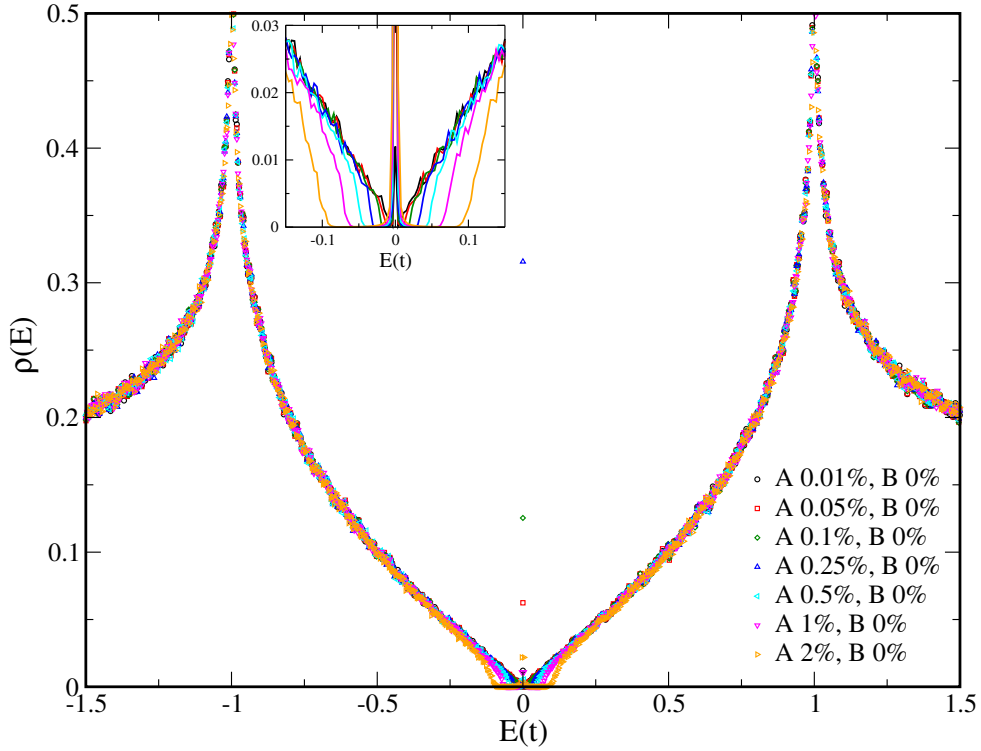


FIGURE 3.4: Density of states of graphene in the presence of different concentration of vacancies in one sub-lattice. The simulation is performed in a graphene lattice containing $\sim 4 \times 10^6$ atoms. With increasing vacancy concentrations not only the peak height increases but also a gap develops near the Dirac point. Inset: Details of the region close to the Dirac point ($E = 0$) is shown. The evolution of the sub-gap near the zero energy is observed by changing the vacancy concentrations in one sub-lattice.

In Fig. 3.5A we plot the number of zero modes associated with the central peak for different vacancy concentrations. The number of zero modes is obtained by calculating the weight under the δ -peak at zero energy,

$$\mathcal{N} = \int_{-\Delta}^{\Delta} \varrho(E) dE, \quad (3.17)$$

where 2Δ is the energy interval defined close to zero energy. It is readily seen from the plot that the number of zero modes, \mathcal{N} , grows linearly as the concentration of vacancy increases. The quantitative estimate matches with the expected number of zero modes from the intuitive argument (chirality) presented above as seen in Fig. 3.5.

In addition, we also extract the magnitude of the sub-gap, ΔE_g , close to the Dirac point from Fig. 3.4. To this end we plot the data (Fig. 3.5B) as a function of $\sqrt{n_{\text{imp}}}$, so as to highlight the flow of the gap with different vacancy concentrations. A power law fit indicates that dependence of the sub-gap with vacancy concentration

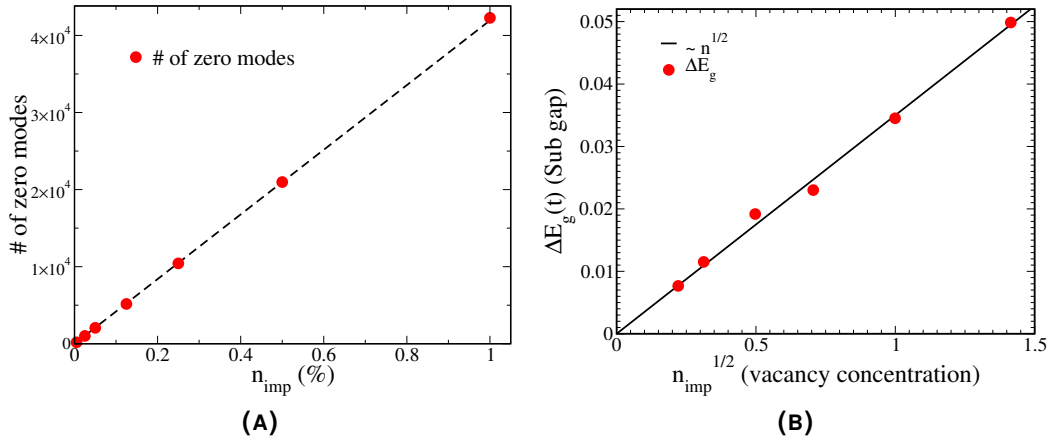


FIGURE 3.5: (A) Shows the evolution of zero modes with vacancy concentrations, $n_{\text{imp}} = n_A - n_B$. The number of zero modes, \mathcal{N} , is calculated numerically using Eq. (3.17). The dotted line shows the expected number of zero modes for different concentrations of vacancies. Numerical simulation is performed on a periodic lattice containing 2048^2 sites. (B) Shows the dependence of the sub-gap, ΔE_g , as a function of $n_{\text{imp}}^{1/2}$. The line describes a linear fit. The linear behavior clearly confirms the expected dependence of the sub-gap with vacancy concentrations, i.e. $\Delta E_g \propto n_{\text{imp}}^{1/2}$.

is: $\Delta E_g \propto n_{\text{imp}}^{1/2}$. This is because in the presence of vacancies, there exists a new energy scale in the problem along with the hopping amplitude, t , which is essentially given by the average distance between the vacancies, l ,

$$\varepsilon \sim \frac{v_F}{l}; \quad \text{with, } l \propto n_{\text{imp}}^{-1/2}. \quad (3.18)$$

where we assume $\hbar = 1$. Indeed, our numerical investigation confirms this assumption (see Fig. 3.5B).

Flow analysis of the eigenvalues: It has been proposed previously that due to flow of states close to E_F to the peak of the density of states (transfer of spectral weight from the low-energy region), introduces the sub-gap, $2\Delta E_g$, near $E = 0$ [138]. In order to understand this behavior of the low-energy states we perform a flow analysis of the eigenvalues in a finite size graphene sample for different vacancy concentrations. Our study, however, in the low concentration regime ($n_{\text{imp}}L^2 \lesssim 1$) for a finite size sample containing 4096 sites indicates that states near the Fermi energy move away from the Dirac point with increasing vacancy concentrations. In Fig. 3.6 we analyze the flow of the few lowest lying eigenvalues with increasing vacancy concentrations in two different situations. The right panel of Fig. 3.6 shows the flow of the eigenvalues when vacancies are placed symmetrically following a line in the lattice. The right panel of Fig. 3.6 shows the flow of few lowest lying eigenvalues in the presence of randomly placed vacancies in one sub-lattice. It emphasizes the observation that eigenvalues close to the Fermi

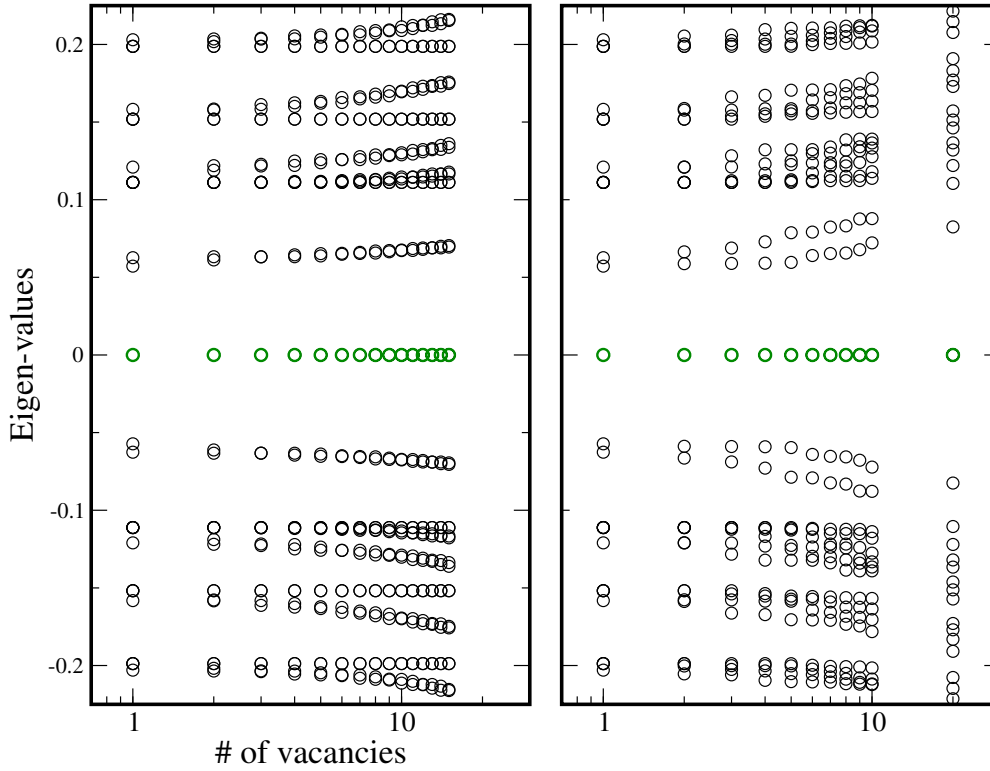


FIGURE 3.6: Flow of the eigenvalues near the Fermi energy with increasing vacancy concentrations. Left panel shows the flow of the eigenvalues when vacancies are placed along a line in one of the sub-lattices of a square graphene lattice containing 4096 sites with periodic boundary condition in both the direction. For comparison in the right panel we show another situation when vacancies are placed randomly in one sub-lattice. It shows that in the presence of vacancies in one sub-lattice the lowest lying eigenvalues are moved away from the Fermi energy creating a gap in the spectrum near the charge neutrality point. Moreover, due to randomness several degeneracies are lifted compared to the previous scenario, when vacancies were placed along a line.

energy move away from the zero energy with increasing number of vacancies. In this situation due to randomness the degeneracies in the eigenvalues are lifted compared to the situation when vacancies has been placed symmetrically along a line.

Vacancies in both the sub-lattices: When vacancies are distributed evenly in both the sub-lattices the above situation changes. Most remarkably, the gap, which was a prominent feature near the Fermi energy in the previous situation, disappears at different concentration of vacancies. Moreover, as the DoS approaches $E \rightarrow 0$, it shows a diverging behavior, which resembles the DoS in the chiral symmetry class, BDI. Further analysis is needed to confirm the expected behavior of the DoS. This is an ongoing work with V. Häfner [136].

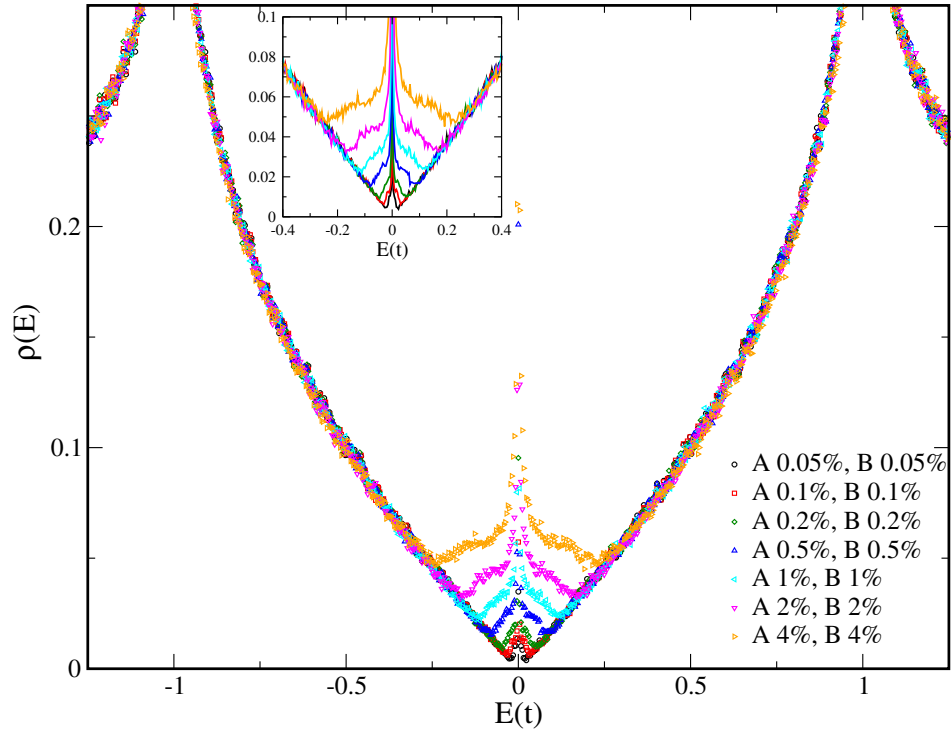


FIGURE 3.7: Density of states of graphene in the presence of different concentration of vacancies. The simulation is performed in a graphene lattice containing $\sim 4 \times 10^6$ atoms. Inset: Details of the region close to the Dirac point ($E = 0$) is shown.

3.2.4 Summary and Outlook

In this part of the thesis we have provided an analysis of the DoS of graphene in the presence of vacancy disorder. Our study shows that the DoS has quite different behavior depending on the distribution of vacancies in different sub-lattices. For vacancies in only one sub-lattice, we notice that a gap develops near the Fermi energy, which scales as, $\Delta E_g \propto n_{\text{imp}}^{1/2}$. However, when vacancies are equally distributed in both sub-lattices, the gap develops into a hump in the low-energy region indicating a quite different situation than what one expects from a single vacancy physics.

Several aspects of the DoS have been left untouched in the above study. For instance, the analysis of the DoS in the presence of vacancies in both the sub-lattices is still ongoing. Moreover, further analysis is needed to show how the peak width at the zero energy of the DoS (see Fig. 3.7) depends on the vacancy concentrations and system sizes. Another important aspect that needs to be addressed in the future study is the intermediate situation that appears when a finite concentration vacancies is distributed unequally in both the sub-lattices. Further investigations in this direction is required to understand the transition behavior of the DoS from the insulating to the metallic phase.

3.3 Transport properties of graphene with vacancies

The transport properties of graphene are interesting in its own right. For instance, it has been shown with analytical treatments that short and wide samples of ballistic graphene have a conductivity close to $\sim 4e^2/\pi h$. Nevertheless experimental investigations suggest the value of the conductivity to be π -times larger than what has been proposed for ballistic samples (see Fig. 1.4,1.5). As mentioned in the introduction, the enhancement in the conductivity is thought to be due to various possible types of disorder that occur in experiments (see Fig. 1.7). In this section we explore the effect of another possible type of disorder (resonant impurities) that preserves the chiral symmetry (C_z in terminology, see Appendix) of graphene, relevant to transport experiments.

A resonant scatterer is realized, for instance, by adding hydrogen atoms or different functional groups (CH_3 , OH , C_2H_5 etc.) as ad-atoms. Importantly, the resonant character of ad-atoms or hydrogen molecules change the hybridization of carbon atoms from sp^2 to sp^3 . A vacancy, on the other hand can have two different consequences, from a chemical point of view while preserving the particle-hole symmetry of the lattice. In a more realistic situation, the vacancy site can either go through a bond reconstruction or the disrupted bonds remain as dangling bonds removing only the π orbital on the site. As a first approximation in our study of vacancies we only consider the latter situation. Similarly, a strong on-site potential is also a natural example of resonant scatterer in graphene, which can be represented with a scalar potential in the Dirac equation, provided the energy of the localized state coincides with the Dirac point.

Even more interesting situation arises for a finite concentration of vacancies. In this situation a finite number of zero modes appears exactly at the Fermi energy; thus affecting the transport measurements at low frequencies. In this section we numerically investigate the effect of a finite concentration vacancies in the transport properties of short and wide graphene sample.

3.3.1 Theoretical model and method

Here we only present an outlook of the model and relevant quantities that have been used in numerical simulation to calculate the transport properties of a graphene sample (see Fig. 3.8). For a general discussion of the model please see Appendix C.

We consider a rectangular graphene sample of width W and length $L \ll W$. In Fig. 3.8 we show a typical experimental setup that has been considered here. Two metallic leads are attached at the long edges at $x = 0$ and $x = L$. With

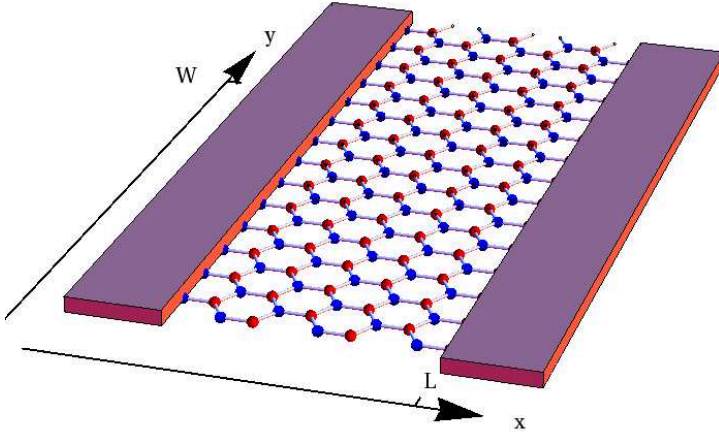


FIGURE 3.8: The ballistic setup used in transport calculation. Two metallic leads are attached along the width at $x = 0$ and $x = L$. Graphene is pinned at the Fermi energy. The current flows along the length of the sample, L .

the matrix Green function formalism (see Appendix C) one can represent the generating function, $\mathcal{F}(\phi)$, of the disordered sample in the following concise form,

$$\mathcal{F}(\phi) = -\frac{W\phi^2}{2\pi L} + \ln \det M(\phi) + \ln \det M(-\phi) + O(1) \quad (3.19)$$

where ϕ is the full counting field and $M(\phi)$ is a $N \times N$ matrix with elements,

$$M_{ij}(\phi) = \frac{\exp\left[\frac{\phi}{2L}(y_i - y_j)\right]}{\sin\left[\frac{\pi}{2L}(z_i x_i + z_j x_j + i y_i - i y_j)\right]} + z_i z_j \frac{\exp\left[\frac{\phi}{2L}(y_j - y_i)\right]}{\sin\left[\frac{\pi}{2L}(z_i x_i + z_j x_j + i y_j - i y_i)\right]} \quad (3.20)$$

where (x_i, y_i) is the coordinate of the i -th impurity. $z_i = \pm 1$ denotes vacancies in A (+1) or in B (-1) sub-lattices respectively. The conductance of a ballistic sample can be calculated by taking the second derivative of the generating function,

$$G = -\frac{4e^2}{h} \left. \frac{\partial^2 \mathcal{F}}{\partial \phi^2} \right|_{\phi=0} = \frac{4e^2 W}{\pi h L} + \frac{8e^2}{h} \text{tr} \left[(\dot{M} M^{-1})^2 - \ddot{M} M^{-1} \right]_{\phi=0} + O(1) \quad (3.21)$$

The main numerical task is to calculate the matrix inversion of the matrix $M(\phi = 0)$ for different configurations of impurities.

3.3.2 Result and discussion

In order to calculate the matrix inversion as described in Eq. (3.21), we use the standard software package provided by the LAPACK [142] routines. For small concentration of vacancies we consider several disorder realizations of the order $10^4 - 10^6$ with system sizes in the range of $W/L = \{8, 10, 12, 14, 16\}$. However, for large vacancy concentrations the direct inversion method breaks down due to a broad distribution of eigenvalues of the matrix, $M(\phi)$. To this end, we adopt a standard matrix-inverse update algorithm (see Ref. [137]) by adding vacancies one by one to compute the conductivity. In this section we present results obtained

from both methods in different regime of vacancy concentrations.

Self averaging: By investigating the distribution function in this section we explore the “self-averaging” property, which is a central concept in any disordered electron system, of the observable quantities in a disordered graphene sample. One can understand self-averaging by considering the following situation: in any transport measurement on a large, macroscopic sample there are several current carrying paths that sum up to the total current. In most of the general cases these paths contribute independently while exploring different parts of the sample. Thus sample to sample fluctuations for such averaging quantities become smaller as the sample size gets bigger. An observable quantity is called self-averaging when this fluctuations becomes much smaller than the average value itself and vanishes in the limit $L \rightarrow \infty$.

The concept of self-averaging is a corner-stone in the theory of disordered electron systems; for instance, self-averaging guarantees restoration of symmetries, such as translation and rotational symmetry, which, to begin with, is broken in the presence of disorder. Specifically, after disorder averaging over an ensemble has been carried out, the resulting equations shares many more symmetry properties with a clean electron system. Consequently, it helps to develop analytical tools to find a quantitative descriptions of the experimental observations by studying only few disorder configurations in a finite size sample, although the exact disorder configuration in experiments are not known. More precisely, the average contribution of various part of the sample, ξ , of sample size, $L \gg \xi$ is no different from the average over different sample of size, ξ , which is also the situation in our construction of the experimental setup (see Fig. 3.8). Below we will show how this particular property is also observed in the situation that we consider here, namely graphene with vacancy disorder.

Distribution function: In Fig. 3.9 (main panel) we plot the flow of the distribution function, $\mathcal{P}(\delta G)$, of the correction to the conductance, δG , with different system sizes of vacancy concentrations, $n_{imp}L^2 = 1$, where $n_{imp} = N/LW$ is the concentration of vacancies with N being the total number of vacancies in a sample. In the following discussion we consider vacancies that are distributed in one sublattice only. First note that the correction to the conductance is positive, which indicates an increase in the clean conductance value in the presence of vacancies. The evolution of the distribution function towards higher value of conductance, δG , with increasing system sizes illustrates the usual behavior as expected from a mesoscopic wide and short sample. As with increasing width of the sample, the number of current carrying path increases; thus also the conductance, which is proportional to the current. Additionally, as the sample gets wider, the width of the distribution function, $\mathcal{P}(\delta G)$, gets broader while at the same time the amplitude of the height decreases. This observation is better illustrated in the inset of Fig. 3.9,

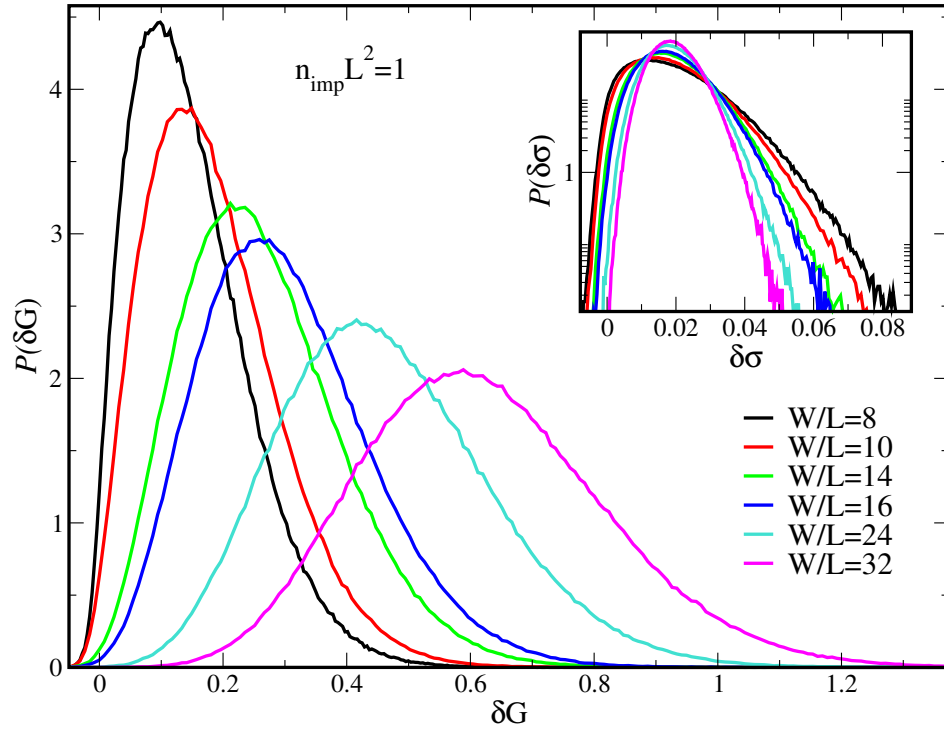


FIGURE 3.9: Flow of the distribution function, $\mathcal{P}(\delta G)$, with different system sizes. Main panel shows the $\mathcal{P}(\delta G)$ for system sizes ranging from, $W/L = \{8, 10, \dots, 32\}$, of vacancy concentration, $n_{\text{imp}} L^2 = 1$. Inset: Shows the distribution function, $\mathcal{P}(\delta\sigma)$, in a log scale indicating the asymmetric distribution function and self-averaging property of the conductivity.

where we plot the distribution function of conductivity, $\sigma = GL/W$, in a log-linear scale. It is readily seen from the inset of the figure that the variance and the average value of the conductivity have two different scaling behavior with system size. Another important feature that comes out from the inset of the Fig. 3.9 is the asymmetry in the distribution function in low vacancy concentration, $n_{\text{imp}} L^2 \lesssim 1$, with respect to the mean value of the conductivity.

The situation changes with higher concentration of vacancies, as seen in the inset of Fig. 3.10. Here, the distribution function becomes symmetric with increasing system size for a fixed vacancy concentration, $n_{\text{imp}} L^2 = 8$ with respect to its mean value. Moreover, the self-averaging property is also evident as the distribution function is getting narrower with increasing system size (see inset of Fig. 3.10). In order to have a quantitative measure of the self-averaging property, we approximate the distribution function, $\mathcal{P}(\delta\sigma)$, with a Gaussian distribution of variance, $\delta\bar{\sigma}^2$ and mean, $\delta\sigma_0$;

$$\mathcal{P}(\delta\sigma) \approx \frac{1}{\sqrt{2\pi\delta\bar{\sigma}^2}} \exp\left(-\frac{(\delta\sigma - \delta\sigma_0)^2}{2\delta\bar{\sigma}^2}\right) \quad (3.22)$$

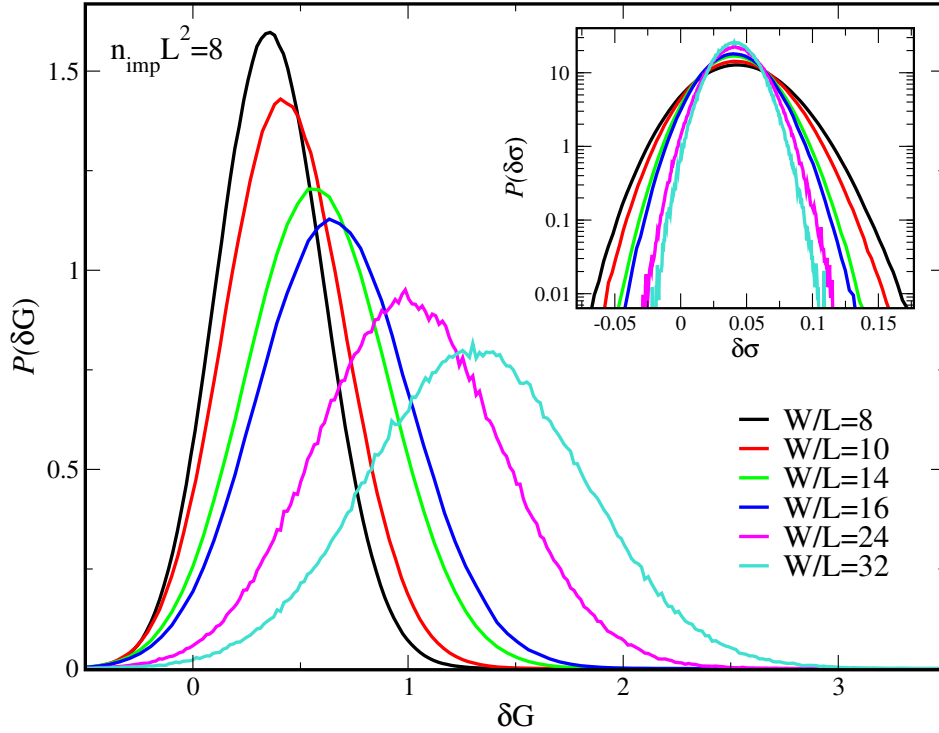


FIGURE 3.10: Flow of the distribution function, $\mathcal{P}(\delta G)$, with different system sizes. Main panel shows the $\mathcal{P}(\delta G)$ for system sizes ranging from, $W/L = \{8, 10, \dots, 32\}$, of vacancy concentration, $n_{\text{imp}}L^2 = 8$. Inset: Shows the distribution function, $\mathcal{P}(\delta\sigma)$, in a log scale indicating the symmetric behavior of distribution function.

The two fitting parameters, $\delta\bar{\sigma}^2, \delta\sigma_0$ is plotted in Fig. 3.11A for different system sizes and two different vacancy concentrations. The main panel shows the dependence of the $\sqrt{\delta\bar{\sigma}^2}$ with $1/(W/L)^{1/2}$. It clearly suggests, that the variance, which scales as $\delta\bar{\sigma} \propto 1/(W/L)^{1/2}$, vanishes in the infinite system size limit; consequently, the distribution becomes a delta function at this limit. Thus the fluctuation in the average value of the conductivity vanishes indicating the self-averaging of the conductivity. Inset of the Fig. 3.11A shows the scaling of the mean value, $\delta\sigma_0$ with system size, $1/(W/L)$. Unlike the variance the mean value scales as $\delta\sigma_0 = \delta\sigma_0^* + O(1/(W/L))$, again emphasizing the ‘self-averaging’ property of the conductivity similar to usual disordered metals, where $\delta\sigma_0^*$ is the mean value of the conductivity in the limit of infinite system size, $L \rightarrow \infty$.

Conductivity: In Fig. 3.12A we show the dependence of the correction to the conductivity ($\delta\sigma = \delta GL/W$) of graphene with vacancy concentrations in the limit $W \gg L$ for different values of δ , which measures the imbalance of vacancy distribution between two sub-lattices. The data in Fig. 3.12A is shown for two different values of system size, W/L . At higher concentration of vacancies there is a significant finite size corrections. In order to eliminate these corrections in Fig. 3.12B

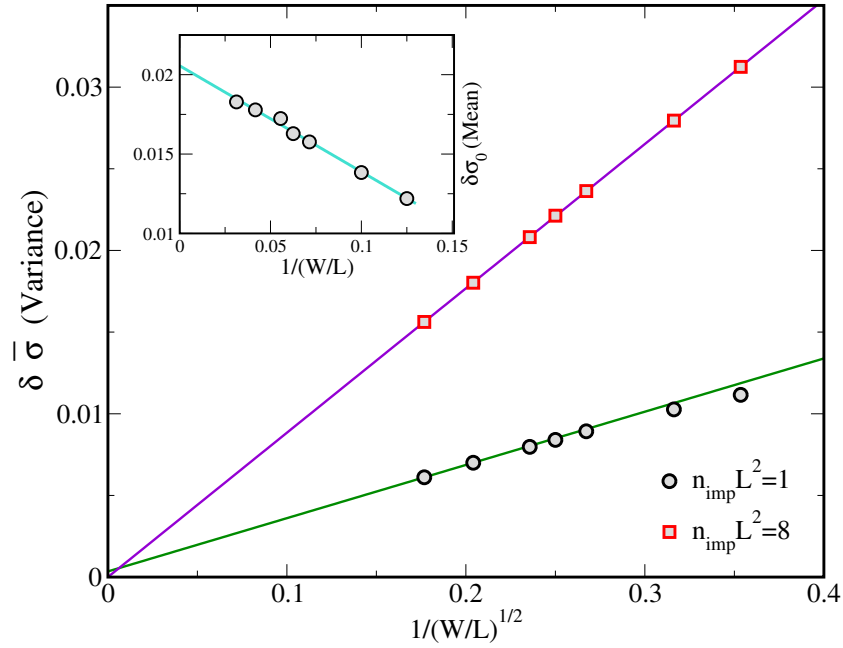


FIGURE 3.11: Main panel: Shows the scaling behavior of variance with system sizes for two different concentration of vacancies, $n_{\text{imp}}L^2 = 1, 8$. It indicates that as the system size reaches infinity, $L \rightarrow \infty$, the variance of the conductivity vanishes. Thus the self-averaging property of the conductivity is established. Inset: Shows the scaling of the mean value with $1/(W/L)$ for a vacancy concentration, $n_{\text{imp}}L^2 = 1$.

we replot the data by taking the limit $W/L \rightarrow \infty$ for every concentrations of vacancies.

In the large concentration limit, $n_{\text{imp}}L^2 \gg 1$, the conductivity, $\sigma = GL/W$ acquires constant values depending on the distribution of vacancies between sublattices that can be seen in Fig. 3.12A. This is because with increasing vacancy concentrations the interatomic distance between vacancies becomes small and they start to overlap and lose the resonant character. For even larger concentration of vacancies, $n_{\text{imp}}L^2 \rightarrow \infty$, the system will eventually go through localization (percolation limit).

This can be put on a firmer basis by recalling that graphene with randomly distributed vacancies falls into the symmetry class BDI. The corresponding σ -model for this symmetry class is characterized by a vanishing β -function that has a line of fixed points with a non-universal value of conductivity in the infrared limit [46]. Our numerical investigation suggests two possible fixed points: a) for a strictly equal distribution of vacancies in both the sub-lattices, $n_A = n_B$, the conductivity saturates at $\sigma^* \simeq 1.6 \times 4e^2/\pi h$ and b) when vacancies are distributed only in one sub-lattice the correction to the conductivity in large concentration limit becomes negligible, implying a value close to the clean fixed point, $4e^2/\pi h$. Importantly, in this situation, $n_A \neq n_B$, the conductivity becomes a non-monotonic function of

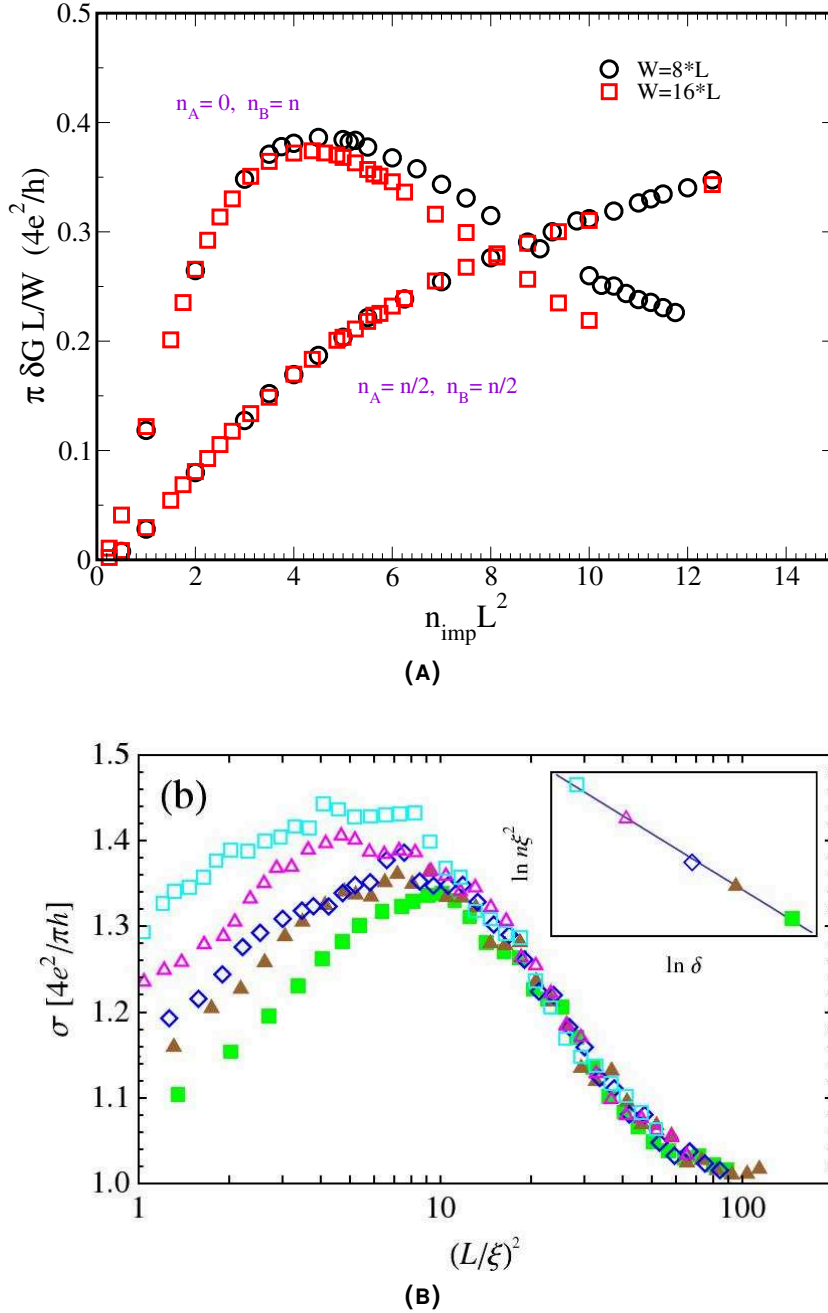


FIGURE 3.12: (A) Dependence of mean conductivity for different concentrations of vacancy $n_{\text{imp}}L^2$ for two different values of $\delta = (n_A - n_B)/n$, i.e. $\delta = 0, 1$ and for two different system sizes. δ measures the vacancy distribution between two sub-lattices. As it is seen with increasing vacancy concentrations conductivity increases up to a maximum value before it decreases. The situation changes when vacancy is distributed equally in both the sub-lattices. In this situation conductivity saturates at some finite value. (B) Shows the conductivity as a function of $(L/\xi)^2$ for different distribution of vacancies between the sub-lattices, δ . At higher concentration of vacancies conductivity becomes a universal function of L/ξ , where ξ is the correlation length of the crossover from the ballistic to the diffusive regime. Inset shows the correlation length, $\ln n \xi^2$ as a function of $\ln \delta$. It illustrates the power law scaling of the length $\xi \sim n^{-1/2} \delta^{-0.36}$. Figure (B) courtesy P. Ostrovsky.

the vacancy concentration, implying a crossover from the ballistic to the diffusive regime.

In order to investigate these two fixed points separately, we perform the scaling analysis in a small parameter, $\delta = (n_A - n_B)/(n_A + n_B)$ (see Fig. 3.12)B. The data plotted there have been extrapolated in the limit $W/L \rightarrow \infty$ for different vacancy concentrations ($n_{\text{imp}}L^2$). The conductivity in the large concentration limit shows a universal scaling with L/ξ , where ξ is the correlation length, $\xi \sim n_{\text{imp}}^{-1/2}\delta^{-0.36}$. This type of non-trivial scaling behavior in the chiral system in the strong coupling limit is not captured within the σ -model framework. This special kind of fixed point need to be investigated further. However, in the small concentration regime the data deviates from the scaling in the small parameter, indicating a possibility of two-parameter scaling in such systems.

3.3.3 Summary and Outlook

In this chapter we present our numerical analysis of the conductivity using a general theory, which was provided by P. Ostrovsky (see Appendix C). First we discuss the ‘self-averaging’ property of the conductivity in such a system. It is important to mention that the presence of the self-averaging property in our model is intrinsic by construction of the small and wide sample. Next we show that the conductivity in such a system is not only depends on the impurity concentration but also on the distribution of impurities in different sub-lattices. Our numerical investigation confirms that the conductivity saturates at a constant value for high concentration of impurities; additionally, it also describes a crossover from the ballistic to the diffusive regime, which suggest a non-trivial phase diagram in two-dimensional chiral class, BDI.

However, further studies are required in order to fully understand this non-trivial phase in this system, which is beyond the standard sigma model analysis [137]. Another important aspect that has been left out in this analysis is the effect of electron-electron interaction on the resonant character of the impurities. A detailed *ab-initio* study will be useful to fully appreciate the experimental findings and to understand the resonant character of zero modes in experiments. Moreover, the effects of edges are partially ignored in this work. For instance, it has been shown that the zigzag edge terminated graphene nano-ribbons has two flat bands (localized at two opposite edges) at the Fermi energy. Thus in the presence of vacancies the interplay between vacancy induced zero modes and edge states is a relevant direction to pursue in future works. Similarly, a more systematic analysis is required for the distribution function, when vacancies are distributed in both the sub-lattices. This is an ongoing work with V. Häfner.

4

CHAPTER 4

Integer Quantum Hall Transition: Interaction Effect

In the last chapter we noticed that the effect of more than one vacancies on the physical observables can not be understood by considering a single defect in a graphene lattice. It is because in the presence of a large concentration of vacancies the zero-modes associated with each of the vacancies start to hybridize; thus forming a narrow impurity band near the Fermi energy. In this limit wavefunctions are neither localized nor metallic, rather fluctuating strongly in space. This is known as the *multifractality* of wavefunctions [66]. Multifractality is a very generic feature of wavefunctions of strongly disordered metals at a critical point. For instance, in a two dimensional electron gas this feature appears in the presence of a magnetic field where the wavefunctions not only fluctuate strongly but also become critical. It implies that the average moments of the wavefunctions, $\langle |\psi(\mathbf{r})|^{2q} \rangle$, show a power law behavior, $L^d \langle |\psi(\mathbf{r})|^{2q} \rangle \sim L^{-\tau_q}$, where each moment scales with its own exponent τ_q . Multifractality in general is a rich concept; it turns out that in some situations characterization of new critical points by its multifractal spectrum has turned out to be very useful – a fact that has been discussed in detail in first chapter.

Although many aspects of the integer quantum Hall transition has been understood in a non-interacting single particle framework, understanding the effect of electron-electron interaction at the integer quantum Hall transition (IQH) still poses a considerable amount of challenge. Interaction effects manifest itself in low energy transport experiments by two distinct features a) renormalization and b) dephasing. In this section we will confine ourself mainly to dephasing effects, which is governed by inelastic processes of electron-electron scattering at finite temperature, T . It has been understood fairly well that in metallic systems dephasing provides a natural cutoff (i.e. an additional scale, T) for weak-localization effects [53]. As for quantum Hall type transitions, dephasing leads to smearing

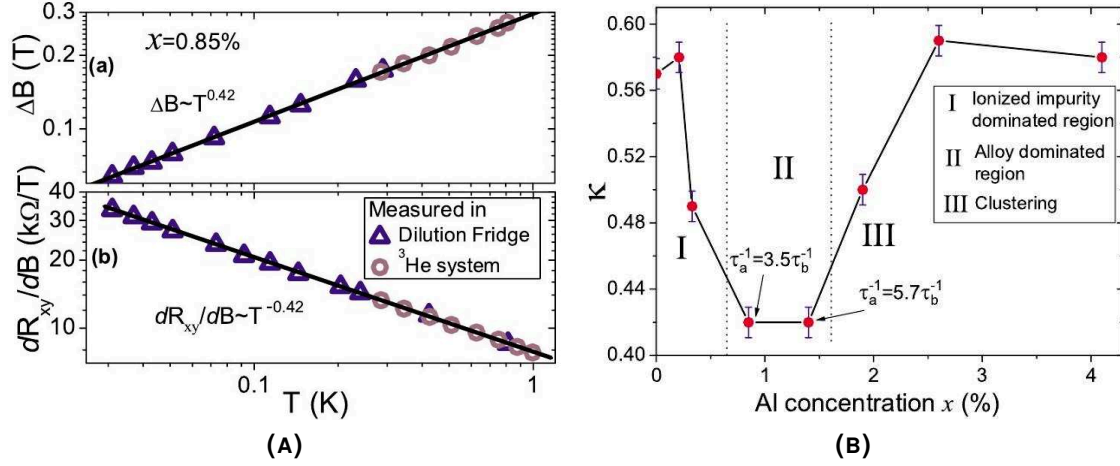


FIGURE 4.1: (A) Shows the scaling behavior of the plateau width (ΔB) and the critical region (slope of the transition, dR_{xy}/dB) as a function of temperature, T , down to 30mK. The experiment is performed in a $\text{Al}_x\text{Ga}_{1-x}\text{As}-\text{Al}_{0.33}\text{Ga}_{0.67}\text{As}$ heterostructure with Al concentration $x = 85\%$ for the 4-3 transition. Both of the curves show a power-law behavior in T indicating the critical exponent to be, $\kappa = 0.42$. (B) Dependence of exponent κ of different Al concentrations. It indicates that for different concentrations the variation in the exponent κ can be as large as 30%. In the second region, where scattering is dominated by alloy disorder, the critical regime of the IQH transition is reached and κ becomes universal, showing a value close to 0.42. Both the figures are adapted from Ref. [75].

at finite temperature, T . In this work we investigate such effects by combining an analytical treatment (lowest order perturbation theory in the interaction) and a numerical simulation at the IQH critical point. This part of the work is in collaboration with I. S. Burmistrov *et. al* [143], where he provides the analytical model and its solution as discussed in Appendix D. Our numerical simulation supports his analytical predictions. The discussion in this chapter largely follows from Ref. [143], which is our joint work that has been published recently.

The chapter is organized as follows. In the first section we will present some of the experimental results related to dephasing at the IQH transition. In the next section we will present the model and method that we use to tackle the problem. At the end along with the results we will provide some outlook based on our work.

4.1 Experimental results

At the IQH transition several experiments have been performed in the last few years which yield very different results for the scaling of the plateau transition with temperature, T . For instance, an experiment looking at the transport coefficients (ρ_{xx} , ρ_{xy}) of two-dimensional electron gas in a InGaAs/InP heterostructure shows

that the width of the plateau scales with the temperature as a power law, $\Delta B \propto T^\kappa$, with $\kappa = 0.42 \pm 0.04$ [76]. Some other experimental works suggest a value of κ slightly higher, $\kappa = 0.56 \pm 0.02$ [77, 78], which is thought to be because of macroscopic inhomogeneities in the sample due to which the true IQH scaling regime is difficult to reach [144, 145]. A more recent study along this line by Li et. al. [75] shows that for short range disorder when the true IQH critical regime is reached, $\kappa = 0.42 \pm 0.01$, and again the large deviation of κ ($\approx 0.58 \pm 0.02$) is assigned to impurity clustering in the sample (see Fig. 4.1).

The situation is better represented in Fig. 4.1B, where the dependency of the critical exponent, κ , is plotted over the concentration of Al. It clearly shows that for different impurity concentrations the value of κ differs mainly due to different nature of the impurity potential. In conventional quantum phase transition the universal scaling regime is defined by a large phase coherence length, which is usually identified as the inelastic scattering length (l_{in}), compare to the disorder correlation length, $\xi \ll l_{\text{in}}$. In regions I and III of Fig. 4.1B, due to the presence of ionized impurities (i.e. a slowly varying disorder potential) and the clustering of Al atoms respectively, the correlation between impurities becomes large compare to l_{in} ($\gtrsim \xi$); thus true scaling behavior is not observed. Whereas in the region II the disorder is dominated by short range impurities; consequently, the universality is restored in the plateau-to-plateau transition and the exponent is found to be $\kappa = 0.42$. Even more recent work in by the same group in $\text{Al}_x\text{Ga}_{1-x}\text{As}-\text{Al}_{0.33}\text{Ga}_{0.67}\text{As}$ heterostructure samples down to very low temperature (1 mK) confirms the previous result for the exponent $\kappa \simeq 0.42 \pm 0.01$ in a large temperature range [146, 147].

In this chapter motivated from the aforementioned experimental investigations we perform a numerical study of the scaling properties of the dephasing rate at the IQH critical point based on the Chalker-Coddington network model (CCNM). The CCNM serves as a model of the integer quantum Hall transition, which we discuss in detail later in the chapter.

4.2 Analytical considerations

In Appendix D we provide a detailed description of the model and the calculation for the dephasing rate, τ_ϕ . Here we only summarize few important results, which will be relevant for numerical simulation of the exponent κ .

First-order correction: Here we study the correction due to interaction to the thermodynamic potential, Ω , by doing a perturbation theory in the interaction near the non-interacting fixed point. The first-order interaction correction to the

thermodynamic potential, Eq. (D.4), includes the following correlation function,

$$\mathcal{K}_1(\mathbf{r}_1, \mathbf{r}_2, E, \omega) = \frac{\Delta^2}{2} \sum_{\alpha, \beta} \langle |\mathcal{M}_{\alpha, \beta}(\mathbf{r}_1, \mathbf{r}_2)|^2 \delta(E + \omega - \epsilon_\alpha) \delta(E - \epsilon_\beta) \rangle \quad (4.1)$$

where $\Delta=1/(\varrho_d L^d)$ is the mean level spacing with ϱ_d being the density of states and d is the dimension of the system in consideration. $\mathcal{M}_{\alpha, \beta}(\mathbf{r}_1, \mathbf{r}_2)$ is the matrix elements of the non-interacting single particle wavefunctions, $\phi_\alpha(\mathbf{r})$, with eigen energy ϵ_α as defined in Eq. (D.5). The correlation function has the following scaling relation,

$$\mathcal{K}_1(\mathbf{r}_1, \mathbf{r}_2, E, \omega) = L^{-2d} \left(\frac{|\mathbf{r}_1 - \mathbf{r}_2|}{L_\omega} \right)^{\mu_2} \tilde{\mathcal{K}}_1 \left(\frac{|\mathbf{r}_1 - \mathbf{r}_2|}{L_\omega} \right), \quad (4.2)$$

where,

$$\tilde{\mathcal{K}}_1(x) = \begin{cases} 1, & x \ll 1 \\ x^{-\mu_2}, & x \gg 1, \end{cases} \quad (4.3)$$

with $L_\omega = L(\Delta/|\omega|)^{1/d}$ being the length scale due to the frequency and μ_2 is the scaling exponent. Note that due to the anti-symmetrized wavefunction (Hartree-Fock), Eq. (D.5), the exponent μ_2 corresponding to the scaling function \mathcal{K}_1 is positive $\mu_2 > 0$. At criticality it reflects that at shorter distances, $|\mathbf{r}_1 - \mathbf{r}_2| \ll L_\omega$, the correlation function is suppressed compared to the metallic system. Using CCNM we calculate the exponent μ_2 at the IQH critical point.

Second order correction: We consider the second order correction in the interaction, U , to calculate the dephasing rate, τ_ϕ , which is determined by the imaginary part of the self-energy (see Fig. D.2). Details of the calculation is given in Appendix D. The imaginary part of the self-energy, $\Sigma_\alpha^R(\varepsilon)$, contains the following 8 wavefunctions correlation function,

$$\begin{aligned} \mathcal{K}_2(\{\mathbf{r}_j\}, E, \epsilon, \varepsilon', \Omega) &= \frac{\Delta^4}{8} \left\langle \sum_{\alpha\beta\gamma\delta} \mathcal{M}_{\alpha\beta}^*(\mathbf{r}_1, \mathbf{r}_2) \mathcal{M}_{\delta\gamma}(\mathbf{r}_1, \mathbf{r}_2) \mathcal{M}_{\gamma\delta}^*(\mathbf{r}_3, \mathbf{r}_4) \mathcal{M}_{\beta\alpha}(\mathbf{r}_3, \mathbf{r}_4) \right. \\ &\quad \times \delta(E - \epsilon_\alpha) \delta(\varepsilon' + \Omega - \epsilon_\beta) \delta(\varepsilon' - \epsilon_\gamma) \delta(\epsilon + \Omega - \epsilon_\delta) \rangle, \end{aligned} \quad (4.4)$$

where $\langle \rangle$ denotes disorder averaging and $\mathcal{M}_{\alpha, \beta}(\mathbf{r}_1, \mathbf{r}_2)$ is defined in Eq. (D.5). The above correlation function has the following scaling behavior,

$$\mathcal{K}_2(\{\mathbf{r}_j\}, 0, 0, \varepsilon' \sim T, \Omega) = L^{-4d} \left(\frac{|\mathbf{r}_1 - \mathbf{r}_2| |\mathbf{r}_3 - \mathbf{r}_4|}{R} \right)^{\mu_2} \left(\frac{R}{L_\Omega} \right)^\alpha, \quad (4.5)$$

where $R = (\mathbf{r}_1 + \mathbf{r}_2 - \mathbf{r}_3 - \mathbf{r}_4)/2$. The above scaling form of the correlation function, \mathcal{K}_2 , is valid in the range $|\mathbf{r}_1 - \mathbf{r}_2|, |\mathbf{r}_3 - \mathbf{r}_4| \ll R \ll L_\Omega$ with the assumption that $\varepsilon' \sim \Omega$, as both the energies are of the order of the temperature, T . L_Ω is a length scale

defined by the energy Ω . In the limit of large distance, $R \sim L_\Omega$, the correlation between wavefunctions at the points $\mathbf{r}_{1,2}$ and at the points $\mathbf{r}_{3,4}$ decouples. In this limit the correlation function \mathcal{K}_2 reduces to a product of two independent scaling functions given by the correlation function \mathcal{K}_1 , i.e. $(|\mathbf{r}_1 - \mathbf{r}_2|/R)^{\mu_2}(|\mathbf{r}_3 - \mathbf{r}_4|/R)^{\mu_2}$. One of the main numerical task in this work is to calculate the exponent, α , which describes the scaling with respect to the variable R/L_Ω .

4.2.1 Dephasing length and short range interaction

We will summarize the above results for dephasing rate and will derive an expression for κ in terms of the exponent μ_2 as defined earlier. We will consider a situation of the “most” short-range interaction (see Appendix D), i.e. $\lambda > d + \mu_2$ with $d = 2$ to derive the relevant exponents. In this situation the dephasing rate is given by, $1/\tau_\phi \propto T^p$ with $p = 1 + 2\mu_2/d$ (see Eq. (D.20)). The scaling of the dephasing length, L_ϕ , is given by,

$$L_\phi \propto T^{-1/z_T}; \quad z_T = \frac{d}{p} = \frac{d}{1 + 2\mu_2/d}. \quad (4.6)$$

The exponent, z_T is the dynamical exponent governing the scaling of the dephasing length, L_ϕ , and have the dimension of energy. It is important to note here that localization problem in general possesses rich physics and characterized by several dynamical exponents. Another important exponent z that controls the scaling with frequency ($L_\omega \sim \omega^{-1/z}$) has a trivial non-interacting value $z=d=2$ for the short range interaction.

The transition width induced by inelastic scattering at finite temperature scales as, T^κ , where κ is given by comparing Eq. (4.6) with localization length exponent, $\xi_{\text{loc}} \propto |E - E_c|^{-\nu}$, where E is the parameter that controls the transition. It yields,

$$\kappa = \frac{1}{z_T \nu} = \frac{1 + 2\mu_2/d}{\nu d}. \quad (4.7)$$

Therefore, by evaluating μ_2 numerically we will be able to compare the existing values of κ with our estimates.

4.3 The network model at the IQH critical point

Aiming to address these challenging questions we have implemented the Chalker-Coddington network model (CCNM) [71], which serves as a paradigm of numerical simulation at the IQH critical point. In this section, we first introduce the model, our implementation approach, and finally the pursued parallelization strategies in

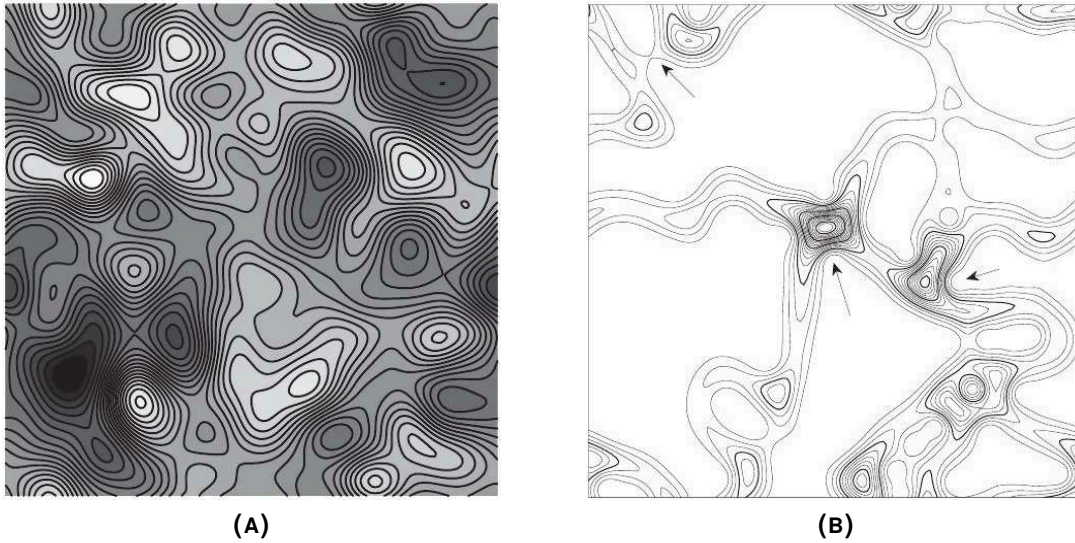


FIGURE 4.2: (A) Shows the equipotential lines of the random potential of correlation length, $\xi_c=2\ell_B$. White regions denotes high potential (maxima) and black denotes low potential (minima). (B) Shows the modulus of a wavefunction corresponding to an energy near the center of the Landau level following essentially the equipotential lines. The arrows denote the tunneling near the saddle points. Figures are adapted from Ref. [148].

the Appendix, which become vital within a reasonable amount of time to obtain the proper scaling behavior of the correlation functions, $\mathcal{K}_{1,2}$.

4.3.1 Percolation picture

One of most fascinating aspect of quantum Hall physics, along with the high magnetic field, is the presence of a random disorder induced by the presence of impurities in the bulk of the sample; such as a GaAs/AlGaAs heterostructure. In most of the experimental situations the nature of a sample is such that the inversion layer is far from the doping layer; consequently, the electrons experience a potential landscape that is rather smooth on the length scale of the magnetic field $\xi_c \gg \ell_B$, where ξ_c is the disorder correlation length and $\ell_B = \sqrt{(\hbar/eB)}$ is the magnetic length. It is particularly important because in this limit the problem of a two-dimensional electron gas in a *high* magnetic field with spatially correlated disorder can be solved (eigenstates and eigen-energies) by solving a semi-classical percolation problem [148]. However, for a complete solution of the problem one needs to include the quantum interference and the tunneling effects in the corresponding model – the percolation model serves only as a physical background of the CCNM.

In sufficiently large field limit, when mixing between different Landau levels is avoided, the dynamics of the electrons are governed by two different length scales

(separation of length scales) in the system. In this limit the eigen energies can be evaluated by solving the Schrödinger equation,

$$E_n = \left(n + \frac{1}{2} \right) \hbar\omega + V_{\text{equi}}(X, Y) \quad (4.8)$$

where $V_{\text{equi}}(X, Y)$ is the potential induced by the impurities and is centered around the point (X, Y) . Fig. 4.2A illustrates such a potential landscape. The general form of the wavefunction can be formally derived using the Schrödinger equation in the limit $\xi_c \gg \ell_B$ [149],

$$\Psi(u, v) = C(u)\mathcal{F}_n(v)e^{i\phi(u,v)}, \quad (4.9)$$

where u and v parameterize the distance along and perpendicular to the equipotential lines respectively. The index n denotes the Landau levels and \mathcal{F}_n is the n th harmonic oscillator wavefunction. The function, $C^{-2}(u)$, is given by the gradient of the potential (V_{equi}) at the point $v = 0$ and $\phi(u, v)$ is a gauge-dependent phase, which changes sign by integer multiple of 2π ; thus giving a condition on the allowed energy values, Eq. (4.8). The wavefunction amplitude is only nonzero along the equipotential lines (see Fig. 4.2B). Moreover, when two equipotential lines come close to each other (saddle point of the potential), the amplitude of the wavefunction becomes higher than at other places on the potential line, which indicates quantum tunneling (indicated by arrows in Fig. 4.2B). Additionally, the average spatial extent of the wavefunctions is given by the mean diameter of the percolating lines. Below we list few important results that come out from the percolation model:

- The wavefunctions that have energies far away from the band center, i.e. at the tail of the bands, follow closed percolating trajectories.
- Upon increasing the energy, the mean diameter of the percolating lines increases; thus at some energy, E_c , it reaches the percolating threshold. At this energy the wavefunctions are critical at the band center for a symmetric potential and the localization length, $\xi_{\text{loc}}(E)$, (or the mean diameter of the percolating trajectories) becomes of the order of system size.
- In the classical percolating theory the mean diameter near the threshold point diverges, $\xi_{\text{loc}}(E) \sim |E - E_c|^{-\nu_p}$, with an universal exponent, $\nu_p=4/3$ [150].
- Including the tunneling near the saddle points of the equipotential lines, it has been proposed that the exponent is increased exactly by one; $\nu=1+4/3 = 7/3$ [151].

The results discussed in this section will now allow us to construct the network model for describing the IQH critical point by including two main physical ingredients -quantum interference and tunneling effects- near the band center.

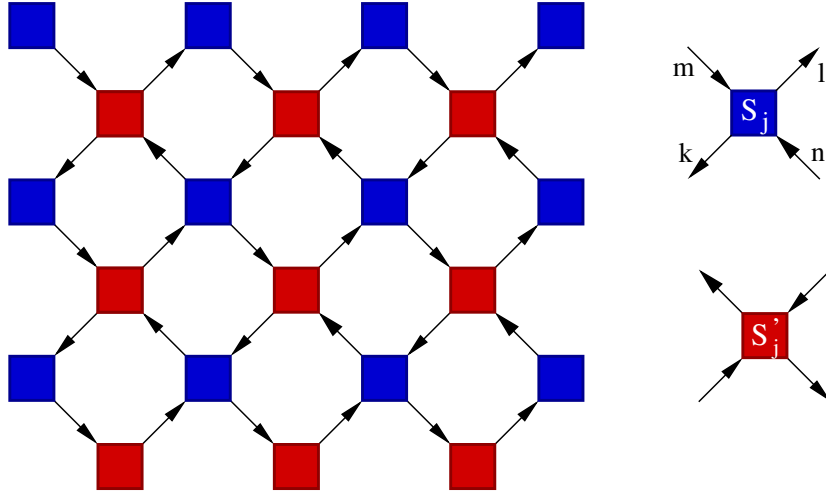


FIGURE 4.3: Schematic diagram of the Chalker-Coddington network model that we use in our numerical simulation. Each saddle point is represented by a scattering matrix S_j (blue) with two incoming (k,l) and two outgoing links (m,n) with corresponding scattering coefficients. The directed links describe the direction of the propagation of wavefunction amplitude. The scattering described by S' (red) differs from that of S by rotation of $\pi/2$ of the incoming and outgoing channel. We employ periodic boundary conditions in both directions of the lattice.

4.3.2 Network model

The network model is constructed from the classical percolation model by replacing the irregular assembly of the saddle points with a regular network of scattering centers connected via links along which the probability amplitude propagates. The general idea behind the model is that every crossing in the lattice is a scattering node where electrons, coming from a specific direction, can only move to its left or right with certain probabilities.

The probability is the same at every node in this model and is $1/2$ at criticality. A scattering matrix (\mathbf{S}_j) describes each of the node of the lattice where the unidirectional incoming (k,l) and outgoing (m,n) links represent the wavefunction amplitude ($\psi_{m,n,k,l}$). By solving a scattering problem with the potential, $V(x,y) = E_0 - ax^2 + by^2$, exactly, one finds the transmission probability as $|t|^2 = 1 - |r|^2 = 1/[1 + \exp(\pi\varepsilon)]$, where $\varepsilon = (E - E_0)/\ell_B^2(ab)^{1/2}$ [152]. The scattering matrix in terms of the transmission and reflection amplitude is defined as,

$$\begin{pmatrix} \psi_m \\ \psi_n \end{pmatrix} = \mathbf{S}_j \begin{pmatrix} \psi_k \\ \psi_l \end{pmatrix}; \quad (4.10)$$

with

$$\mathbf{S}_j = \begin{pmatrix} e^{-i\phi_m} & 0 \\ 0 & e^{i\phi_n} \end{pmatrix} \begin{pmatrix} -r & t \\ t & r \end{pmatrix} \begin{pmatrix} e^{i\phi_k} & 0 \\ 0 & e^{-i\phi_l} \end{pmatrix}. \quad (4.11)$$

The phases $\phi_{m,n,k,l}$ are random and correspond to the waves in the corresponding links. $R_j = |r|^2$ and $T_j = 1 - R_j = |t|^2$ defines the reflection and transmission amplitudes at the link j respectively. The wavefunction (Ψ) on the network consists of complex amplitudes ($\psi_{m,n,k,l,\dots}$) that were previously defined on each link of the lattice. The time evolution of such a state is given by,

$$|\Psi(t+1)\rangle = U_E |\Psi(t)\rangle, \quad (4.12)$$

where U_E is the energy dependent unitary “network” operator. The stationary solution of such a state is,

$$|\Psi(t)\rangle = e^{-i\phi} |\Psi(t+1)\rangle, \quad (4.13)$$

where ϕ is the phase angle. Combining Eq. (4.12) and (4.13) we get the eigenvalue equation as [153],

$$U_E |\Psi\rangle = e^{i\phi} |\Psi\rangle. \quad (4.14)$$

The solution of the eigenvalue problem, the quasi-energies (ϕ) and eigenvectors (Ψ), constitute the basic quantities that enter the calculation of almost any physical observable. It has been shown by calculating the transmission through the network the localization length exponent has been determined and found to be $\nu = 2.5 \pm 0.5$ [71]. However, a recent finite size scaling analysis shows that the CCNM suffers from large finite size corrections and the exponent is found to be $\nu = 2.593[2.587, 2.598]$ [72], which is significantly larger than earlier analytical estimates, $\nu = 2.33$ [151] but close to previous numerical calculation with the same model.

4.3.3 Method

We numerically simulate the aforementioned CCNM in order to calculate the corresponding scaling functions and exponents mentioned earlier. The details of implementation in our new computer code are given in Appendix E. Specifically, the existing code has been completely rewritten by us in order to facilitate parallelization. The work was done in close collaboration with I. Kondov from the SCC, who further optimized our code and in particular employed test-suite for benchmarking it. The improvement in computational speed that we could achieve in this way is roughly 2 orders of magnitude. The discussion in the Appendix is largely based on our joint preprint that has been presented in the KIT SimLab workshop [154].

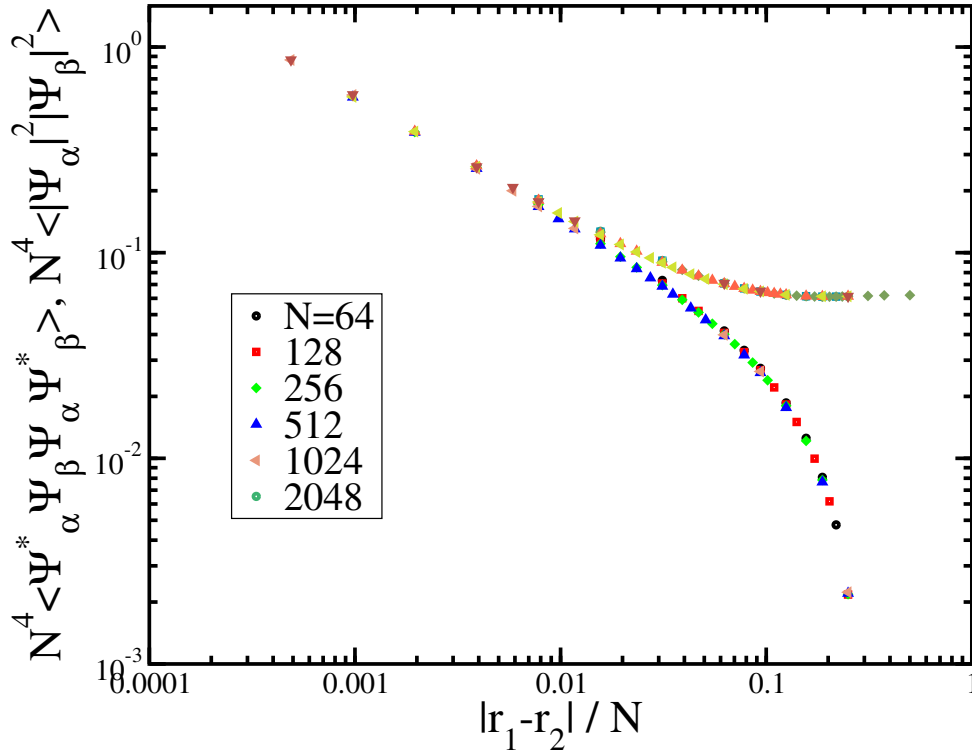


FIGURE 4.4: Hartree-Fock contribution to the wavefunction correlation, \mathcal{K}_1 for pair of wavefunctions having neighboring energies. It is seen that the both the scaling function not only follow the same scaling exponent but also same amplitude at distances: $\mathbf{r}_1 - \mathbf{r}_2 \ll N$. The corresponding exponent $\Delta_2 \simeq -0.52$ is consistent with earlier multifractal analysis [66].

4.4 Results and discussions

We employed the aforementioned CCNM to calculate the eigenvalues near zero energy (pseudo energy) that constitute the correlation functions $\mathcal{K}_{1,2}$. In the present context the system size L is parameterized by the number of links, N , in both direction in the model. We use a square lattice containing $N = \{256, 512, 768, 1024, 2048\}$ links in each direction with periodic boundary conditions. Typically we use $10^4 - 10^6$ disorder configurations to average depending on the system sizes to calculate the correlation function as described in Eq. (4.2) and Eq. (4.5).

4.4.1 First order correction

In Fig. 4.4 we plot the Hartree and Fock contribution separately, the difference of which constitutes the wavefunction correlation function \mathcal{K}_1 , as defined in Eq. (4.2). It is readily seen that the power law scaling regime for both the contribution

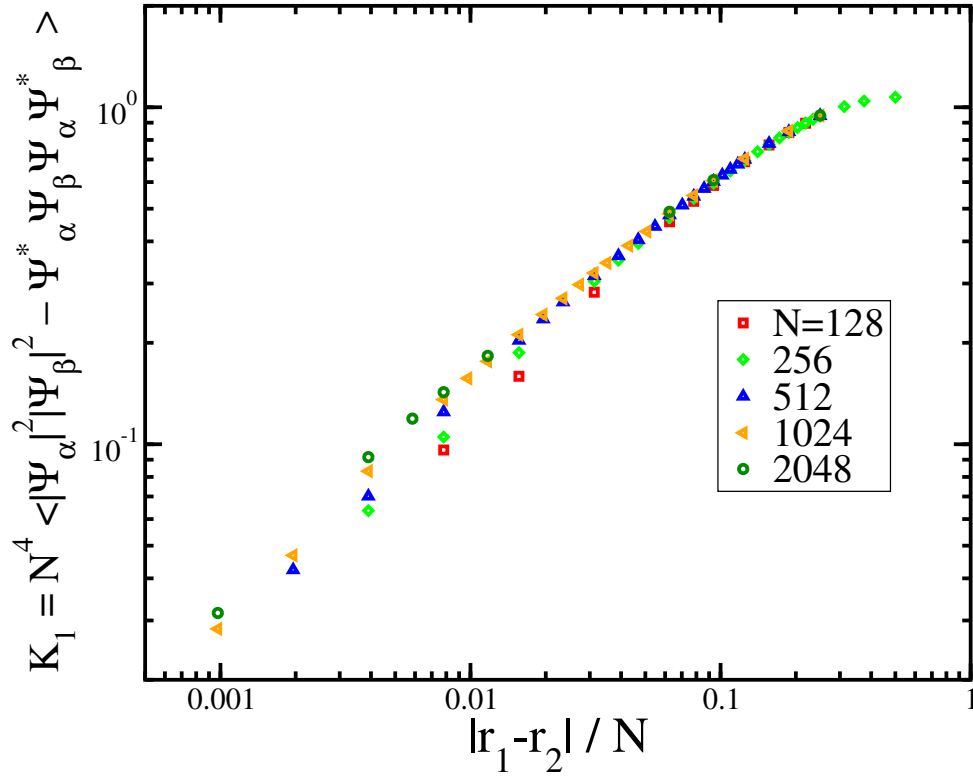


FIGURE 4.5: Shows the correlation function \mathcal{K}_1 defined as the difference between two functions shown in Fig. 4.4. The extracted value of the exponent is $\mu_2 \simeq 0.62 \pm 0.05$. Two type of deviations from the perfect scaling behavior (straight line in a double log scale) is seen in two different regime. At large distances $\mathbf{r}_1 - \mathbf{r}_2 \approx N/2$, the scaling is influenced due to system size; whereas in small distances the scaling behavior is affected due to corrections to scaling originating from the small scale in the system, i.e, the ultraviolet cutoff, a (the lattice constant).

(Hartree and Fock) is achieved in a window where the point separation is much smaller than the system size, $\mathbf{r}_1 - \mathbf{r}_2 \ll N$. The corresponding scaling exponent, $\Delta_2 \simeq -0.52$, is consistent with earlier analysis of moments of wavefunctions [66]. Note that not only the scaling of these contribution is the same but also the amplitude (pre-factor) of these two terms is similar. Thus the scaling of the correlation function \mathcal{K}_1 , Eq. 4.2, which is a difference between these two terms, is governed by the sub-leading exponent rather than the leading multifractal exponent.

In Fig. 4.5 we show the scaling of the correlation function, \mathcal{K}_1 with $|\mathbf{r}_1 - \mathbf{r}_2|/N$. As discussed in the previous paragraph the scaling in this situation is governed by the sub-leading exponent. However, the scaling here is not pure in a sense that it is not a straight line in a double log scale (see Fig. 4.5), which is mainly due to presence of different length scales in the system and related to higher sub-leading terms. For instance, in the large distance limit, $|\mathbf{r}_1 - \mathbf{r}_2|/N \gtrsim 0.1$, the scaling is affected by system size. At small distances we notice that the data for different

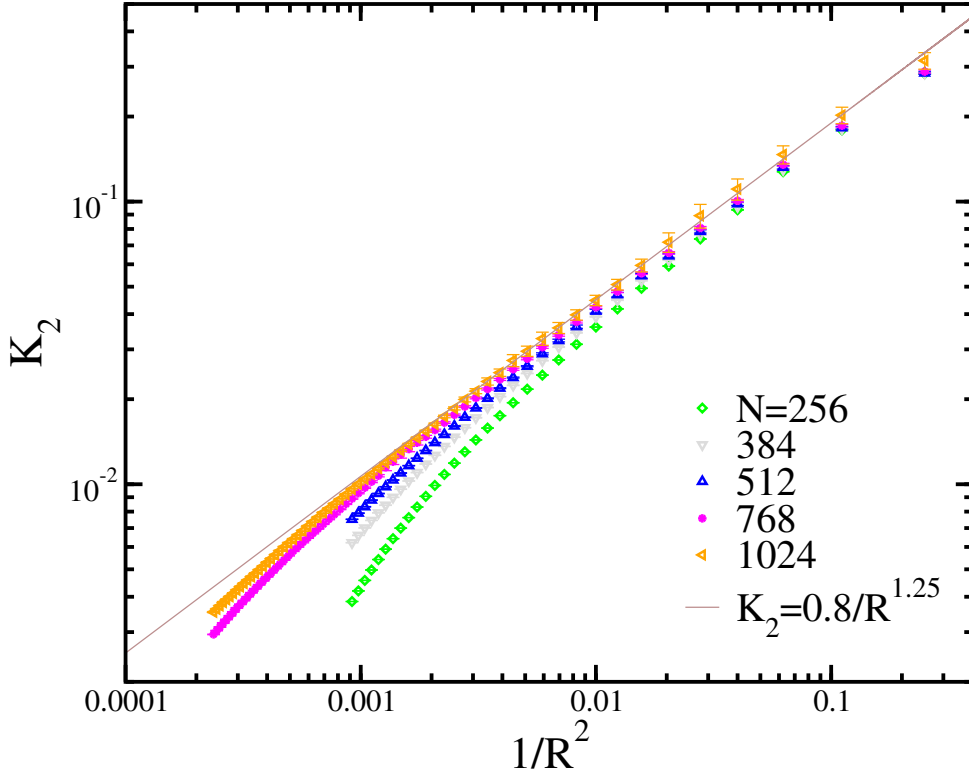


FIGURE 4.6: Shows the correlation function \mathcal{K}_2 as a function of $1/R^2$ for fixed distances $|\mathbf{r}_1 - \mathbf{r}_2| = |\mathbf{r}_3 - \mathbf{r}_4| = 1$ as defined in Eq. (4.4). The function \mathcal{K}_2 for four neighboring energies and averaged over 10^6 disorder realizations. The error bars indicate the statistical deviations. It can be seen that with increasing system size, N , the data approach a straight line in a double log scale, which indicates a power law dependence. A power law fit implies a value of exponent $\simeq 1.25$, i.e. equal to $2\mu_2$ and is consistent with previously found value (see Fig. 4.5). Within given numerical accuracy we conclude that the exponent $\alpha \simeq 0$.

system sizes do not fall on top of each other. This is because in this regime a new length scale appears, $a/|\mathbf{r}_1 - \mathbf{r}_2|$, that dominates the correction to scaling. The numerical analysis for the correlation function, \mathcal{K}_1 , yields the power law exponent $\mu_2 \simeq 0.62 \pm 0.05$.

4.4.2 Second order correction

In Fig. 4.6 we plot the function, \mathcal{K}_2 at fixed small distances $|\mathbf{r}_1 - \mathbf{r}_2| = |\mathbf{r}_3 - \mathbf{r}_4| \equiv \rho$ as a function of $1/R^2$, where $R = (\mathbf{r}_1 + \mathbf{r}_2 - \mathbf{r}_3 - \mathbf{r}_4)/2$. With increasing system sizes ($N = 256, \dots, 1024$) the data approach a straight line in a double log scale. A power law fit reveals the exponent $\simeq 1.25$, which is consistent with our previous analysis of Hartree-Fock terms. It implies that within the accuracy of our numerical analysis the exponent, α , that describes scaling with the variable

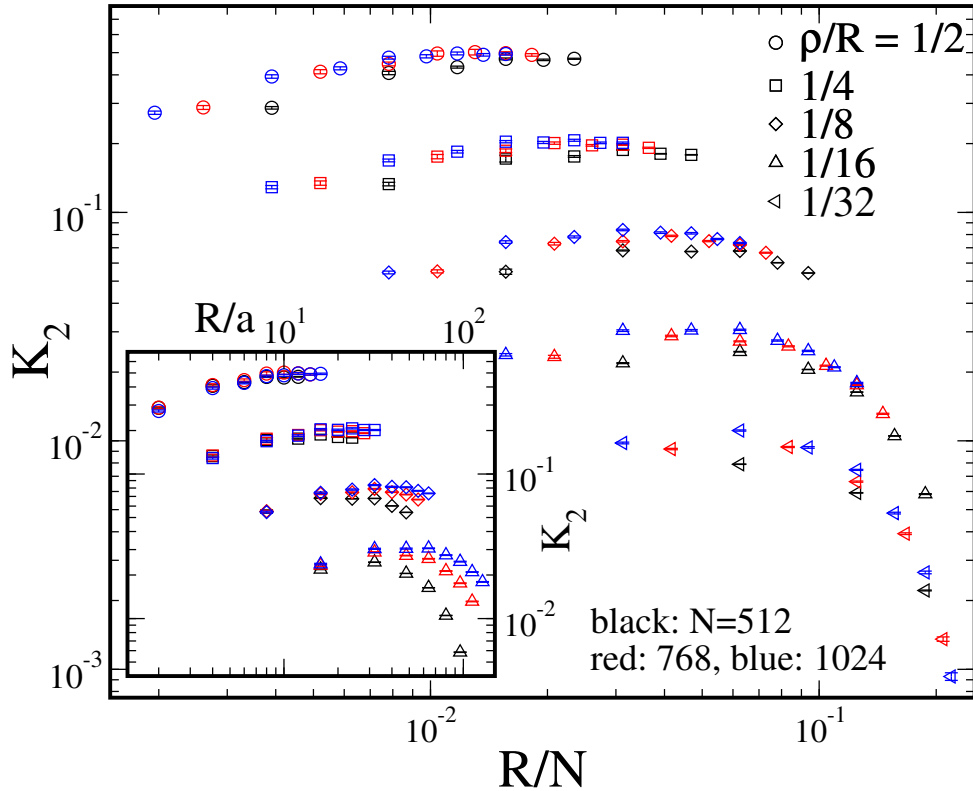


FIGURE 4.7: Main panel: Shows the scaling behavior of the function \mathcal{K}_2 as a function of R/N for fixed values of $\rho/R = \{1/2, 1/4, 1/8, 1/16, 1/32\}$. Three different colors represent three different system sizes as used in our numerical simulation, $N = 512, 768, 1024$. According to Eq. (4.4), the scaling of \mathcal{K}_2 at fixed small distances, ρ/R , is governed by $(R/L_\Omega)^\alpha$, where $L_\Omega = N$ for $R/N \ll 1$. As seen from the plot the scaling is represented by a plateau at intermediate value of R/N that indicates a value of α close to zero. At higher value of R/N the data deviates from pure scaling as the higher order terms become significant. Similarly, at small distances corrections are dominated by the parameter a/ρ . Inset: Shows the same data re-plotted as a function of R/a . It confirms that at small value of R/a there is no correction due to system size, N , and the correction to pure power law scaling is only due to a/ρ .

R/L_Ω is either zero or very small.

In order to investigate the exponent α even more carefully, we plot the function \mathcal{K}_2 as a function of R/N for fixed ρ/R in Fig. 4.7. According to Eq. (4.4), this is a direct way to probe the exponent, α . For small $R/N \lesssim 0.1$ the curves for different system sizes not only fall on top of each other but are almost flat, which indicates that the exponent is indeed close to zero ($\alpha \simeq 0$). Again in small R regime the deviation to scaling is due to the parameter, a/ρ . This is well illustrated in the inset of Fig. 4.7, where the function \mathcal{K}_2 is plotted as a function of R/a . It is easily seen that at small R/a the data deviate from pure power law scaling as it was the situation previously (see Fig. 4.5).

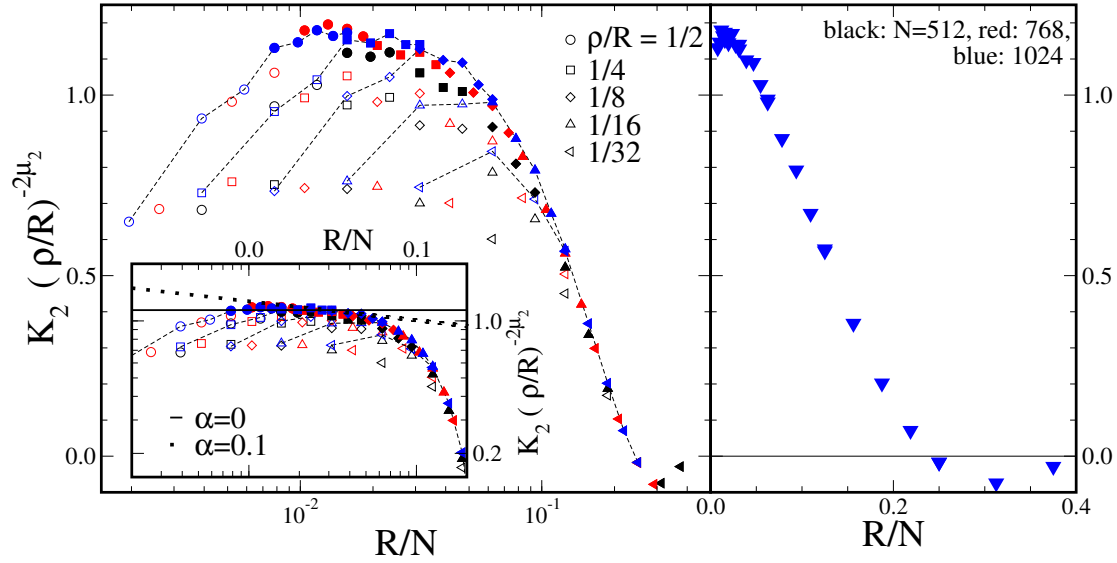


FIGURE 4.8: Left panel: Shows the function $(\rho/R)^{-2\mu_2}\mathcal{K}_2$ as function of R/N with $\mu_2 = 0.625$. Similar to Fig. 4.7, different symbols represent different value of ρ/R and different colors are for different system sizes, N . Again it emphasizes that at small values of R/N the deviation from the single parameter scaling is controlled by the parameter, a/ρ . Inset: Same data in a log-log scale. The solid line (corresponds to $\alpha = 0$) and the dotted line ($\alpha = -0.1$) indicate the power law scaling regime and the deviation from that. Right panel: Single parameter scaling function plotted as a function of R/N as obtained from the data (solid symbols) of the left panel.

In the left panel of Fig. 4.8 we re-plot the scaling function multiplying each trace by $(\rho/R)^{-2\mu_2}$, where $\mu_2 = 0.625$ is taken from Fig. 4.5 as a function of R/N . It is readily seen that the data (solid symbols) collapse on a single parameter scaling curve showing the dependence of $(\rho/R)^{-2\mu_2}\mathcal{K}_2$ on R/N . Consequently, it signals that the value of μ_2 is indeed correct and $\alpha \simeq 0$. The open symbols deviate from the single parameter scaling curve due to correction in a/ρ in small R/N range. The inset of the left panel of Fig. 4.8 shows the single parameter scaling function in a log-log scale. The plateau of the single parameter scaling curve yields a value of $\alpha \simeq -0.05 \pm 0.1$. It needs to be emphasized at this point that within the available system sizes it is indeed very complicated to have a proper error bound on the possible values of α . It is because the corrections a/ρ and R/N are not negligible within the available numerical system sizes. Furthermore, the uncertainty in the numerical determination of μ_2 also enters in the scaling analysis of the exponent α . The right panel of Fig. 4.8 shows the single parameter scaling function on a double linear scale.

4.4.3 Discussions

In this subsection we will summarize our numerical findings. Our numerical simulation of the correlation functions $\mathcal{K}_{1,2}$ yield the corresponding values of the exponents: $\mu_2 \simeq 0.62 \pm 0.05$ and $\alpha \simeq -0.05 \pm 0.1$. First of all the values nicely agree with those previously obtained by Lee and Wang [155]. Here it should be noted that the system sizes used in our calculations are at least an order of magnitude larger than in Ref. [155]. In particular, the large system sizes $N \gtrsim 500$ played an important role for the scaling analysis of the correlation function as seen in Fig. 4.7. Indeed, in order to achieve the scaling regime, i.e. $\propto (R/N)^\alpha$ and $\alpha \simeq 0$, the value of the parameter must be small, $R/N \lesssim 0.05$. At the same time the scale ρ can not be too small as the corrections to scaling due to the parameter a/ρ becomes substantial unless $\rho/a \gtrsim 4$. Consequently, it gives us a condition for a preferable parameter range where the power law is observable $R \gg \rho$, which in practice requires $R/\rho \gtrsim 2$. Our larger system sizes and the chosen parameter range allow us to explore the true scaling regime in a window of R/N approximately between 0.007 and 0.05 as seen in Fig. 4.7.

Using our estimate for μ_2 and α , we calculate the exponent κ as described in Eq. (4.6) and Eq. (4.7) in the limit of the ‘most’ short-range interaction, $\lambda > 2 + \mu_2 \simeq 2.62$. We get,

$$p \simeq 1.62; \quad z_T \simeq 1.23; \quad \kappa \simeq 0.346. \quad (4.15)$$

Here we used the localization length exponent $\nu \simeq 2.35$ as found in Ref. [156], which is confirmed by several later works as well. Although the most recent work in this direction suggests that the correction to scaling in determining the localization length exponent using the CCNM is much larger; consequently, it suggests a larger localization length exponent $\nu = 2.59$ [72]. Using this value of the exponent ν we get a smaller value of the exponent $\kappa \simeq 0.314$. In the next section we describe our numerical results in the context of experiments.

4.5 Summary and Outlook

To summarize, we have studied the scaling properties of dephasing rate, τ_ϕ , at the critical point of the IQH transition. We have considered the case of most short range Coulomb interaction in a system with broken spin-rotation symmetry, which happens in the presence of a strong magnetic field. In this situation the short-range interaction is RG-irrelevant and the scaling properties are obtained by performing the scaling analysis near the non-interacting critical point.

At this point few comments are in order: First, strictly speaking, the calculation of the dephasing rate in this work is done in the lowest order (Golden rule) of the perturbation theory; thus the most important range of frequencies that we

consider here for the dephasing rate are $\Omega \sim \epsilon' \sim T$. This estimation only allows us to have an upper bound on L_ϕ , consequently the lower bound on z_T , and the upper bound on κ . It is not easy to eliminate other possible contributions from a different scaling regime of frequencies and spatial variables to the lowest order of the dephasing rate. Nevertheless, our preliminary analysis shows that these are more unlikely, but a more detailed investigation is needed to study such exotic contribution.

Second, the experimental determination of the exponents ν and z_T is highly complicated by the fact that they are affected by the systematic errors (the scatter of data can be as big as 10%). Specifically, the works [157–159] that measured the exponent ν reported a value of κ in a range 0.6 to 0.8, which is much larger than the true exponent $\kappa \simeq 0.42$. Further complications arise in direct determination of the exponent z , which is based on the analysis of the data for different system sizes [146]. Here problem originates due to the correlation of disorder with the sample width. The effect is not small as it is seen in Ref. [146], where by changing the sample width by a factor of ≈ 5 not only changes the saturation temperature by a factor of ≈ 5 but also changes the characteristic temperature scale by a factor of ≈ 2.5 . Consequently, that affects the determination of the exponent z_T . More experimental works are needed in this direction to overcome these difficulties in determining the exponents ν and z_T .

Finally, let us comment on the experimental value of κ and our numerical findings. The most updated experimental values of the exponents are $\nu \simeq 2.3 \pm 0.1$, $z_T \simeq 1.0 \pm 0.1$ and $\kappa \simeq 0.42 \pm 0.01$, where we believe that the errors bound are considerably underestimated due to systematic errors. Now let us compare these values with the latest theoretical values of the exponents: $\nu \simeq 2.35 - 2.39$, $z_T \simeq 1.23$ and using Eq. (4.7), we get a value of κ in a range 0.314 to 0.346, which is much smaller than the true exponent value found in the experiments. The difference between the theory (short-range interaction) and experiments (long-range interaction) is not so large considering the systematic errors in the experimental determination of the exponents ($\lesssim 10\%$ for ν , $\lesssim 20\%$ for z_T and $\lesssim 30\%$ for κ). Nevertheless, it suggests that current experiments at the IQH critical point can not be explained by the present theory considered at the non-interacting fixed point in our work. Either a controlled experiment in the case of short-range interaction is needed or a theory at the IQH critical point for long-range electron-electron interaction is required for further advancement in this direction.

5

CHAPTER 5

Conclusion

The aim of this thesis was threefold. Along with the material properties of graphene, we have investigated the transport properties of this novel material in the presence of disorder and a magnetic field. It has been observed in several experiments that graphene shows surface corrugation (“ripples”) even at relatively low temperatures. Their origin is thought to be due to the residual strain originating from experimental preparation techniques. For instance, residual strain can be induced by the presence of a substrate or by a scaffold, where graphene sheets are freely suspended in vacuum or in air. Motivated from these experimental observations, in the first part we have studied the effects of strain, including edge effects, on the elastic properties of small graphene flakes. Combining a phenomenological theory and density functional theory calculations we have calculated independently all the Lamé parameters. To estimate the finite size effects on these, we analyze the total energy of a flake in two different ways, i.e. by an atomic energy representation and by a representation in terms of the bond energies. These two different ways of representing the total energy elucidate one important observation, namely that edge effects can be significant for the elastic properties. For instance, for the shear strain the dependency of the elastic constant, μ , on the flake size can be as large as 70%. Additionally, we also investigate the effects of zero point motion on the elastic parameters. For example, we observe that the zero point motion renormalizes the transverse stiffness (or bending rigidity, κ) significantly, by about 26% [104].

Apart from having considerable effects on the elastic properties of small flakes, strain also has important consequences on the low energy electronic properties of graphene. For instance, it has been shown that ripples induce an effective magnetic field; although, it does not break the overall time reversal symmetry of the system, it can lead to a non-trivial quantum Hall physics without an external magnetic field. Thus understanding the transport characteristics of graphene in the presence of various types of disorder poses a considerable amount of challenge in experiments.

Here, we analyze the density of states and the transport properties of graphene in the presence of such disorder, namely vacancies. To analyze the density of states we develop a numerical method along with V. Häfner, which is particularly suited to calculate the density of states and other observables (such as conductivity) for large systems. In clean graphene due to the presence of chiral symmetry, a vacancy gives rise to a state exactly at the Fermi energy (“zero mode”). For a finite concentration of vacancies the density of states is sensitive to the distribution of vacancies in different sub-lattices. For instance, our numerical simulation confirms that for a finite concentration of vacancies, which are distributed only in one of the sub-lattices only, the number of zero modes is given by exactly the number of vacancies.

In collaboration with P. Ostrovsky, who has developed a general theory to describe graphene with an arbitrary number of isolated impurities based on the Dirac equation, we analyze the transport properties of graphene at the charge neutrality point in the presence of a finite concentration of vacancies. By analyzing the distribution function for different vacancy concentrations we investigate the ‘self-averaging’ property of the conductivity in such a system. Our numerical simulation reveals that the conductivity in such a system not only depends on the impurity concentrations but also on the distribution of vacancies in different sub-lattices. Additionally, with increasing vacancy concentrations we observe a crossover from the ballistic to the diffusive regime. In the diffusive regime the conductivity saturates at two different constant values depending on the vacancy distribution between different sub-lattices. This indicates a new fixed point, which is beyond the standard σ -model RG analysis, and has a non-trivial scaling behavior [137].

In our previous study we noticed that the effect of many impurities can not be understood by considering only one defect, i.e. a single vacancy. This is because in the presence of more than one vacancies wave function forms a complicated interference pattern. Moreover, the wave function amplitudes have large fluctuations in space; this behavior is generic for any strongly disordered metal. In the presence of a magnetic field the situation becomes even more interesting, i.e. a quantum Hall transition. At the quantum Hall critical point the fluctuations in the wave-function amplitude are characterized by the multifractality. This multifractal behavior also manifests itself in other correlation functions calculated at the critical point. In particular, we encounter such scaling behavior when considering the matrix elements of the short range Coulomb interaction. Motivated from the experimental findings in this part of the thesis we investigate the effect of dephasing induced by the electron-electron interaction at finite temperature on a quantum Hall critical point in collaboration with I. Burmistrov. In our study we address this question by combining a perturbation theory in the interaction near the non-interacting fixed point and a numerical simulation based on the Chalker-Coddington network model. We numerically calculate the scaling of the correlation functions that appear in the interaction correction to the self-energy

at the non-interacting integer quantum Hall critical point. It turns out that the in the first order interaction correction the correlators combine in a way such that the *leading* multifractal power laws cancel; the subleading terms govern the interaction corrections. Here we determine quantitatively the sub-leading multifractal exponents, μ_2 , of the salient wave function correlators [143]. In particular our numerical estimation of the exponent $\mu_2 \simeq 0.62 \pm 0.05$, which is consistent with earlier calculation by Lee and Wang [155]. Moreover, with our improved efficient computer code we have been able to achieve system sizes containing $\sim 5 \times 10^6$ nodes, which becomes extremely important to reach the true scaling regime. Using the estimates for μ_2 and $\alpha \simeq -0.05 \pm 0.1$, we get a value of the critical exponent, $\kappa \simeq 0.346 \pm 0.035$. This value, however, differ from some experimental findings and we discuss the origin of this discrepancies in Chapter 4.

A

APPENDIX A

Symmetry classification of disordered metals

In general the presence or absence of certain symmetries, such as translational invariance, time reversal etc., plays a major role in the classification of disordered electron systems in a systematic way. A classification scheme of random Hamiltonians based only on time reversal and spin rotation symmetries was first proposed by F. Dyson [160] after E. Wigner [161] pointed out that random matrix theory has a very broad application in physical problems. The “Wigner-Dyson” ensemble comprises the three generic classes, the “unitary”, the “orthogonal”, and the “symplectic”, combining only two symmetry properties, i.e. time reversal (TR) and spin rotation (SR). Later in the 1990’s Gade and Wegner emphasized that TR and SR are not the only two symmetries that can exist in nature. For instance, in bipartite systems the sub-lattice [55, 162] symmetry (SLS) plays an important role in determining its critical properties and the density of states. In the continuum limit this symmetry manifest itself as the chiral symmetry in the Dirac Hamiltonian. The symmetry classification was completed by Atland and Zirnbauer [163] by including the particle-hole symmetry (PHS) that arises most naturally in superconducting systems and is incorporated in the Bogoliubov-de Gennes (BdG) Hamiltonian. Below we briefly describe the different symmetry classes arising from the combination of the symmetries mentioned earlier.

A.1 Symmetry classification scheme

A.1.1 Wigner-Dyson classes

Using TR and SR invariance three symmetry classifications are possible within the Wigner-Dyson scheme: unitary, orthogonal and symplectic. When time reversal invariance is broken, the Hamiltonians become general Hermitian matrices,

$$H = H^\dagger. \quad (\text{A.1})$$

In this class the presence or absence of SR invariance does not yield any new symmetry classification. This set of matrices is invariant under the unitary transformation; thus the name “unitary” class. In the presence of TR invariance, the Hamiltonian is invariant under the operation,

$$H = KH^TK^{-1}, \quad (\text{A.2})$$

where K is the unitary operation represented via the anti-unitary TR operator as $\mathcal{T} = KC$ and C being the complex conjugation operator. Since by definition acting of TR operator, \mathcal{T} , twice leaves the Hamiltonian invariant, the square of the unitary operator, K , can have two possible values, $K^2 = p$, where $p = 1$ represents the systems with integer angular momentum; similarly $p = -1$ corresponds to a system with half-integer angular momentum where TR is preserved but SR invariance is broken.

A.1.2 Chiral classes

In the chiral classes the Dirac Hamiltonian has the following block structure in the sub-lattice space,

$$H = \begin{pmatrix} 0 & h \\ h^\dagger & 0 \end{pmatrix} \quad (\text{A.3})$$

and the chiral symmetry is represented by,

$$\sigma_z H \sigma_z = -H. \quad (\text{A.4})$$

where σ_z is the Pauli matrix in the “iso-spin” space. A popular example of a material that belongs to this class is graphene. Similar to the Wigner-Dyson classes, the chiral ensemble can also possess TR and SR invariance, thus it is also subdivided into three chiral classes- denoted “chiral unitary”, “chiral orthogonal”, and “chiral symplectic”.

Symmetry classes	Cartan-nomenclature (Hamiltonian)	RMT	TR	SR	PHS	SLS
Wigner-Dyson	A (unitary)	GUE	−	±	−	−
	AI (orthogonal)	GOE	+	+	−	−
	AII (symplectic)	GSE	+	−	−	−
Chiral	AIII (chiral unit.)	chGUE	−	±	−	+
	BDI (chiral orho.)	chGOE	+	+	+	+
	CII (chiral sympl.)	chGSE	+	−	+	+
BdG	C		−	+	+	−
	CI		+	+	+	+
	D		−	−	+	−
	DIII		+	−	+	+

TABLE A.1: Symmetry classifications of disordered systems. First column: Name of different symmetry classes. Second column: Cartan nomenclature of the symmetry classes. Third column: Name of the corresponding Random matrix theories (RMT). Fourth, fifth, sixth and seventh columns describe the absence (−) or presence (+) of time reversal (TR), spin rotation (SR), particle-hole (PHS), and sub-lattice symmetries (SLS) in the disordered Hamiltonians, respectively. Adapted from Ref. [66].

A.1.3 Bogoliubov-de Gennes classes

The other four classes appear naturally in disordered superconducting systems with particle-hole symmetry. The most general single particle Hamiltonian for such systems is given by,

$$H = \sum_{\alpha,\beta}^N h_{\alpha,\beta} c_{\alpha}^{\dagger} c_{\beta} + \frac{1}{2} \sum_{\alpha,\beta}^N (\Delta_{\alpha,\beta} c_{\alpha}^{\dagger} c_{\beta}^{\dagger} - \Delta_{\alpha,\beta}^{*} c_{\alpha} c_{\beta}) \quad (\text{A.5})$$

where, $c_{\alpha,\beta}$ ($c_{\alpha,\beta}^{\dagger}$) is the fermionic annihilation (creation) operator. $h_{\alpha,\beta}$, $\Delta_{\alpha,\beta}$ are the $N \times N$ matrices with $h = h^{\dagger}$ and $\Delta^{\text{T}} = -\Delta$. Now it is straight forward to give the Hamiltonian, Eq. (A.5), a matrix representation ($\hat{H} = \psi^{\dagger} H \psi$) by considering the c and c^{\dagger} in spinor notation, $\psi_{\alpha}^{\dagger} = (c_{\alpha}^{\dagger}, c_{\alpha})$, and,

$$H = \begin{pmatrix} h & \Delta \\ -\Delta^{*} & -h^{\text{T}} \end{pmatrix} \quad (\text{A.6})$$

The minus sign represents the fermionic commutation relations of c and c^{\dagger} operators. This specific construction of the Hamiltonian respects the particle hole symmetry (PHS) as,

$$H = -\sigma_x H^{\text{T}} \sigma_x \quad (\text{A.7})$$

where, σ_x is the Pauli matrix in the particle-hole space. The above condition represents the class of disordered superconductors in the absence of other symmetries and is denoted as D in Cartan representation and presented in the second last row of Tab. A.1. Unlike the Wigner-Dyson and chiral classes, the absence of TR invariance for the spin full systems is important, since it combines the PHS in a non-trivial way. The Hamiltonian is represented in the same way as in Eq. (A.6), where now the spinor wavefunctions have an extra spin index, $\psi_\alpha^\dagger = (c_{\alpha\uparrow}^\dagger, c_{\alpha\downarrow})$. The Hamiltonian then possesses another symmetry property,

$$H = -\sigma_y H^T \sigma_y. \quad (\text{A.8})$$

The ensemble of Hamiltonians with spins that exhibit the above symmetry, Eq. (A.8), represents the class C in the symmetry classification scheme. If TR invariance is present one obtains two more symmetry classes (CI and DIII) similar to the chiral classes.

A.2 Importance of the symmetry classifications

Conductance: The most fundamental observable to characterize a metal is its *conductance*, g . In a linear response regime it is the proportionality constant in the current voltage relationship and is defined as,

$$I = \frac{e^2}{h} gV \quad (\text{A.9})$$

where, V is the applied voltage and I is the measured current in the system. In general, the conductance is a material property that also depends on the system geometry, e.g. due to Ohm's law.

β -function: In order to understand the effect of disorder in metals, it is essential to take the wave nature of the quasi-particles into account. In a disordered environment the wavefunctions form a complicated interference pattern that leads to the localization of the wavefunctions in real space, which was discovered by Anderson [164]. For long (quasi) one-dimensional disordered wire the electronic wave-functions are localized in real space, which implies that the conductance of such systems drops in an exponential way, $e^{-L/\xi(E_F)}$, - faster than the inverse of the length of the system, L^{-1} - where ξ is the localization length and E_F is the Fermi energy. The characteristic of this transition can be understood in the framework of the one parameter scaling theory [165], which describes the flow of the dimensionless conductance with the system size in terms of a β -function,

$$\frac{d \ln g}{d \ln L} = \beta(g) \quad (\text{A.10})$$

The scaling theory was given a more solid foundation after the formulation of the field theoretical description of the problem in the context of a nonlinear σ -model¹. The model allows one to calculate systematically the β -function (flow equation) using the field-theoretical renormalization group (RG) approach by doing a resummation of the singularities in the perturbation theory near or at two-dimension ($2+\epsilon$ dimension). For critical properties and exponents in a system with given symmetries one needs to calculate the β -function, $\beta(t) = -dt/d \ln L$, perturbatively in the coupling constant, $t = 1/2\pi g$, using a specific sigma model that belongs to the specific symmetry classes listed in Tab. A.1. The β -function provides information about the localization of electronic states in a very effective way.

The form of the β -function is mainly determined by the symmetries of the problem and the physical dimension of the system, which we discuss briefly in the next paragraph.

Discussion: Here we will discuss some of the aspects of the β -function for the localization problem in the context of the symmetry classes discussed above. For instance, in one and two dimensions the β -function in conventional symmetry classes is always negative (without any topological term in the sigma model), which signifies that all states are localized in two-dimension; therefore the system is an insulator. For dimension $d > 2$ in the orthogonal and the unitary symmetry classes the situation changes as the β -function changes its sign giving rise to an unstable fixed point, g_c , where $\beta(g_c) = 0$; thus the system undergoes a *metal-to-insulator* transition, i.e. an Anderson transition. This is because Anderson localization is mainly due to multiple scattering events at the same impurity, which enhances the interference between wave-functions. In dimension greater than two the return

¹In order to fully appreciate the symmetry classification scheme, it is important to have a basic understanding of the associated field theories in different symmetry classes. Here we only present the corresponding field theoretical model for pedagogical purpose without any derivations; for a more detailed discussions readers are encouraged to look at a recent review on the subject Ref. [66]. The σ -model [166–168] is the effective low-energy long wavelength microscopic theory of the system that describes the dynamics of the interacting soft modes (diffusion and cooperons). For unitary symmetry class (A) the σ -model action is given by,

$$S[Q] = \frac{\pi\rho}{4} \int d^d \mathbf{r} \text{Str}[-D(\nabla Q)^2 - 2i\omega\Lambda Q] \quad (\text{A.11})$$

where, ρ is the density of states, D being the diffusion constant. The Q in the super-symmetric formulation represents a 4×4 super matrix that satisfies the condition $Q^2 = 1$ with $\Lambda = \text{diag}(1, 1, -1, -1)$ and Str represents the super-trace. The 4×4 structure of the matrix is because it incorporates two type of Green's function (advanced and retarded) which is represented via the bosonic and the fermionic degrees of freedom in terms of a functional integral. In principle one can also have a $n \times n$ super-matrix that represents n advanced and n retarded Green's function; consequently, the σ -model is defined on a larger manifold. For other symmetry classes the general form of the σ -model is same but the underlying symmetry properties of the σ -model is different along with the dimension of the manifold of the Q matrices.

probability to a same point is not sufficiently large to localize all electronic wavefunctions; thus systems with dimension $d > 2$ can have metallic phase.

The situation changes in the symplectic class (AII), where the β -function is related to the orthogonal class via [46],

$$\beta_{\text{sp}} = -2\beta_{\text{ortho}}(-t/2) \quad (\text{A.12})$$

where $t = 1/\pi g$ and g is the conductance of the spinful system. It implies that the β -function is positive for small $t < t^*$ and a true metallic phase exists with an Anderson transition at some specific $t^* \sim 1$. As mentioned earlier that in two-dimension all states are localized in the conventional symmetry classes (A, AI, C, CI; without any topological term in the sigma model), the symplectic class is very special in a sense that it represents a mechanism to have a critical fixed point even in two-dimension. For the chiral classes, AIII, BDI, and CII the β -function is exactly zero at all orders of the perturbation series in two-dimension, implying that these classes support a phase with non-zero conductance, which is either metallic or critical (or a line of fixed points) [55, 162]. In other symmetry classes, D and DIII, which corresponds to systems with broken SR invariance, the β -function is positive at small t , denoting the existence of a metal-insulator transition in two-dimension in the strong coupling limit. The behavior is similar to the one found in the class AII (symplectic Wigner-Dyson class); these symmetry classes correspond to systems with broken spin rotation invariance, where the unconventional sign of the β -function signifies a weak anti-localization rather than the conventional localization of the electronic wavefunction [46].

In some situations the σ -model allows for an extra term in the action, which is invisible to any orders of the perturbation series; thus the resulting β -function is different. For instance, for some physical systems that belongs to class A or C or D the action includes a topological θ -term that has a value in the interval $[0, 2\pi]$,

$$iS_{\text{topo}}[Q] = i\theta N[Q] \quad (\text{A.13})$$

$N[Q]$ is an integer represents the winding number of the field configuration, $Q(\mathbf{r})$. A classical example of appearance of such a term is first identified by Pruisken [169] in the context of the integer quantum Hall effect (symmetry class A). But it only describes the microscopic theory of the quantum Hall critical point in the weak coupling limit. For the class, AII, the θ -term takes a special value, $\theta = \pi$ in the model of Dirac fermions with random scalar potential (e.g. graphene with long range disorder) [50]. This topological term inhibits localization and known as \mathbb{Z}_2 topological term.

Another possibility for criticality in two-dimension arises in classes AIII, C, and DIII, where the Wess-Zumino (WZ) term in the σ -model plays the major role.

The WZ term has the following form,

$$iS_{WZ}(g) = \frac{ik}{24\pi} \int d^2\mathbf{r} \int_0^1 ds \epsilon_{\mu\nu\lambda} \text{Str}(g^{-1}\partial_\mu g)(g^{-1}\partial_\nu g)(g^{-1}\partial_\lambda g) \quad (\text{A.14})$$

where k is the integer denotes the level of the WZW model [68]. For instance, the model of Dirac fermions in random vector potential (chiral unitary, AIII) is described by including the WZ term in the action. In this scenario the σ -model coupling constant is truly marginal yielding a line of fixed points as mentioned previously. In the next section we will present a similar discussion, where we will see how different terms (θ -term or WZ term) appear in the σ -model action for different types of disorder in graphene.

A.3 Symmetries in clean graphene

Here we analyze the symmetries of clean graphene Hamiltonian given in the AB and KK' space as defined in 1.7, which we use later to classify different transport properties of graphene in the presence of disorder. The discussion presented here is mostly follows from Ref. [46]. As discussed in introduction 1 that the effective continuum two-dimensional Hamiltonian of graphene in AB and KK' spaces has the following form,

$$H = v_F \tau_z \boldsymbol{\sigma} \cdot \mathbf{k} \quad (\text{A.15})$$

where τ_z is the third Pauli matrix in the KK' space. First, the three generators of the iso-spin, which form the SU(2) group and commute with the Hamiltonian is given by,

$$\Lambda_x = \sigma_z \tau_x, \quad \Lambda_y = \sigma_z \tau_y, \quad \Lambda_z = \sigma_z \tau_z. \quad (\text{A.16})$$

Next there exists two fundamental symmetries of clean Hamiltonian which are the time inversion, (T_0) and the chiral symmetry (C_0). Now combining T_0 , C_0 and iso-spins ($\Lambda_{0,x,y,z}$) one can in total constructs 12 more symmetry operations. These 12 symmetries can be classified in three different symmetry groups, namely, of time-reversal type (T_μ), of chiral type (C_μ) and of Bogoliubov-de Gennes type (CT_μ). These 12 symmetries can be represented by the following notations:

$$\begin{aligned} T_0 : A &\mapsto \sigma_x \tau_x A^T \sigma_x \tau_x, & C_0 : A &\mapsto -\sigma_z \tau_0 A \sigma_z \tau_0, & CT_0 : A &\mapsto -\sigma_y \tau_x A^T \sigma_y \tau_x, \\ T_x : A &\mapsto \sigma_y \tau_0 A^T \sigma_y \tau_0, & C_x : A &\mapsto -\sigma_0 \tau_x A \sigma_0 \tau_x, & CT_x : A &\mapsto -\sigma_x \tau_0 A^T \sigma_x \tau_0, \\ T_y : A &\mapsto \sigma_y \tau_z A^T \sigma_y \tau_z, & C_y : A &\mapsto -\sigma_0 \tau_y A \sigma_0 \tau_y, & CT_y : A &\mapsto -\sigma_x \tau_z A^T \sigma_x \tau_z, \\ T_z : A &\mapsto \sigma_x \tau_y A^T \sigma_x \tau_y, & C_z : A &\mapsto -\sigma_z \tau_z A \sigma_z \tau_z, & CT_z : A &\mapsto -\sigma_y \tau_y A^T \sigma_y \tau_y. \end{aligned}$$

In Tab. 1.1 we list few possible disorder types and corresponding symmetries that are present in the disordered graphene Hamiltonian.

B APPENDIX B

Density Functional Theory

Density functional theory (DFT) is a very efficient method to calculate the ground state energy of an interacting many-body system in an external potential, which is usually the potential from ion-cores. In many-body physics the main numerical difficulty comes from the fact that the Hilbert space dimension increases exponentially; thus treating many-body system exactly (e.g exact diagonalization) is only possible for rather small systems. Because of this, the numerical simulations of physical system are always based on some drastic approximations. In this respect DFT is particularly effective when one deals with large systems with $10^3 - 10^4$ electrons due to its efficient numerical formulation compared to other *ab-initio* methods, i.e. efficient scaling with number of electrons ($O(N^3)$). Because, instead of trying to find the solution of the many-body Schrödinger equation, in DFT one only looks at the ground state density, which has much less degrees of freedom than the wave-functions themselves. That such formulation is possible is not at all obvious to start with, because of the reason mentioned before. For pedagogical purpose, here we only give an outline of the basic formulation of the DFT without any detail derivation and proof. The following discussion is largely based on the lecture notes of F. Evers [170].

In DFT almost everything (observables) can be obtained, in principle, by solving an optimization problem for the ground state (GS) density, $n(\mathbf{r})$, alone,

$$E_0[n(\mathbf{r})] = \min_{n(\mathbf{r})} \left[\mathcal{F}[n] + \int d\mathbf{r} v_{\text{ex}}(\mathbf{r}) n(\mathbf{r}) \right], \quad (\text{B.1})$$

where v_{ex} describes the system specific, external potential (due to the ion cores) and \mathcal{F} describe a functional of the GS density, which is independent of v_{ex} and E_0 being the GS energy. The functional, $\mathcal{F}[n]$ (Eq. (B.1)) can be expressed in terms

of three energies,

$$\mathcal{F}[n(\mathbf{r})] = T[n(\mathbf{r})] + E_{\text{H}}[n(\mathbf{r})] + E_{\text{xc}}[n(\mathbf{r})], \quad (\text{B.2})$$

where E_{H} and E_{xc} are the Hartree and exchange-correlation energies, respectively. $T[n(\mathbf{r})]$ defines the single particle kinetic energy. The Hartree term is given by,

$$E_{\text{H}}[n(\mathbf{r})] = \frac{e^2}{2} \int \int \frac{n(\mathbf{r}_1)n(\mathbf{r}_2)}{|\mathbf{r}_1 - \mathbf{r}_2|} d\mathbf{r}_1 d\mathbf{r}_2, \quad (\text{B.3})$$

where $n(\mathbf{r}_1)$ is the GS density at the point \mathbf{r}_1 . Except the exchange-correlation, E_{xc} , the other three parts of the energy functional (Eq. (B.1)) are known exactly. In practice E_{xc} is given by approximations, some of which we discuss later.

In principle DFT provides a way to calculate the exact physical observables by minimizing the density functional. However, in practice exact form of the functionals (energy) are not known except for few smaller systems. Approximations are needed for E_{xc} and we discuss few of those in the following sections.

B.1 Kohn-Sham formalism in a nutshell

The *Kohn-Sham formalism* [171, 172] is the most useful implementation of DFT in practice. In this formalism the optimization problem of Eq. B.1) is solved by introducing a set of ortho-normalized ($\langle \phi_\ell | \phi_{\ell'} \rangle = \delta_{\ell, \ell'}$) single particle orbitals that re-parameterize the density as,

$$n(\mathbf{r}) = \sum_{\ell=1}^N |\phi_\ell(\mathbf{r})|^2, \quad (\text{B.4})$$

where $\phi_\ell(\mathbf{r})$ are the single particle Kohn-Sham orbitals. N denotes the number of particles. With this new parameterization the optimization problem (Eq. B.1) can be reformulated as single particle problem in an external potential (v_{s}) with single particle energy levels (ϵ_ℓ) as,

$$\left[-\frac{1}{2m} \Delta + v_{\text{s}}(\mathbf{r}) \right] \phi_\ell(\mathbf{r}) = \epsilon_\ell \phi_\ell(\mathbf{r}); \quad (\text{B.5})$$

with a relation to the ground state energy,

$$\frac{1}{2} \frac{\partial}{\partial \phi_\ell(\mathbf{r})} E_0[n(\mathbf{r})] = \left[-\frac{1}{2m} \Delta + v_{\text{s}}(\mathbf{r}) \right] \phi_\ell(\mathbf{r}), \quad (\text{B.6})$$

where $v_{\text{s}} = v_{\text{ex}}(\mathbf{r}) + v_{\text{H}}(\mathbf{r}) + v_{\text{xc}}(\mathbf{r})$, $v_{\text{H}}(\mathbf{r})$ denotes the Hartree interaction. The third term in the decomposition is the exchange correlation potential that incorporates complicated many body interaction. We have thus replaced the many-body in-

tracting problem by an effective single particle (Kohn-Sham particles) problem. The Hartree and exchange-correlation potentials are given by,

$$v_{\text{H}}(\mathbf{r}) = e^2 \int \frac{n(\mathbf{r}')}{|\mathbf{r} - \mathbf{r}'|} d\mathbf{r}', \quad v_{\text{xc}}(\mathbf{r}) = \frac{\delta E_{\text{xc}}[n(\mathbf{r})]}{\delta n(\mathbf{r})}. \quad (\text{B.7})$$

At this point few comments are in order. First it should be noted that the Hartree (v_{H}) and exchange potential (v_{xc}) are themselves depend on the GS density. So the above Eq. B.6 has to be solved self-consistently (SC). However, in DFT the SC problems are much easier to solve than, for instance, the Hartree-Fock (HF) equations, which are non-local in space. Moreover, in HF the orbital dependency is tricky in a sense that a real HF orbitals interact with $N - 1$ real orbitals, while a virtual orbital interacts with N real orbitals. In DFT all the orbitals feel the same effective potential, $v_{\text{s}}(\mathbf{r})$, as mentioned in Eq. (B.5).

In order to solve the self-consistent equations for the single particle problem, exchange correlation function need to be approximated. Here we discuss few of the approximations that are used in practice to estimate the exchange correlation function.

B.1.1 Local density approximation

The exact dependence of $E_{\text{xc}}(\mathbf{r})$ on the GS density, $n(\mathbf{r})$, is not known. In the simplest approximation, the *Local Density Approximation* (LDA) [172], one takes for v_{xc} the result obtained from the homogenous electron gas but replacing the homogenous density with $n(\mathbf{r})$. In the LDA approximation, the exchange correlation function is assumed to be local and has the form,

$$E_{\text{xc}}[n(\mathbf{r})] = \int d^3\mathbf{r}' \epsilon_{\text{xc}}^{\text{homo}}(\mathbf{r}, [n(\mathbf{r}')]) n(\mathbf{r}) \quad (\text{B.8})$$

where $\epsilon_{\text{xc}}^{\text{homo}}(\mathbf{r}, [n(\mathbf{r}')])$ is the exchange correlation functional in the homogenous Fermi gas. The exchange correlation function $\epsilon_{\text{xc}}^{\text{homo}}(\mathbf{r}, [n(\mathbf{r}')])$ depends primarily on the density near the point \mathbf{r} . The Dirac exchange [173] and the correlation in an uniform Fermi gas is given by [174],

$$\begin{aligned} \epsilon_{\text{X}}^{\text{homo}}(n)/\mathcal{V} &= -n \frac{3k_{\text{F}}}{4\pi} = -\frac{0.458}{r_{\text{s}}} \\ \epsilon_{\text{C}}^{\text{homo}}(n)/\mathcal{V} &= -\frac{0.44}{r_{\text{s}} + 7.8} \end{aligned} \quad (\text{B.9})$$

where r_{s} is the Wigner-Seitz radius ($n=3r_{\text{s}}^3/4\pi$) and k_{F} is the Fermi wave vector. The correlation part is obtained by interpolating the high and low density ($r_{\text{s}} \gg 1$) limit in a homogeneous Fermi gas from the analytical continuation by performing a $1/r_{\text{s}}$ expansion [175].

This approximation is formally valid as long as the density of the system varies slowly on the scale of local Fermi wavelength (λ_F). It does, however, give excellent results in a broad regime. Similarly, it is also known that LDA has several other problems. For instance, it is known that LDA overestimates the binding energy of covalent bonds of two-atomic molecules by few electron volts. Similar situation arises for the ionization potential. Nevertheless, it turned out that for many molecular and chemical systems, where density has strong fluctuations, LDA give reasonable results for certain properties. For instance, bond length and geometries (structure) of molecular system in LDA is predicted within an error of 1% only.

B.1.2 Generalized gradient approximation

In the *Generalized Gradient Approximation* (GGA) [176] the idea is to expand the effective functional, $\mathcal{F}_{xc}[n]$ in the electron density, $n(\mathbf{r})$, and include first order corrections, $\nabla n(\mathbf{r})$, such that the sum rules are satisfied [170]. The GGA correction to the exchange correlation potential is expressed in terms of an analytical function, called the enhancement factor;

$$E_{xc}^{\text{GGA}}[n(\mathbf{r})] = \int d^3\mathbf{r} n(\mathbf{r}) \epsilon_{xc}^{\text{homo}} \mathcal{F}_{xc}(n(\mathbf{r}), \nabla n(\mathbf{r})) \quad (\text{B.10})$$

\mathcal{F}_{xc} is written in terms of Wigner-Seitz radius, r_s and reduced density gradient, $s(\mathbf{r})$,

$$s(\mathbf{r}) = \frac{|\nabla n(\mathbf{r})|}{2k_F(\mathbf{r})n(\mathbf{r})} \quad (\text{B.11})$$

The actual form of $\mathcal{F}_{xc}[n]$ is then determined by fitting experimental data or some other numerical methods (e.g Monte-Carlo technique). A common problem of both LDA and GGA functionals is the self-interaction problem. This is because both the functionals are (semi-) local in space; thus the effective potential generated by the total electron density will cause an electron to interact with its own density. Another aspect that has not been taken into account in LDA and GGA functionals is the van-der-Waal forces.

In spite of all these deficiencies, GGA turns out to be very useful method in improving the early functionals in DFT for many examples; such as, reduction in over-binding in the molecular systems. For binding energy, GGA seems to have less error than LDA; for instance, in a small two-atomic molecules the error in binding energy for GGA functionals compared to LDA is reduced by a factor of 5.

B.1.3 Hybrid Functionals

Hybrid functionals is another attempt to improve beyond the GGA functionals. These functionals reduce the self-interaction problem by mixing Hartree-Fock energy to the exchange part of the functional. The functionals have the following generic form [111],

$$E_{xc}^{\text{Hybrid}} = \alpha E_{xc}^{\text{LDA}}[n(\mathbf{r})] + \beta(E_x^{\text{HF}}(\{\phi_i(\mathbf{r})\}) - E_x^{\text{LDA}}[n(\mathbf{r})]) + \gamma E_x^{\text{GGA}}[n(\mathbf{r})] \quad (\text{B.12})$$

where the coefficients α, β, γ controls the mixing between LDA, GGA, and HF functionals. Note that this approximation goes beyond the DFT formalism as the HF energy does not depend only on the GS density but also on the single particle orbitals, $\phi_i(\mathbf{r})$ and calculated using other empirical methods.

Hybrid functionals are better in improving the self-interaction problem. However, from the point of view of correlation effects GGA is still better because HF does not include dynamic correlations.

C

APPENDIX C

Theory of transport in disordered graphene

We describe the calculation method for a graphene samples with length, L , and width $W \gg L$ (see Fig. 3.8). It is again important to mention the collaboration with P. Ostrovsky, who contributed with the analytical model that we present in this section. Here we will present an outline of the transport theory that has been developed in the Ref. [137] using full counting statistics for arbitrary number of resonant impurities, N .

C.1 Model and Method

In graphene the low energy physics is described by the Dirac Hamiltonian,

$$H = -i\hbar v_F \boldsymbol{\sigma} \cdot \vec{\nabla} + V(\mathbf{r}) \quad (\text{C.1})$$

where $V(\mathbf{r})$ is the impurity potential and $\boldsymbol{\sigma} = \{\sigma_x, \sigma_y\}$ is the vector of Pauli matrices. In transport calculation we also assume that the chemical potential of a graphene sample ($0 < x < L$) is tuned to the Dirac point, while the two attached metallic leads have chemical potential $\mu \rightarrow \infty$.

The cumulant generating function for charge transport is defined as an operator trace of the Green's function in the Keldysh space,

$$\mathcal{F} = \text{Tr} \ln \mathcal{G}^{-1} \quad (\text{C.2})$$

where \mathcal{G} is the Green's function in Keldysh space and the trace (Tr) is over the spatial coordinates as well as the valley and RA indices. Observable, such as conductance, noise, are easily derived from the generating function, \mathcal{F} . For

instance, the conductance (G) is given by the second derivative of the generating function with respect to the counting fields,

$$G = -\frac{4e^2}{h} \frac{\partial^2 \mathcal{F}}{\partial \phi^2} \Big|_{\phi=0} \quad (\text{C.3})$$

where ϕ is the counting field. The factor 4 in the above expression accounts for valley and spin degeneracy. To calculate the Green's function for \mathcal{F} we use the matrix Green's function representation in the retarded-advance (RA) space [177–180]. With the help of the Dyson equation the Green's function is given in the standard operator notation as,

$$(\mathcal{G}_0^{-1} - V) \mathcal{G} = \mathbb{1}. \quad (\text{C.4})$$

where, \mathcal{G}_0 is the Green's function of the clean system, which depends on the counting field and satisfy the necessary boundary conditions. Now using the standard definition of the Green's function as described in the Dyson equation, Eq. (C.4), the full counting generating function, Eq. (C.2), can be written as a sum of two terms: $\mathcal{F} = \mathcal{F}_0 + \delta\mathcal{F}$, where $\mathcal{F}_0 = \mathbf{Tr} \ln \mathcal{G}_0^{-1}$ with,

$$\delta\mathcal{F} = \mathbf{Tr} \ln(1 - V\mathcal{G}_0) \quad (\text{C.5})$$

where, $\delta\mathcal{F}$ describes the correction to the cumulant generating function in the presence of impurities. At this point we assume that impurities do not overlap as the size of impurities is much smaller than the distance between impurities and Fermi wavelength and also the operator determinant in the definition of $\delta\mathcal{F}$ reduces to usual matrix determinant form. The generating function is then re-written in the N -dimensional impurity space (unfolded space) as,

$$\delta\mathcal{F} = \mathbf{Tr} \ln(1 - V\mathcal{G}_0) \equiv \mathbf{Tr} \ln(1 - \hat{V}\hat{\mathcal{G}}_0) \quad (\text{C.6})$$

where, $\hat{V} = \text{diag}\{V_1, V_2, \dots, V_N\}$ and all the elements of \mathcal{G}_0 is equal to $\hat{\mathcal{G}}_0$. Now in this representation $\hat{\mathcal{G}}_0$ is a $N \times N$ matrix in the impurity space. The above equation can be solved by introducing the usual T -matrix in the Dyson equation, Eq. (C.4),

$$\hat{\mathcal{G}} = \hat{\mathcal{G}}_0 + \hat{\mathcal{G}}_0 \hat{T}_0 \hat{\mathcal{G}}_0; \quad \text{with, } \hat{T}_0 = \frac{1}{1 - \hat{V}\hat{\mathcal{G}}_0} \hat{V} \quad (\text{C.7})$$

Now, notice that the diagonal part of the matrix $\hat{\mathcal{G}}_0$ has diverging contribution which need to be properly regularized. The matrix, \hat{g} , which is the diverging part and is given by the bare Green's function of an infinite graphene plane, is diagonal in impurity space and depends neither on the counting field nor on the boundary condition,

$$\hat{\mathcal{G}}_0 = \hat{g} + \hat{\mathcal{G}}_{\text{reg}} \quad (\text{C.8})$$

with,

$$g(\mathbf{r}) = -\frac{i}{2\pi} \frac{\boldsymbol{\sigma} \cdot \mathbf{r}}{r^2} \quad (\text{C.9})$$

Using the above definition of Green's function and T -matrix the correction in the cumulant generating function can be expressed as a sum of two terms in a standard matrix product form,

$$\delta\mathcal{F} = \mathbf{Tr} \ln[1 - \hat{\mathcal{T}}\hat{\mathcal{G}}_{\text{reg}}] + \mathbf{Tr} \ln[1 - \hat{V}\hat{g}] \quad (\text{C.10})$$

where, $\hat{\mathcal{T}} = \text{diag}\{T_1, T_2, \dots, T_N\}$ with, $T_n = (1 - V_n g)^{-1} V_n$. The last term in the above expression is independent of the counting field; consequently, we can safely ignore the term from the cumulant generating function as it makes no contribution to the observable, Eq. (C.3). The matrix elements of the regularized Green's function is given by,

$$(\mathcal{G}_{\text{reg}})_{nm} = \begin{cases} \mathcal{G}_0(\mathbf{r}_m, \mathbf{r}_n) & m \neq n \\ \lim_{\mathbf{r} \rightarrow \mathbf{r}_n} [\mathcal{G}_0(\mathbf{r}_n, \mathbf{r}) - g(\mathbf{r}_n - \mathbf{r})] & m = n \end{cases} \quad (\text{C.11})$$

where, $\mathbf{r}_n = (x_n, y_n)$ defines the position of an impurity.

At this stage, the problem of impurity induced correction to the conductivity reduces to a calculation of the matrix determinant of a finite size matrix of a dimension given by the number of impurities in the sample. In Eq. (C.10) the bare Green's function, \mathcal{G}_0 , is obtained by solving analytically the matrix Green's function method in the RA space with $V = 0$ in Eq. (C.1),

$$\begin{pmatrix} \mu - H + i0 & -i\sigma_x \sinh\left(\frac{\phi}{2}\right) \delta(x) \\ -i\sigma_x \sinh\left(\frac{\phi}{2}\right) \delta(x - L) & \mu - H - i0 \end{pmatrix} \mathcal{G}_0(\mathbf{r}, \mathbf{r}') = \delta(\mathbf{r} - \mathbf{r}') \quad (\text{C.12})$$

where, in leads $\mu \rightarrow \infty$ and in the sample $\mu = 0$. The only remaining part to solve of the general result, Eq. (C.10), are the \mathcal{T} -matrices of individual impurities (see Ref. [137] and refs therein). This is, for instance, obtained by solving the single impurity problem. The resulting generating function then can be recast in the following concise form,

$$\mathcal{F}(\phi) = -\frac{W\phi^2}{2\pi L} + \ln \det M(\phi) + \ln \det M(-\phi) \quad (\text{C.13})$$

where, $M = \{M_{i,j}\}$ is a $N \times N$ matrix with elements,

$$M_{ij}(\phi) = \frac{\exp\left[\frac{\phi}{2L}(y_i - y_j)\right]}{\sin\left[\frac{\pi}{2L}(z_i x_i + z_j x_j + i y_i - i y_j)\right]} + z_i z_j \frac{\exp\left[\frac{\phi}{2L}(y_j - y_i)\right]}{\sin\left[\frac{\pi}{2L}(z_i x_i + z_j x_j + i y_j - i y_i)\right]} \quad (\text{C.14})$$

where, N is the number of impurities (vacancies) at positions (x_i, y_i) . The variable $z_i = \pm 1$ denotes the position of vacancies in sub-lattice A or B. This general expression allow us to calculate observable quantities for any given number of

vacancies with its position. For instance, the conductance is expressed as,

$$G = -\frac{4e^2}{h} \left. \frac{\partial^2 \mathcal{F}}{\partial \phi^2} \right|_{\phi=0} = \frac{4e^2 W}{\pi h L} + \frac{8e^2}{h} \text{tr} \left[(\dot{M} M^{-1})^2 - \ddot{M} M^{-1} \right]_{\phi=0} \quad (\text{C.15})$$

where, \dot{M} , \ddot{M} are first and second derivative of M with respect to ϕ . The main calculation task is to invert a matrix $M(\phi = 0)$, which has a dimension of the number of impurities in the sample.

D

APPENDIX D

Calculation of the dephasing rate

We describe our analytical model with an outline of the calculation for the dephasing rate, τ_ϕ , at criticality. In the following analysis we consider a specific situation when the time-reversal invariance of the system is fully broken due to presence of a strong magnetic field. This particular problem belongs to the conventional unitary symmetry class. Along with time-reversal invariance we also assume that due to strong magnetic field the spin-rotational invariance is also broken, such that the system is fully spin polarized. The situation arises naturally in the experiments in the presence of magnetic impurities or in the presence of strong spin-orbit coupling. It is again important to emphasize the fact that this part of the discussion is largely based on Ref. [143] and the analytical model with its solution is provided by I. Burmistrov.

D.1 Model Hamiltonian

We consider a model Hamiltonian for disordered interacting two-dimensional electronic system,

$$\mathcal{H} = \mathcal{H}_0 + \mathcal{H}_{\text{int}}, \quad (\text{D.1})$$

where, \mathcal{H}_0 is the non-interacting single particle term that contains the disorder potential, $V_{\text{dis}}(\mathbf{r})$, and is given by,

$$\mathcal{H}_0 = \int d\mathbf{r} \Psi^\dagger(\mathbf{r}) \left[\frac{1}{2m} (-i\nabla - \mathcal{A}(\mathbf{r}))^2 + V_{\text{dis}}(\mathbf{r}) \right] \Psi(\mathbf{r}), \quad (\text{D.2})$$

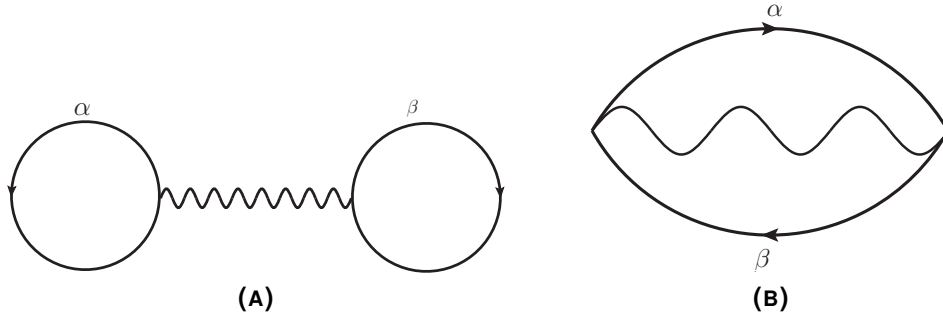


FIGURE D.1: (A) Hartree correction to the thermodynamic potential. The wavy line denotes the interaction and the solid lines represent the single particle propagator (Green's function). (B) Feynman diagram for the Fock correction, where α, β are the energy index.

where $\mathcal{A}(\mathbf{r})$ is the vector potential, which is defined as $\vec{B} = \nabla_{\mathbf{r}} \times \mathcal{A}(\mathbf{r})$. The Hamiltonian, Eq. (D.2), describes a system with broken time reversal symmetry that belongs to the unitary symmetry class, A. Due to broken spin-rotational invariance, here we consider spinless electrons for the rest of the derivation. The interaction part of the Hamiltonian is given by,

$$\mathcal{H}_{\text{int}} = \frac{1}{2} \int d\mathbf{r}_1 d\mathbf{r}_2 \Psi^\dagger(\mathbf{r}_1) \Psi^\dagger(\mathbf{r}_2) U(\mathbf{r}_1 - \mathbf{r}_2) \Psi(\mathbf{r}_2) \Psi(\mathbf{r}_1), \quad (\text{D.3})$$

where $U(\mathbf{r}_1 - \mathbf{r}_2)$ is the short-range interaction potential with $\Psi(\mathbf{r})$ being the single particle non-interacting wavefunction.

D.2 First order correction to the thermodynamic potential

Here we study the correction due to interaction to the thermodynamic potential, Ω , by doing a perturbation theory in the interaction near the non-interacting fixed point. The first order diagrams that contribute in the correction to the thermodynamic potential are shown in Fig. D.1. By following the same consideration of Ref. [155], the first order (Hartree-Fock) contribution to the thermodynamic potential has the form,

$$\Omega^{(1)} = \frac{1}{2} \sum_{\alpha, \beta} n_f(\epsilon_\alpha) n_f(\epsilon_\beta) \int d\mathbf{r}_1 d\mathbf{r}_2 U(\mathbf{r}_1 - \mathbf{r}_2) |\mathcal{M}_{\alpha, \beta}(\mathbf{r}_1, \mathbf{r}_2)|^2, \quad (\text{D.4})$$

where $n_f(\epsilon_{\alpha, \beta})$ is the Fermi-Dirac distribution function. $\mathcal{M}_{\alpha, \beta}(\mathbf{r}_1, \mathbf{r}_2)$ is the matrix elements of the exact single particle wavefunctions, $\phi_\alpha(\mathbf{r})$ with eigen energy ϵ_α ,

$$\mathcal{M}_{\alpha, \beta}(\mathbf{r}_1, \mathbf{r}_2) = \phi_\alpha(\mathbf{r}_1) \phi_\beta(\mathbf{r}_2) - \phi_\alpha(\mathbf{r}_2) \phi_\beta(\mathbf{r}_1). \quad (\text{D.5})$$

After disorder averaging of Eq. (D.4), the average contribution to the thermodynamic potential is given by,

$$\langle \Omega^{(1)} \rangle = \int \frac{dE d\omega}{\Delta^2} n_f(E) n_f(E + \omega) \int d\mathbf{r}_1 d\mathbf{r}_2 \mathcal{K}_1(\mathbf{r}_1, \mathbf{r}_2, E, \omega), \quad (\text{D.6})$$

where $\Delta = 1/(\varrho_d L^d)$ is the mean level spacing, ϱ_d is the density of states, and L is the system size in d dimension. The angular brackets $\langle \rangle$ denotes the disorder averaging. The function \mathcal{K}_1 can be calculated by comparing Eq. (D.4) and Eq. (D.6),

$$\mathcal{K}_1(\mathbf{r}_1, \mathbf{r}_2, E, \omega) = \frac{\Delta^2}{2} \sum_{\alpha, \beta} \langle |\mathcal{M}_{\alpha, \beta}(\mathbf{r}_1, \mathbf{r}_2)|^2 \delta(E + \omega - \epsilon_\alpha) \delta(E - \epsilon_\beta) \rangle. \quad (\text{D.7})$$

\mathcal{K}_1 describes the correlation between two eigenstates ($\phi_\alpha(\mathbf{r})$) of the non-interacting Hamiltonian, Eq. (D.2). In the limit, $L \rightarrow \infty$ the correlation function, \mathcal{K}_1 exhibits the following scaling behavior,

$$\mathcal{K}_1(\mathbf{r}_1, \mathbf{r}_2, E, \omega) = L^{-2d} \left(\frac{|\mathbf{r}_1 - \mathbf{r}_2|}{L_\omega} \right)^{\mu_2} \tilde{\mathcal{K}}_1 \left(\frac{|\mathbf{r}_1 - \mathbf{r}_2|}{L_\omega} \right), \quad (\text{D.8})$$

where,

$$\tilde{\mathcal{K}}_1(x) = \begin{cases} 1, & x \ll 1 \\ x^{-\mu_2}, & x \gg 1, \end{cases} \quad (\text{D.9})$$

with $L_\omega = L(\Delta/|\omega|)^{1/d}$ being the length scale due to frequency and μ_2 is the scaling exponent. We are mostly interested in the energies close to each other such that, $\omega \sim \Delta$ and $L_\omega \sim L$. It is important to note at this point that due to anti-symmetrized wavefunction (Hartree-Fock), Eq. (D.5), the exponent μ_2 is positive $\mu_2 > 0$. At criticality it reflects that at shorter distances, $|\mathbf{r}_1 - \mathbf{r}_2| \ll L_\omega$, the correlation function is suppressed compared to metallic system. One of the main goal in this work is to calculate the exponent μ_2 at the IQH critical point.

To complete the analysis, we assume the electron-electron interaction of the following form,

$$U(\mathbf{R}) = u_0 \left(1 + \left(\frac{\mathbf{R}}{a} \right)^2 \right)^{-\lambda/2} \quad (\text{D.10})$$

with $\lambda > d$, and a being the lattice constant. Using the above definition of interaction, $U(\mathbf{R})$, in Eq. (D.6) and performing the spatial integration one finds,

$$\langle \Omega^{(1)} \rangle \propto \int \frac{dE d\omega}{\Delta} n_f(E) n_f(E + \omega) \mathcal{U}(L_\omega) \quad (\text{D.11})$$

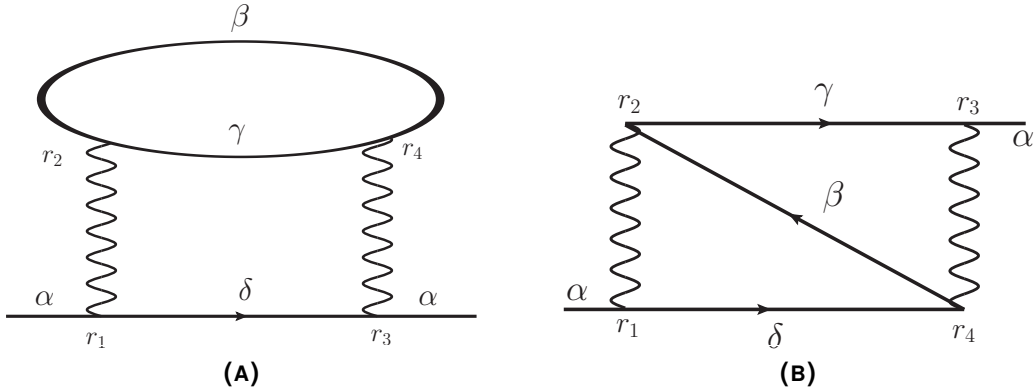


FIGURE D.2: (A) Second order Feynman diagrams that contribute in the self-energy.

where

$$\mathcal{U}(L_\omega) = \varrho_d u_0 a^d \begin{cases} (a/L_\omega)^{\mu_2}, & d + \mu_2 < \lambda, \\ (a/L_\omega)^{\mu_2} \ln \frac{L_\omega}{a}, & \lambda = d + \mu_2, \\ (a/L_\omega)^{\lambda-d}, & d < \lambda < d + \mu_2. \end{cases} \quad (\text{D.12})$$

where $\mathcal{U}(L_\omega)$ is the renormalized interaction parameter. For short ranged electron-electron interaction, $\lambda > d$, the interaction becomes irrelevant near non-interacting fixed point, $\mathcal{U} = 0$; thus the sub-leading terms, μ_2 , govern the interaction corrections and the *leading* multifractal powerlaws cancel. We will elaborate on this aspect further in our numerical analysis section.

D.3 Second order correction to the self-energy: Dephasing rate

We consider the second order correction in the interaction to calculate the dephasing rate, τ_ϕ , which is determined by the imaginary part of the self-energy (see Fig. D.2). We define the self-energy by following Ref. [181] of a single particle state with energy, ϵ_α , as,

$$\begin{aligned} \Sigma_\alpha^R(\epsilon) &= \frac{1}{8} \int d\mathbf{r}_1 d\mathbf{r}_2 d\mathbf{r}_3 d\mathbf{r}_4 U(\mathbf{r}_1 - \mathbf{r}_2) U(\mathbf{r}_3 - \mathbf{r}_4) \mathcal{M}_{\alpha\beta}^*(\mathbf{r}_1, \mathbf{r}_2) \mathcal{M}_{\delta\gamma}(\mathbf{r}_1, \mathbf{r}_2) \\ &\times \mathcal{M}_{\gamma\delta}^*(\mathbf{r}_3, \mathbf{r}_4) \mathcal{M}_{\beta\alpha}(\mathbf{r}_3, \mathbf{r}_4) \sum_{\beta\gamma\delta} \frac{n_f(\epsilon_\beta)[1 - n_f(\epsilon_\gamma)] + n_f(\epsilon_\delta)[n_f(\epsilon_\gamma) - n_f(\epsilon_\beta)]}{\epsilon + \epsilon_\beta - \epsilon_\gamma - \epsilon_\delta + i0}. \end{aligned} \quad (\text{D.13})$$

where $\mathcal{M}_{\alpha\beta}(\mathbf{r}_1, \mathbf{r}_2)$ is given by Eq. D.5. Next, we perform the disorder averaging

of the self-energy,

$$\Sigma^R(E, \epsilon) = \Delta \left\langle \sum_{\alpha} \Sigma_{\alpha}^R(\epsilon) \delta(E - \epsilon_{\alpha}) \right\rangle. \quad (\text{D.14})$$

In order to perform the disorder averaging at the criticality we exploit the fact that in this situation dephasing rate, τ_{ϕ} , is a self-averaging quantity unlike in the localized phase, where the level spacing becomes larger than the averaged dephasing rate. Consequently, in localized phase the Golden rule approximation, where states are treated essentially as a continuum, breaks down. The result of the above averaging procedure can be presented in the following form:

$$\begin{aligned} \text{Im}\Sigma^R(E, \epsilon) = & -\pi \left(\prod_{j=1}^4 \int d\mathbf{r}_j \right) U(\mathbf{r}_1 - \mathbf{r}_2) U(\mathbf{r}_3 - \mathbf{r}_4) \int \frac{d\Omega d\epsilon'}{\Delta^3} \{n_f(\epsilon' + \Omega) \\ & \times [1 - n_f(\epsilon')] + [n_f(\epsilon') - n_f(\epsilon' + \Omega)] n_f(\epsilon + \Omega)\} \mathcal{K}_2(\{\mathbf{r}_j\}, E, \epsilon, \epsilon', \Omega). \end{aligned} \quad (\text{D.15})$$

where the correlation function, $\mathcal{K}_2(\{\mathbf{r}_j\}, E, \epsilon, \epsilon', \Omega)$, is given by,

$$\begin{aligned} \mathcal{K}_2(\{\mathbf{r}_j\}, E, \epsilon, \epsilon', \Omega) = & \frac{\Delta^4}{8} \left\langle \sum_{\alpha\beta\gamma\delta} \mathcal{M}_{\alpha\beta}^*(\mathbf{r}_1, \mathbf{r}_2) \mathcal{M}_{\delta\gamma}(\mathbf{r}_1, \mathbf{r}_2) \mathcal{M}_{\gamma\delta}^*(\mathbf{r}_3, \mathbf{r}_4) \mathcal{M}_{\beta\alpha}(\mathbf{r}_3, \mathbf{r}_4) \right. \\ & \times \delta(E - \epsilon_{\alpha}) \delta(\epsilon' + \Omega - \epsilon_{\beta}) \delta(\epsilon' - \epsilon_{\gamma}) \delta(\epsilon + \Omega - \epsilon_{\delta}) \left. \right\rangle \end{aligned} \quad (\text{D.16})$$

To perform the integration we need to set the characteristic energy scales in the problem. First, we are interested in dephasing rate at the mass shell, $E = \epsilon$, and at $\epsilon \sim T$. As we are mostly after the scaling behavior of the dephasing rate and not attempting to calculate the numerical pre-factor of order unity, we set the temperature to be zero. Next, all the other integral variables (ϵ', Ω) are also set by the temperature. After the energy integration Eq. D.15 becomes,

$$\begin{aligned} \text{Im}\Sigma^R(0, 0) = & -\frac{1}{2\Delta^3} \left(\prod_{j=1}^4 \int d\mathbf{r}_j \right) U(\mathbf{r}_1 - \mathbf{r}_2) U(\mathbf{r}_3 - \mathbf{r}_4) \int d\Omega \\ & \times \left(\coth \frac{\Omega}{2T} - \tanh \frac{\Omega}{2T} \right) \mathcal{K}_2(\{\mathbf{r}_j\}, 0, 0, \epsilon' \sim T, \Omega) \end{aligned} \quad (\text{D.17})$$

The scaling behavior of the correlation function, \mathcal{K}_2 is given in Ref. [155],

$$\mathcal{K}_2(\{\mathbf{r}_j\}, 0, 0, \epsilon' \sim T, \Omega) = L^{-4d} \left(\frac{|\mathbf{r}_1 - \mathbf{r}_2| |\mathbf{r}_3 - \mathbf{r}_4|}{R} \right)^{\mu_2} \left(\frac{R}{L_{\Omega}} \right)^{\alpha} \quad (\text{D.18})$$

where $R = (\mathbf{r}_1 + \mathbf{r}_2 - \mathbf{r}_3 - \mathbf{r}_4)/2$. The above scaling form of the correlation function, \mathcal{K}_2 , is valid in the range $|\mathbf{r}_1 - \mathbf{r}_2|, |\mathbf{r}_3 - \mathbf{r}_4| \ll R \ll L_{\Omega}$ with the assumption that

$\varepsilon' \sim \Omega$, as both the energies are of the order of temperature, T . In the limit of large distance, $R \sim L_\Omega$, the correlation between wavefunctions at the points $\mathbf{r}_{1,2}$ and at the points $\mathbf{r}_{3,4}$ decouple. It is now easy to see that in this limit the function \mathcal{K}_2 reduces to a product of two independent scaling functions given by the correlation function \mathcal{K}_1 , i.e. $(|\mathbf{r}_1 - \mathbf{r}_2|/R)^{\mu_2}(|\mathbf{r}_3 - \mathbf{r}_4|/R)^{\mu_2}$. One of the main numerical tasks in this work is to calculate the exponent, α , which describes the scaling with respect to the variable R/L_Ω .

Combining Eq. (D.17) and Eq. (D.18), we obtain,

$$|\text{Im}\Sigma^R(0,0)| = \varrho_d T \int_0^T d\Omega \int_a^{L_\Omega} d\mathbf{R} \mathcal{U}^2(R) \left(\frac{R}{L_\Omega}\right)^\alpha \quad (\text{D.19})$$

The above integration over \mathbf{R} depends on the relation between α, μ_2, λ and d . For the calculation of the dephasing rate we first assume a scenario, where $\alpha > -d$. Then, if $\lambda > d + \mu_2$; the dephasing rate is given by,

$$-\text{Im}\Sigma^R(0,0) \sim \frac{1}{\tau_\phi} \propto \delta \mathcal{U}^2(a) \begin{cases} (T/\delta)^{1+2\mu_2/d}, & d - 2\mu_2 + \alpha > 0, \\ (T/\delta)^{1+2\mu_2/d} \ln(\delta/T), & d - 2\mu_2 + \alpha = 0, \\ (T/\delta)^{2+\alpha/d}, & d - 2\mu_2 + \alpha < 0. \end{cases} \quad (\text{D.20})$$

In the situation $\lambda = d + \mu_2$, Eq. (D.19) reduces to,

$$\frac{1}{\tau_\phi} \propto \delta \mathcal{U}^2(a) \times \begin{cases} (T/\delta)^{1+2\mu_2/d} \ln^2(\delta/T), & d - 2\mu_2 + \alpha > 0, \\ (T/\delta)^{1+2\mu_2/d} \ln^3(\delta/T), & d - 2\mu_2 + \alpha = 0, \\ (T/\delta)^{2+\alpha/d}, & d - 2\mu_2 + \alpha < 0. \end{cases} \quad (\text{D.21})$$

Similarly, in the limit $\lambda < d + \mu_2$ one finds,

$$\frac{1}{\tau_\phi} \propto \delta \mathcal{U}^2(a) \times \begin{cases} (T/\delta)^{-1+2\lambda/d}, & 3d - 2\lambda + \alpha > 0, \\ (T/\delta)^{-1+2\lambda/d} \ln(\delta/T), & 3d - 2\lambda + \alpha = 0, \\ (T/\delta)^{2+\alpha/d}, & 3d - 2\lambda + \alpha < 0. \end{cases} \quad (\text{D.22})$$

where $\delta = 1/\varrho_d a^d$ is the ultraviolet energy cutoff. Now it is readily seen that the temperature dependence of the dephasing rate, τ_ϕ , depends on the exponents μ_2, α , dimensionality d , and the index λ that characterizes the decay of the electron-electron interaction. Here, the exponents μ_2 and α characterize the correlation of the multifractal wavefunctions at the criticality. In this work we will numerically calculate those exponents at the IQH critical point in two-dimension.

E

APPENDIX E

Numerical implementation of the network model

In this section we discuss the numerical implementation of the network model that has been used to calculate the sub-leading multifractal exponent and the exponent κ as described in Chapter 4. The discussion is largely based on Ref. [154].

We have developed a “highly optimized” numerical implementation of the Chalker-Coddington network model (CCNM) with intensive use of sparse matrix libraries ARPACK and MUMPS for diagonalization and solving linear equations. In particular, we have performed a detailed profiling of the serial code and subsequently employed multilevel hybrid (shared memory and distributed memory) strategies for parallelization. The dimension of the matrices computed is of the order of 10 million x 10 million and 10^6 disorder realizations have been done, which is particularly important to observe the true scaling behavior of the correlation functions, Eq. (4.2), Eq. (4.5).

E.1 Parallelization procedure

The CCNM described in the Section 4.3.2 has been implemented in Fortran 90. In order to efficiently tackle numerics with sparse matrices the program makes intensive use of high performance libraries ARPACK and MUMPS. In particular, the Implicitly Restarted Arnoldi Iteration from the ARPACK package [182] was employed to compute approximations to eigenvalues from Eq. (4.14). Typically 6 to 8 eigenvalues close to zero energy are computed in order to calculate the correlation functions. In order to diagonalize iteratively in the ARPACK one needs to provide another routine to solve a system of linear equation. For this purpose we

use the Multi-frontal Massively Parallel sparse direct Solver (MUMPS) [183–185] and PORC reordering [186].

At first we perform numerous optimizations to improve the serial performance of the code and to identify and to reduce the number of bottlenecks. Reducing the number of bottlenecks is important for efficient parallelization of the overall code with minor programming and tuning effort due to the law of diminishing returns. It turns out that for all models (first-order correction (Eq. (4.2)), second-order correction (Eq. (4.5))) the call to the linear solver (here MUMPS library) was the most expensive part. For instance, our time measurements shows that the linear solver MUMPS take 65-70% of the total runtime of the entire code. The rest of the time is used by several other parts of the code. For example the driver subroutine including the calls to MUMPS and the subroutine defining the network operator (U) take together up to 15%, and in the second-order correction model the subroutine, that calculates the correlation function as defined in Eq. (4.5), takes up to 15% of the run time for a specific choice of the system size L .

In the next subsections we describe our strategies to parallelization.

E.1.1 Parallelization of the disorder averaging

With our naive implementation of the model the calculation time for a reasonable system size with $10^4 - 10^6$ disorder realizations takes time of the order of few months. This is why we first considered parallelization of the disorder averaging. We implemented it using reduction global communications of MPI such as `mpi_reduce`. In this way, for instance, a single job can be finished within a week, which is bounded by a specific cluster runtime. Even if a job is not finished within a week time we have implemented an additional means to checkpoint the calculation and to continue later in a new job restarting from the last checkpoint.

E.1.2 Parallelization of the linear solver

The two major advantages to perform parallelization at this level are memory reduction per task and the work-load distribution (speedup) over the available processors. The MUMPS library is parallelized with use of MPI and basing on asynchronous static and dynamic scheduling algorithms. Moderate speedups of 14 on 32 processors [183] have been reported. Nearly linear scaling for up to 4 tasks and speedup of 6 on 8 tasks have been reported for the most recent version of MUMPS [187]. Noticeably, the parallel performance reported strongly varies with the size and type of the left-hand-side matrix [188, 189].

Additionally we have compiled our code using the Intel Fortran compiler version 11. For the parallel version of the code the Intel MPI library was used on the

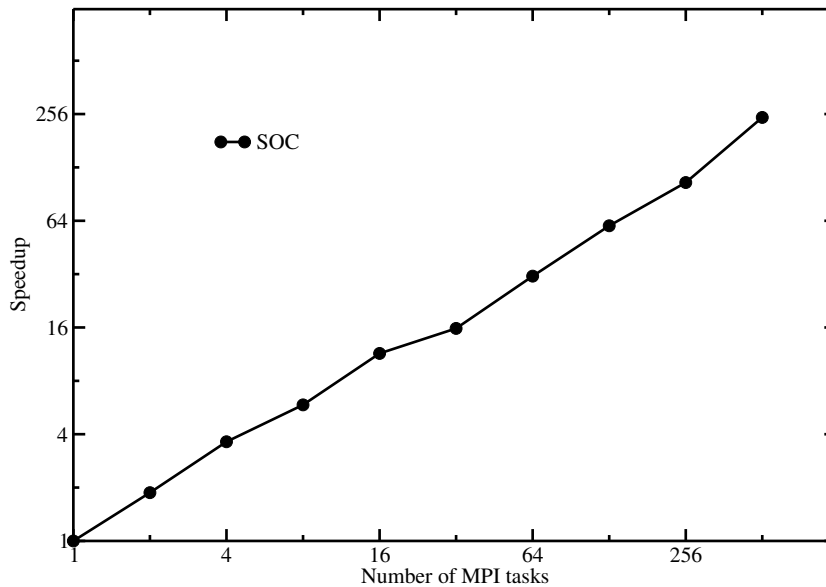


FIGURE E.1: Speedup of parallel disorder averaging for the second-order scaling function with $L = 512$ links in one direction denoted by circles. Figure courtesy: I. Kondov.

Opus cluster and HP-MPI library on the XC 3000 (HC3). For LAPACK, BLAS, BLACS and ScaLAPACK that are needed by MUMPS and ARPACK the Intel Math Kernel Library version 10 was linked. For profiling and debugging purposes gprof and DDT, respectively, were used.

E.1.3 Simulation protocol and parameters

We started our runs on the systems Opus (IBM x3550 with Intel Xeon E5430 processors and DDR InfiniBand interconnect) and the HC3 (HP XC3000 with Intel Xeon E5540 processors and QDR InfiniBand interconnect) at the Steinbuch Centre for Computing (SCC). The system size, L , is defined in terms of number of links in one direction of the square lattice which was varied from 128 up to 2048 links in one direction of the CCNM model. For calculating the second-order correction (see Eq. (4.5)) we choose the following combination of spatial distances to calculate the correlation function, \mathcal{K}_2 , $\mathbf{r}_1 - \mathbf{r}_2 = \mathbf{r}_3 - \mathbf{r}_4 = 1$ and $\mathbf{r}_1 - \mathbf{r}_3 = 3$.

E.2 Computational performance

Parallelization of the disorder averaging is coarse grained it is widely latency insensitive. In addition, it requires exchange of very small messages and the communication times do not depend on the interconnects bandwidth. Thus, the paralleliza-

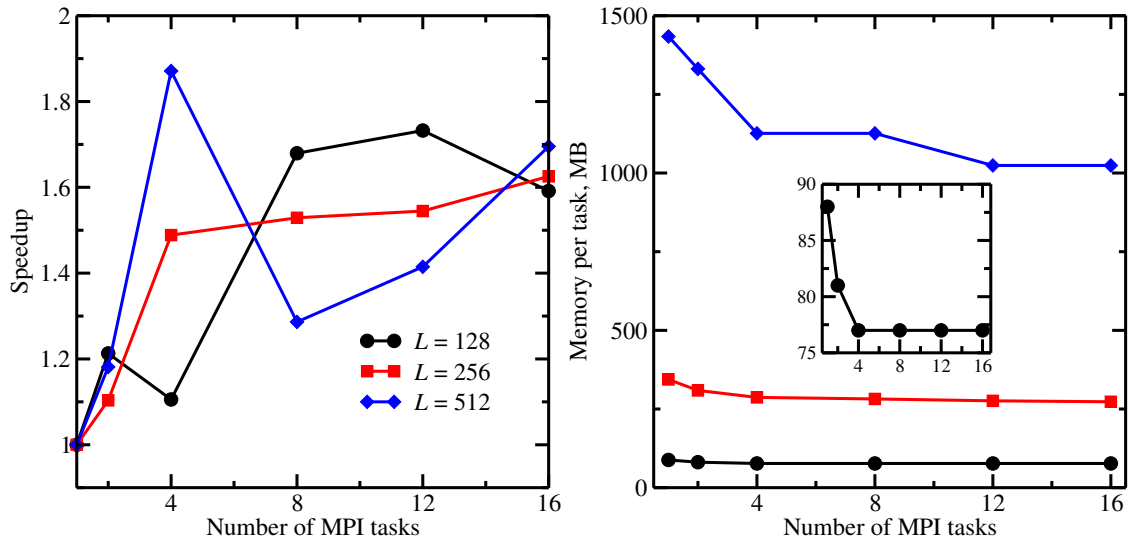


FIGURE E.2: Speedup (left plot) and memory usage per task (right plot) for the second-order scaling with parallelized linear solver (MUMPS). Measured data for $L = 128$, 256 and 512 links are denoted by black circles, red squares and blue diamonds, respectively. Figure courtesy: I. Kondov.

tion of the disorder averaging scales very well for very high MPI task number as shown on Fig. E.1. Due to the widely dominating parallel section for the sampling tasks ($> 99.99\%$ for models with $L = 512$ links) the speedup is nearly linear for up to 512 MPI tasks. However, the observed slope is notably smaller than that of the ideal speedup. As introduced in the methods section, we have implemented a synchronous algorithm to parallelize disorder averaging. Because each disorder realization takes slightly different time due to iterative solver this leads to load imbalance which gives rise to overall smaller slope of the speedup. We have analyzed the measured time profiles of all parallel sections and arrived to approx. 13% average load imbalance as determined as the ratio of the standard deviation and the mean of parallel section times for second-order correction. Moreover, we identified load imbalance peaks (from the ratio of the mean and the maximum of parallel section times) amounting to approx. 47% for the second-order scaling.

Besides parallelization of disorder averaging we also exploited parallelism available in the linear solver library MUMPS. As noted previously, parallelization of this kind is already known to scale only moderately [188, 189], however, the possibility to distribute data, which scales like L^4 , enables carrying out computations for $L > 2000$ links which is otherwise limited by the memory available on the compute node for one MPI task. As a benchmark we show on Fig. E.2 the measured speedup and memory decrease per task. For two and four tasks an initial increase in the speedup is observed. Then the speedups for $L = 128$ and $L = 256$ links additionally increase while the speedup for the models with $L = 512$ links drops somewhat with 8 MPI tasks. The best speedup found for the second-order scaling model is 1.9. The speedup for both 128-link models is decreasing going past 16

MPI tasks while the gain for the 512-link models is non-significant. Note that the speedup only due to calls to MUMPS has been discussed. The code parts that do not belong to the linear solver, amounting to 35%, are not considered.

On the right panel of Figs. E.2 we plot the reduction of memory usage per task with the degree of parallelization. Largest decrease of a factor of two is found for the PCC model for all network sizes. For all sizes the memory usage decreases monotonously with task number. However, no further gain was measured for number of tasks larger than 16. To summarize, the linear solver as available in the MUMPS library can perform only moderately in parallel utilizing efficiently up to 2-4 MPI tasks. Additional speedup improvement may be achieved using threaded BLAS calls as has been reported in Ref. [187] with up to 4 threads per task. Furthermore, the data distribution can be optimized using another partitioning algorithm [190]. Also in this case a trade-off between performance gain and resource utilization has to be made with up to 16 tasks.

E.3 Summary and Outlook

We have showed an efficient parallel implementation of the Chalker-Coddington network model. Currently, the code can be efficiently used on massively parallel computers, like the HC3 at SCC, to solve and average solutions over disorder within a single day. For matrices for network size of $L \approx 1000 - 2000$ an improved parallelization of the linear solver can yield additional speedup and, at certain extent, to manage the existing memory bottleneck per task.

In current and future work we consider using ParMETIS [190, 191] or PT-SCOTCH [192] for factorization/reordering to improve the scaling in terms of speedup and memory usage per core. In addition, using multi-threaded BLAS on 2-4 threads can improve the speedup considerably. In order to minimize and eliminate load imbalance due to parallelization of disorder sampling, an asynchronous scheduling algorithm is currently being implemented. Another optimization aspect is the reduction of code parts not belonging to the linear solver via serial optimization.

Bibliography

- [1] K. S. Novoselov, A. K. Geim, S. V. Morozov, D. Jiang, Y. Zhang, S. V. Dubonos, I. V. Grigorieva, and A. A. Firsov. Electric Field Effect in Atomically Thin Carbon Films. *Science*, 306(5696):666–669, 2004.
- [2] C. W. J. Beenakker. Colloquium: Andreev reflection and Klein tunneling in graphene. *Rev. Mod. Phys.*, 80(4):1337–1354, Oct 2008.
- [3] A. H. Castro Neto, F. Guinea, N. M. R. Peres, K. S. Novoselov, and A. K. Geim. The electronic properties of graphene. *Rev. Mod. Phys.*, 81(1):109–162, Jan 2009.
- [4] A. K. Geim and K. S. Novoselov. The rise of graphene. *Nat. Mat.*, 6(3):183–191, Mar 2007.
- [5] K. S. Novoselov, D. Jiang, F. Schedin, T. J. Booth, V. V. Khotkevich, S. V. Morozov, and A. K. Geim. Two-dimensional atomic crystals. *Proc. Natl. Acad. Sci. U.S.A.*, 102(30):10451–10453, 2005.
- [6] N. M. R. Peres. Colloquium: The transport properties of graphene: An introduction. *Rev. Mod. Phys.*, 82(3):2673–2700, Sep 2010.
- [7] W. Bao, F. Miao, Z. Chen, H. Zhang, W. Jang, C. Dames, and C. N. Lau. Ripple texturing of suspended graphene atomic membranes. *Nat. Nano.*, 4:562, 2009.
- [8] J. C. Meyer, A. K. Geim, M. I. Katsnelson, K. S. Novoselov, T. J. Booth, and S. Roth. The structure of suspended graphene sheets. *Nature*, 446(7131):60–63, Mar 2007.
- [9] E. Stolyarova, K.T. Rim, S. Ryu, J. Maultzsch, P. Kim, L.E. Brus, T.F. Heinz, M.S. Hybertsen, and G.W. Flynn. High-resolution scanning tunneling microscopy imaging of mesoscopic graphene sheets on an insulating surface. *Proc. Natl. Acad. Sci.*, 104(22):9209–9212, 2007.
- [10] M. Farjam and H. Rafii-Tabar. Comment on “band structure engineering of graphene by strain: First-principles calculations”. *Phys. Rev. B*, 80(16):167401, Oct 2009.
- [11] G. Cocco, E. Cadelano, and L. Colombo. Gap opening in graphene by shear strain. *Phys. Rev. B*, 81(24):241412, Jun 2010.

- [12] A. Hashimoto, K. Suenaga, A. Gloter, K. Urita, and S. Iijima. Direct evidence for atomic defects in graphene layers. *Nature*, 430(7002):870–873, Aug 2004.
- [13] P. R. Wallace. The band theory of graphite. *Phys. Rev.*, 71(9):622–634, May 1947.
- [14] J. L. Mañes, F. Guinea, and María A. H. Vozmediano. Existence and topological stability of fermi points in multilayered graphene. *Phys. Rev. B*, 75(15):155424, Apr 2007.
- [15] A. L. Vázquez de Parga, F. Calleja, B. Borca, M. C. G. Passeggi, J. J. Hinarejos, F. Guinea, and R. Miranda. Periodically rippled graphene: Growth and spatially resolved electronic structure. *Phys. Rev. Lett.*, 100(5):056807, Feb 2008.
- [16] F. Guinea, B. Horovitz, and P. Le Doussal. Gauge field induced by ripples in graphene. *Phys. Rev. B*, 77(20):205421, May 2008.
- [17] F. Guinea, M. I. Katsnelson, and A. K. Geim. Energy gaps and a zero-field quantum hall effect in graphene by strain engineering. *Nat. Phys.*, 6(1):30–33, Jan 2010.
- [18] S. Choi, S. Jhi, and Y. Son. Effects of strain on electronic properties of graphene. *Phys. Rev. B*, 81(8):081407, Feb 2010.
- [19] V. M. Pereira and A. H. Castro Neto. Strain engineering of graphene’s electronic structure. *Phys. Rev. Lett.*, 103(4):046801, Jul 2009.
- [20] G. Gui, J. Li, and J. Zhong. Band structure engineering of graphene by strain: First-principles calculations. *Phys. Rev. B*, 78(7):075435, Aug 2008.
- [21] V. M. Pereira, A. H. Castro Neto, and N. M. R. Peres. Tight-binding approach to uniaxial strain in graphene. *Phys. Rev. B*, 80(4):045401, 2009.
- [22] O. Hod, V. Barone, J. E. Peralta, and G. E. Scuseria. Enhanced half-metallicity in edge-oxidized zigzag graphene nanoribbons. *Nano Lett.*, 7(8):2295, 2007.
- [23] D. Jiang, B. G. Sumpter, and S. Dai. First principles study of magnetism in nanographenes. *J. Chem. Phys.*, 127(12):124703, 2007.
- [24] E. Kan, Z. Li, J. Yang, and J. G. Hou. Half-Metallicity in Edge-Modified Zigzag Graphene Nanoribbons. *J. Am. Chem. Soc.*, 130(13):4224, 2008.
- [25] L. Pisani, J. A. Chan, B. Montanari, and N. M. Harrison. Electronic structure and magnetic properties of graphitic ribbons. *Phys. Rev. B*, 75(6):064418, 2007.

- [26] Y. Son, M. L. Cohen, and S. G. Louie. Energy gaps in graphene nanoribbons. *Phys. Rev. Lett.*, 97(21):216803, 2006.
- [27] Katsunori W., Manfred S., and Mitsutaka F. Spin wave mode of edge-localized magnetic states in nanographite zigzag ribbons. *J. Phys. Soc. Jap.*, 67(6):2089, 1998.
- [28] J. Atalaya, A. Isacsson, and J. M. Kinaret. Continuum elastic modeling of graphene resonators. *Nano Lett.*, 8(12):4196, 2008.
- [29] R. M. Ribeiro, V. M. Pereira, N. M. R. Peres, P. R. Briddon, and A. H. Castro Neto. Strained graphene: tight-binding and density functional calculations. *New J. Phys.*, 11(11):115002, 2009.
- [30] G. Savini, Y.J. Dappe, S. Oeberg, J.-C. Charlier, M.I. Katsnelson, and A. Fasolino. Bending modes, elastic constants and mechanical stability of graphitic systems. *Carbon*, 49(1):62 – 69, 2011.
- [31] N. Stander, B. Huard, and D. Goldhaber-Gordon. Evidence for Klein Tunneling in Graphene p-n Junctions. *Phys. Rev. Lett.*, 102(2):026807, Jan 2009.
- [32] A. F. Young and P. Kim. Quantum interference and klein tunnelling in graphene heterojunctions. *Nat. Phys.*, 5(3):222–226, Mar 2009.
- [33] M. I. Katsnelson, K. S. Novoselov, and A. K. Geim. Chiral tunnelling and the Klein paradox in graphene. *Nat. Phys.*, 2(9):620–625, Sep 2006.
- [34] M. I. Katsnelson. Zitterbewegung, chirality, and minimal conductivity in graphene. *Eur. Phys. J. B*, 51:157–160, 2006.
- [35] R. V. Gorbachev, A. S. Mayorov, A. K. Savchenko, D. W. Horsell, and F. Guinea. Conductance of p-n-p Graphene Structures with “Air-Bridge” Top Gates. *Nano Lett.*, 8(7):1995–1999, 2008.
- [36] O. Klein. Die Reflexion von Elektronen an einem Potentialsprung nach der relativistischen Dynamik von Dirac. *Z. Phys*, 53:157–165, 1929.
- [37] Y Zhang, Y-W Tan, H L. Stormer, and P Kim. Experimental observation of the quantum Hall effect and Berry’s phase in graphene. *Nature*, 438(7065):201–204, Nov 2005.
- [38] F. Miao, S. Wijeratne, Y. Zhang, U. C. Coskun, W. Bao, and C. N. Lau. Phase-Coherent Transport in Graphene Quantum Billiards. *Science*, 317(5844):1530–1533, 2007.
- [39] J. Tworzydło, B. Trauzettel, M. Titov, A. Rycerz, and C. W. J. Beenakker. Sub-Poissonian Shot Noise in Graphene. *Phys. Rev. Lett.*, 96(24):246802, Jun 2006.

- [40] A. W. W. Ludwig, M. P. A. Fisher, R. Shankar, and G. Grinstein. Integer quantum hall transition: An alternative approach and exact results. *Phys. Rev. B*, 50(11):7526–7552, Sep 1994.
- [41] K. Nomura and A. H. MacDonald. Quantum transport of massless dirac fermions. *Phys. Rev. Lett.*, 98(7):076602, Feb 2007.
- [42] Y. Zhang, V. W. Brar, C. Girit, A. Zettl, and M. F. Crommie. Origin of spatial charge inhomogeneity in graphene. *Nat. Phys.*, 5(10):722–726, Oct 2009.
- [43] X. Du, I. Skachko, A. Barker, and E. Y. Andrei. Approaching ballistic transport in suspended graphene. *Nat. Nano.*, 3(8):491–495, Aug 2008.
- [44] E. H. Hwang, S. Adam, and S. Das Sarma. Carrier transport in two-dimensional graphene layers. *Phys. Rev. Lett.*, 98(18):186806, May 2007.
- [45] J. Martin, N. Akerman, G. Ulbricht, T. Lohmann, J. H. Smet, K. von Klitzing, and A. Yacoby. Observation of electron-hole puddles in graphene using a scanning single-electron transistor. *Nat. Phys.*, 4(2):144–148, Feb 2008.
- [46] A. D. Mirlin, F. Evers, I. V. Gornyi, and P. M. Ostrovsky. Anderson Transitions: Criticality, Symmetries and Topologies. *Int. J. Mod. Phys. B*, 24(12-13):1577–1620, MAY 20 2010.
- [47] J. H. Bardarson, J. Tworzydło, P. W. Brouwer, and C. W. J. Beenakker. One-parameter scaling at the dirac point in graphene. *Phys. Rev. Lett.*, 99(10):106801, Sep 2007.
- [48] P. Markoš and L. Schweitzer. Critical regime of two-dimensional ando model: relation between critical conductance and fractal dimension of electronic eigenstates. *J. Phys. A: Mathematical and General*, 39(13):3221, 2006.
- [49] P. M. Ostrovsky, I. V. Gornyi, and A. D. Mirlin. Conductivity of disordered graphene at half filling. *The European Physical Journal - Special Topics*, 148:63–72, 2007. 10.1140/epjst/e2007-00226-4.
- [50] P. M. Ostrovsky, I. V. Gornyi, and A. D. Mirlin. Quantum criticality and minimal conductivity in graphene with long-range disorder. *Phys. Rev. Lett.*, 98(25):256801, Jun 2007.
- [51] P. M. Ostrovsky, I. V. Gornyi, and A. D. Mirlin. Interaction-induced criticality in z_2 topological insulators. *Phys. Rev. Lett.*, 105(3):036803, Jul 2010.
- [52] J. E. Moore. The birth of topological insulators. *Nature*, 464(7286):194–198, Mar 2010.
- [53] B.L. Altshuler, A.G. Aronov, In: A.L. Efros, and M. Pollak (Eds.). *Electron - Electron Interactions in Disordered Systems*. Elsevier, 1985. p. 1.

- [54] A. M. Finkelstein. *Sov. Sci. Rev.*, 1(Sect. A 14), 1990.
- [55] R. Gade and F. Wegner. The $n = 0$ replica limit of $u(n)$ and models. *Nucl. Phys. B*, 360(2-3):213 – 218, 1991.
- [56] F. Evers. Electron transport in disordered systems: unconventional Anderson transitions. Habilitationsschrift, August 2005.
- [57] V. M. Pereira, F. Guinea, J. M. B. Lopes dos Santos, N. M. R. Peres, and A. H. Castro Neto. Disorder induced localized states in graphene. *Phys. Rev. Lett.*, 96(3):036801, Jan 2006.
- [58] S. Guruswamy, A. LeClair, and A. W. W. Ludwig. $gl(NN)$ Super-current algebras for disordered Dirac fermions in two dimensions. *Nucl. Phys. B*, 583(3):475 – 512, 2000.
- [59] K. S. Novoselov, Z. Jiang, Y. Zhang, S. V. Morozov, H. L. Stormer, U. Zeitler, J. C. Maan, G. S. Boebinger, P. Kim, and A. K. Geim. Room-Temperature Quantum Hall Effect in Graphene. *Science*, 315(5817):1379, 2007.
- [60] V. P. Gusynin and S. G. Sharapov. Unconventional integer quantum hall effect in graphene. *Phys. Rev. Lett.*, 95(14):146801, Sep 2005.
- [61] P. M. Ostrovsky, I. V. Gornyi, and A. D. Mirlin. Theory of anomalous quantum hall effects in graphene. *Phys. Rev. B*, 77(19):195430, May 2008.
- [62] L. Sheng, D. N. Sheng, F. D. M. Haldane, and L. Balents. Odd-Integer Quantum Hall Effect in Graphene: Interaction and Disorder Effects. *Phys. Rev. Lett.*, 99(19):196802, Nov 2007.
- [63] Y. Zheng and T. Ando. Hall conductivity of a two-dimensional graphite system. *Phys. Rev. B*, 65(24):245420, Jun 2002.
- [64] K. S. Novoselov, E. McCann, S. V. Morozov, V. I. Fal'ko, M. I. Katsnelson, U. Zeitler, D. Jiang, F. Schedin, and A. K. Geim. Unconventional quantum hall effect and berry's phase of 2π in bilayer graphene. *Nat. Phys.*, 2(3):177–180, Mar 2006.
- [65] K. S. Novoselov, A. K. Geim, S. V. Morozov, D. Jiang, M. I. Katsnelson, I. V. Grigorieva, S. V. Dubonos, and A. A. Firsov. Two-dimensional gas of massless Dirac fermions in graphene. *Nature*, 438(7065):197–200, Nov 2005.
- [66] F. Evers and A. D. Mirlin. Anderson transitions. *Rev. Mod. Phys.*, 80(4):1355–1417, Oct 2008.
- [67] M. R. Zirnbauer. Conformal field theory of the integer quantum Hall plateau transition. arXiv:hep-th/9905054v2, May 1999.
- [68] E. Witten. Non-abelian bosonization in two dimensions. *Commun. Math. Phys.*, 92:455–472, 1984. 10.1007/BF01215276.

- [69] F. Evers, A. Mildenberger, and A. D. Mirlin. Multifractality at the quantum hall transition: Beyond the parabolic paradigm. *Phys. Rev. Lett.*, 101(11):116803, Sep 2008.
- [70] H. Obuse, A. R. Subramaniam, A. Furusaki, I. A. Gruzberg, and A. W. W. Ludwig. Boundary multifractality at the integer quantum hall plateau transition: Implications for the critical theory. *Phys. Rev. Lett.*, 101(11):116802, Sep 2008.
- [71] J. T. Chalker and P. D. Coddington. Percolation, quantum tunnelling and the integer hall effect. *J. Phys C: Solid State Physics*, 21(14):2665, 1988.
- [72] K. Slevin and T. Ohtsuki. Critical exponent for the quantum Hall transition. *Phys. Rev. B*, 80(4):041304, Jul 2009.
- [73] A. Punnoose and A. M. Finkel'stein. Metal-insulator transition in disordered two-dimensional electron systems. *Science*, 310(5746):289–291, 2005.
- [74] E. Abrahams, S. V. Kravchenko, and M. P. Sarachik. Metallic behavior and related phenomena in two dimensions. *Rev. Mod. Phys.*, 73(2):251–266, Mar 2001.
- [75] Wanli Li, G. A. Csáthy, D. C. Tsui, L. N. Pfeiffer, and K. W. West. Scaling and universality of integer quantum hall plateau-to-plateau transitions. *Phys. Rev. Lett.*, 94(20):206807, May 2005.
- [76] H. P. Wei, D. C. Tsui, M. A. Paalanen, and A. M. M. Pruisken. Experiments on delocalization and universality in the integral quantum hall effect. *Phys. Rev. Lett.*, 61(11):1294–1296, Sep 1988.
- [77] A. de Visser, L. A. Ponomarenko, G. Galistu, D. T. N. de Lang, A. M. M. Pruisken, U. Zeitler, and D. Maude. Quantum critical behaviour of the plateau-insulator transition in the quantum hall regime. *J. Phys.: Conference Series*, 51(1):379, 2006.
- [78] A.M.M. Pruisken, D.T.N. de Lang, L.A. Ponomarenko, and A. de Visser. Universal scaling results for the plateau-insulator transition in the quantum hall regime. *Solid State Commun.*, 137(10):540 – 544, 2006.
- [79] N. D. Mermin and H. Wagner. Absence of ferromagnetism or antiferromagnetism in one- or two-dimensional isotropic heisenberg models. *Phys. Rev. Lett.*, 17(22):1133–1136, Nov 1966.
- [80] Konstantin V. Emtsev, A. Bostwick, K. Horn, J.s Jobst, Gary L. Kellogg, L. Ley, Jessica L. McChesney, T. Ohta, Sergey A. Reshanov, J. Rohrl, E. Rotenberg, Andreas K. Schmid, D. Waldmann, Heiko B. Weber, and T. Seyller. Towards wafer-size graphene layers by atmospheric pressure graphitization of silicon carbide. *Nat. Mat.*, 8(3):203–207, Mar 2009.

- [81] C. Berger, Z. Song, T. Li, X. Li, A. Y. Ogbazghi, R. Feng, Z. Dai, Alexei N. Marchenkov, Edward H. Conrad, Phillip N. First, and Walt A. de Heer. Ultrathin epitaxial graphite: 2d electron gas properties and a route toward graphene-based nanoelectronics. *J. Phys. Chem. B*, 108(52):19912–19916, 2004.
- [82] C. Berger, Z. Song, X. Li, X. Wu, N. Brown, Cécile Naud, D. Mayou, T. Li, J. Hass, Alexei N. Marchenkov, Edward H. Conrad, Phillip N. First, and Walt A. de Heer. Electronic Confinement and Coherence in Patterned Epitaxial Graphene. *Science*, 312(5777):1191–1196, 2006.
- [83] Y.-M. Lin, C. Dimitrakopoulos, K. A. Jenkins, D. B. Farmer, H.-Y. Chiu, A. Grill, and Ph. Avouris. 100-GHz Transistors from Wafer-Scale Epitaxial Graphene. *Science*, 327(5966):662, 2010.
- [84] F. Varchon, R. Feng, J. Hass, X. Li, B. Ngoc Nguyen, C. Naud, P. Mallet, J.-Y. Veuillen, C. Berger, E. H. Conrad, and L. Magaud. Electronic structure of epitaxial graphene layers on sic: Effect of the substrate. *Phys. Rev. Lett.*, 99(12):126805, Sep 2007.
- [85] L. Vitali, C. Riedl, R. Ohmann, I. Brihuega, U. Starke, and K. Kern. Spatial modulation of the dirac gap in epitaxial graphene. *Surface Science*, 602(22):L127 – L130, 2008.
- [86] Zhihong C., Yu-Ming L., Michael J. Rooks, and Phaedon A. Graphene nanoribbon electronics. *Physica E: Low-dimensional Systems and Nanostructures*, 40(2):228 – 232, 2007. International Symposium on Nanometer-Scale Quantum Physics.
- [87] N. Rosenkranz, M. Mohr, and C. Thomsen. Uniaxial strain in graphene and armchair graphene nanoribbons: An ab initio study. *Ann. der Phys.*, 523(1-2):137–144, 2011.
- [88] F. Guinea, B. Horovitz, and P. Le Doussal. Gauge fields, ripples and wrinkles in graphene layers. *Solid State Commun.*, 149(27-28):1140 – 1143, 2009.
- [89] E. Cadelano, P. L. Palla, S. Giordano, and L. Colombo. Nonlinear elasticity of monolayer graphene. *Phys. Rev. Lett.*, 102(23):235502, 2009.
- [90] S. Choi, S. Jhi, and Y. Son. Effects of strain on electronic properties of graphene. *Phys. Rev. B*, 81(8):081407, 2010.
- [91] D. Garcia-Sanchez, A. M. van der Zande, A. San Paulo, B. Lassagne, P. L. McEuen, and A. Bachtold. Imaging mechanical vibrations in suspended graphene sheets. *Nano Lett.*, 8(5):1399, 2008.
- [92] O. Hod and G. E. Scuseria. Electromechanical properties of suspended graphene nanoribbons. *Nano Lett.*, 9(7):2619, 2009.

- [93] C. Lee, X. Wei, J. W. Kysar, and J. Hone. Measurement of the elastic properties and intrinsic strength of monolayer graphene. *Science*, 321(5887):385–388, July 2008.
- [94] Q. Lu, M. Arroyo, and R. Huang. Elastic bending modulus of monolayer graphene. *J. Phys. D: Appl. Phys.*, 42(10):102002 (6pp), 2009.
- [95] C. D. Reddy, A. Ramasubramaniam, V. B. Shenoy, and Y. Zhang. Edge elastic properties of defect-free single-layer graphene sheets. *Appl. Phys. Lett.*, 94(10):101904, 2009.
- [96] C. C. Chen, W. Bao, J. Theiss, C. Dames, C. N. Lau, and S. B. Cronin. Raman spectroscopy of ripple formation in suspended graphene. *Nano Lett.*, 2009.
- [97] T. M. G. Mohiuddin, A. Lombardo, R. R. Nair, A. Bonetti, G. Savini, R. Jalil, N. Bonini, D. M. Basko, C. Galiotis, N. Marzari, K. S. Novoselov, A. K. Geim, and A. C. Ferrari. Uniaxial strain in graphene by raman spectroscopy: G peak splitting, grüneisen parameters, and sample orientation. *Phys. Rev. B*, 79(20):205433, 2009.
- [98] C. Casiraghi, A. Hartschuh, H. Qian, S. Piscanec, C. Georgi, A. Fasoli, K. S. Novoselov, D. M. Basko, and A. C. Ferrari. Raman spectroscopy of graphene edges. *Nano Lett.*, 9, 2009.
- [99] A. C. Ferrari, J. C. Meyer, V. Scardaci, C. Casiraghi, M. Lazzeri, F. Mauri, S. Piscanec, D. Jiang, K. S. Novoselov, S. Roth, and A. K. Geim. Raman spectrum of graphene and graphene layers. *Phys. Rev. Lett.*, 97(18):187401, 2006.
- [100] Z. H. Ni, T. Yu, Y. H. Lu, Y. Y. Wang, Y. P. Feng, and Z. X. Shen. Uniaxial strain on graphene: Raman spectroscopy study and band-gap opening. *ACS Nano*, 2(11):2301, 2008.
- [101] J. E. Proctor, E. Gregoryanz, K. S. Novoselov, M. Lotya, J. N. Coleman, and M. P. Halsall. High-pressure raman spectroscopy of graphene. *Phys. Rev. B*, 80(7):073408, 2009.
- [102] G. Tsoukleri, J. Parthenios, K. Papagelis, R. Jalil, A. C. Ferrari, A. K. Geim, K. S. Novoselov, and C. Galiotis. Subjecting a graphene monolayer to tension and compression. *Small*, 5:2397–2402, 2009.
- [103] S. Reich, H. Jantoljak, and C. Thomsen. Shear strain in carbon nanotubes under hydrostatic pressure. *Phys. Rev. B*, 61(20):R13389, 2000.
- [104] S. Bera, A. Arnold, F. Evers, R. Narayanan, and P. Wölfle. Elastic properties of graphene flakes: Boundary effects and lattice vibrations. *Phys. Rev. B*, 82(19):195445, Nov 2010.

- [105] L. Landau and E. Lifshitz. *Theory of Elasticity, Vol 7*. Pergamon Press, 1959.
- [106] Reinhart Ahlrichs, Michael Bär, Marco Häser, Hans Horn, and Christoph Kölmel. Electronic structure calculations on workstation computers: The program system turbomole. *Chem. Phys. Lett.*, 162(3):165 – 169, 1989.
- [107] A. D. Becke. Density-functional exchange-energy approximation with correct asymptotic behavior. *Phys. Rev. A*, 38(6):3098–3100, Sep 1988.
- [108] J. P. Perdew. Density-functional approximation for the correlation energy of the inhomogeneous electron gas. *Phys. Rev. B*, 33(12):8822–8824, Jun 1986.
- [109] J. P. Perdew, K. Burke, and M. Ernzerhof. Generalized gradient approximation made simple. *Phys. Rev. Lett.*, 77(18):3865–3868, Oct 1996.
- [110] J. P. Perdew and Y. Wang. Accurate and simple analytic representation of the electron-gas correlation energy. *Phys. Rev. B*, 45(23):13244–13249, Jun 1992.
- [111] A. D. Becke. Density-functional thermochemistry. iii. the role of exact exchange. *J. Chem. Phys.*, 98(7):5648–5652, 1993.
- [112] A. Schäfer, H. Horn, and R. Ahlrichs. Fully optimized contracted gaussian basis sets for atoms li to kr. *J. Chem. Phys.*, 97(4):2571–2577, 1992.
- [113] P. Koskinen, S. Malola, and H. Häkkinen. Self-passivating edge reconstructions of graphene. *Phys. Rev. Lett.*, 101:115502, 2008.
- [114] C. K. Gan and D. J. Srolovitz. First-principles study of graphene edge properties and flake shapes. *Phys. Rev. B*, 81:125445, 2010.
- [115] S. Jun. Density-functional study of edge stress in graphene. *Phys. Rev. B*, 78:073405, 2008.
- [116] N. Mounet and N. Marzari. First-principles determination of the structural, vibrational and thermodynamic properties of diamond, graphite, and derivatives. *Phys. Rev. B*, 71(20):205214, May 2005.
- [117] K. V. Zakharchenko, M. I. Katsnelson, and A. Fasolino. Finite temperature lattice properties of graphene beyond the quasiharmonic approximation. *Phys. Rev. Lett.*, 102(4):046808, 2009.
- [118] M. Arroyo and T. Belytschko. Finite crystal elasticity of carbon nanotubes based on the exponential cauchy-born rule. *Phys. Rev. B*, 69(11):115415, 2004.
- [119] Konstantin N. Kudin, G. E. Scuseria, and B. I. Yakobson. *c2f*, *bn*, and *c* nanoshell elasticity from ab initio computations. *Phys. Rev. B*, 64(23):235406, 2001.

- [120] R. Faccio, P. A. Denis, H. Pardo, C. Goyenola, and Á. W. Mombrú. Mechanical properties of graphene nanoribbons. *J. Phys.: Cond. Mat.*, 21:285304, 2009.
- [121] R. C. Weast and M. J. Astle. *CRC Handbook of Chemistry and Physics*. CRC press, New York, 89 edition, 2009.
- [122] O. L. Blakslee, D. G. Proctor, E. J. Seldin, G. B. Spence, and T. Weng. Elastic constants of compression-annealed pyrolytic graphite. *J. Appl. Phys.*, 41(8):3373–3382, 1970.
- [123] A. Bosak, M. Krisch, M. Mohr, J. Maultzsch, and C. Thomsen. Elasticity of single-crystalline graphite: Inelastic x-ray scattering study. *Phys. Rev. B*, 75(15):153408, 2007.
- [124] A. Fasolino, J. H. Los, and M. I. Katsnelson. Intrinsic ripples in graphene. *Nat. Mat.*, 6:858, 2007.
- [125] G. M. Odegard, T. S. Gates, L. M. Nicholson, and K. E. Wise. Equivalent-continuum modeling of nano-structured materials. *Compos. Sci. Technol.*, 62(14):1869 – 1880, 2002.
- [126] Y. Shi, K. K. Kim, A. Reina, M. Hofmann, L. Li, and J. Kong. Work function engineering of graphene electrode via chemical doping. *ACS Nano*, 4(5):2689–2694, 2010. PMID: 20433163.
- [127] Y. Yu, Y. Zhao, S. Ryu, L. E. Brus, K. S. Kim, and P. Kim. Tuning the graphene work function by electric field effect. *Nano Lett.*, 9(10):3430–3434, 2009. PMID: 19719145.
- [128] P. Deglmann and F. Furche. Efficient characterization of stationary points on potential energy surfaces. *J. Chem. Phys.*, 117(21):9535–9538, 2002.
- [129] P. Deglmann, F. Furche, and R. Ahlrichs. An efficient implementation of second analytical derivatives for density functional methods. *Chem. Phys. Lett.*, 362(5-6):511 – 518, 2002.
- [130] C. Thomsen, S. Reich, and P. Ordejón. Ab initio determination of the phonon deformation potentials of graphene. *Phys. Rev. B*, 65(7):073403, 2002.
- [131] E. Mariani and F. von Oppen. Flexural phonons in free-standing graphene. *Phys. Rev. Lett.*, 100(7):076801, Feb 2008.
- [132] A. L. C. Pereira and P. A. Schulz. Additional levels between landau bands due to vacancies in graphene: Towards defect engineering. *Phys. Rev. B*, 78(12):125402, Sep 2008.

- [133] O. V. Yazyev and L. Helm. Defect-induced magnetism in graphene. *Phys. Rev. B*, 75(12):125408, Mar 2007.
- [134] O. V. Yazyev. Magnetism in disordered graphene and irradiated graphite. *Phys. Rev. Lett.*, 101(3):037203, Jul 2008.
- [135] O. V. Yazyev. Emergence of magnetism in graphene materials and nanostructures. *Rep. Prog. Phys.*, 73(5):056501, 2010.
- [136] V. Haefner. Wave-packet dynamics and density of states of disordered graphene. Diploma Thesis, KIT, 2011.
- [137] P. M. Ostrovsky, M. Titov, S. Bera, I. V. Gornyi, and A. D. Mirlin. Diffusion and criticality in undoped graphene with resonant scatterers. *Phys. Rev. Lett.*, 105(26):266803, Dec 2010.
- [138] V. M. Pereira, J. M. B. Lopes dos Santos, and A. H. Castro Neto. Modeling disorder in graphene. *Phys. Rev. B*, 77(11):115109, Mar 2008.
- [139] J. T. Chalker, N. Read, V. Kagalovsky, B. Horovitz, Y. Avishai, and A. W. W. Ludwig. Thermal metal in network models of a disordered two-dimensional superconductor. *Phys. Rev. B*, 65(1):012506, Dec 2001.
- [140] A. Mildenberger, F. Evers, A. D. Mirlin, and J. T. Chalker. Density of quasi-particle states for a two-dimensional disordered system: Metallic, insulating, and critical behavior in the class-d thermal quantum hall effect. *Phys. Rev. B*, 75(24):245321, Jun 2007.
- [141] S. Yuan, H. De Raedt, and M. I. Katsnelson. Modeling electronic structure and transport properties of graphene with resonant scattering centers. *Phys. Rev. B*, 82(11):115448, Sep 2010.
- [142] E. Anderson, Z. Bai, C. Bischof, S. Blackford, J. Demmel, J. Dongarra, J. Du Croz, A. Greenbaum, S. Hammarling, A. McKenney, and D. Sorensen. *LAPACK Users' Guide*. Society for Industrial and Applied Mathematics, Philadelphia, PA, third edition, 1999.
- [143] I.S. Burmistrov, S. Bera, F. Evers, I.V. Gornyi, and A.D. Mirlin. Wave function multifractality and dephasing at metal-insulator and quantum Hall transitions. *Ann. of Phys.*, 326(6):1457 – 1478, 2011.
- [144] B. Karmakar, M. R. Gokhale, A. P. Shah, B. M. Arora, D. T. N. de Lang, A. de Visser, L. A. Ponomarenko, and A. M. M. Pruisken. The effects of macroscopic inhomogeneities on the magnetotransport properties of the electron gas in two dimensions. *Physica E: Low-dimensional Systems and Nanostructures*, 24(3-4):187 – 210, 2004.

- [145] R. T. F. van Schaijk, A. de Visser, S. M. Olsthoorn, H. P. Wei, and A. M. M. Pruisken. Probing the plateau-insulator quantum phase transition in the quantum hall regime. *Phys. Rev. Lett.*, 84(7):1567–1570, Feb 2000.
- [146] Wanli Li, C. L. Vicente, J. S. Xia, W. Pan, D. C. Tsui, L. N. Pfeiffer, and K. W. West. Scaling in plateau-to-plateau transition: A direct connection of quantum hall systems with the anderson localization model. *Phys. Rev. Lett.*, 102(21):216801, May 2009.
- [147] Wanli Li, J. S. Xia, C. Vicente, N. S. Sullivan, W. Pan, D. C. Tsui, L. N. Pfeiffer, and K. W. West. Crossover from the nonuniversal scaling regime to the universal scaling regime in quantum hall plateau transitions. *Phys. Rev. B*, 81(3):033305, Jan 2010.
- [148] B. Kramer, S. Kettemann, and T. Ohtsuki. Localization in the quantum hall regime. *Physica E: Low-dimensional Systems and Nanostructures*, 20(1-2):172 – 187, 2003. Proceedings of the International Symposium @'Quantum Hall Effect: Past, Present and Future.
- [149] S. A. Trugman. Localization, percolation, and the quantum hall effect. *Phys. Rev. B*, 27(12):7539–7546, Jun 1983.
- [150] H. Saleur and B. Duplantier. Exact determination of the percolation hull exponent in two dimensions. *Phys. Rev. Lett.*, 58(22):2325–2328, Jun 1987.
- [151] G.V. Mil'nikov and I.M. Sokolov. Semiclassical localization in a magnetic field. *Pis'ma Zh. Eksp. Teor. Fiz.*, 48(9):494–497, 1986.
- [152] B. Kramer, T. Ohtsuki, and S. Kettemann. Random network models and quantum phase transitions in two dimensions. *Phys. Reps.*, 417(5-6):211–342, 2005.
- [153] R. Klesse and M. Metzler. Universal multifractality in quantum Hall systems with long-range disorder potential. *Euro. Phys. Lett.*, 32(3):229, 1995.
- [154] S. Bera, I. Kondov, and F. Evers. Highly efficient numerical implementation of Chalker-Coddington network model and applications, 2010. Accepted as paper in the proceedings of the Workshop SimLab@KIT 2010, Karlsruhe.
- [155] D. Lee and Z. Wang. Effects of electron-electron interactions on the integer quantum hall transitions. *Phys. Rev. Lett.*, 76(21):4014–4017, May 1996.
- [156] B. Huckestein. Scaling theory of the integer quantum hall effect. *Rev. Mod. Phys.*, 67(2):357–396, Apr 1995.
- [157] F. Hohls, U. Zeitler, and R. J. Haug. High frequency conductivity in the quantum hall regime. *Phys. Rev. Lett.*, 86(22):5124–5127, May 2001.

- [158] F. Hohls, U. Zeitler, and R. J. Haug. Hopping conductivity in the quantum hall effect: Revival of universal scaling. *Phys. Rev. Lett.*, 88(3):036802, Jan 2002.
- [159] S. Koch, R. J. Haug, K. v. Klitzing, and K. Ploog. Size-dependent analysis of the metal-insulator transition in the integral quantum Hall effect. *Phys. Rev. Lett.*, 67(7):883–886, Aug 1991.
- [160] F. J. Dyson. Statistical Theory of the Energy Levels of Complex Systems. I. *J. Math. Phys.*, 3(1):140–156, 1962.
- [161] E. P. Wigner. On a class of analytic functions from the quantum theory of collisions. *Ann. of Math.*, 53(1):pp. 36–67, 1951.
- [162] R. Gade. Anderson localization for sublattice models. *Nucl. Phys. B*, 398(3):499 – 515, 1993.
- [163] A. Altland and M. R. Zirnbauer. Nonstandard symmetry classes in mesoscopic normal-superconducting hybrid structures. *Phys. Rev. B*, 55(2):1142–1161, Jan 1997.
- [164] P. W. Anderson. Absence of diffusion in certain random lattices. *Phys. Rev.*, 109(5):1492–1505, Mar 1958.
- [165] E. Abrahams, P. W. Anderson, D. C. Licciardello, and T. V. Ramakrishnan. Scaling theory of localization: Absence of quantum diffusion in two dimensions. *Phys. Rev. Lett.*, 42(10):673–676, Mar 1979.
- [166] K. B. Efetov, A. I. Larkin, and D. E. Khmel'nitskii. *Zh. Eksp. Teor. Fiz.*, 79:1120, 1980 [Sov. Phys. JETP 52, 568 (1980)].
- [167] F. Wegner. The mobility edge problem: Continuous symmetry and a conjecture. *Z. Phys. B*, 35:207–210, 1979. 10.1007/BF01319839.
- [168] L. Schäfer and F. Wegner. Disordered system with n orbitals per site: Lagrange formulation, hyperbolic symmetry, and goldstone modes. *Z. Phys. B*, 38:113–126, 1980.
- [169] A. M. M. Pruisken. On localization in the theory of the quantized hall effect: A two-dimensional realization of the $[\theta]$ -vacuum. *Nucl. Phys. B*, 235(2):277 – 298, 1984.
- [170] F Evers. The ABC of Density Functional Theory in Theory and Practice. WS 2010/11, Karlsruhe Institute of Technology, 2010-11.
- [171] P. Hohenberg and W. Kohn. Inhomogeneous electron gas. *Phys. Rev.*, 136(3B):B864–B871, Nov 1964.
- [172] W. Kohn and L. J. Sham. Self-consistent equations including exchange and correlation effects. *Phys. Rev.*, 140(4A):A1133–A1138, Nov 1965.

- [173] K. Burke. The ABC of DFT. <http://dft.uci.edu/>, 2007.
- [174] D. M. Ceperley and B. J. Alder. Ground state of the electron gas by a stochastic method. *Phys. Rev. Lett.*, 45(7):566–569, Aug 1980.
- [175] J. P. Perdew and Alex Zunger. Self-interaction correction to density-functional approximations for many-electron systems. *Phys. Rev. B*, 23(10):5048–5079, May 1981.
- [176] J. P. Perdew and W. Yue. Accurate and simple density functional for the electronic exchange energy: Generalized gradient approximation. *Phys. Rev. B*, 33(12):8800–8802, Jun 1986.
- [177] Yu. V. Nazarov. Limits of universality in disordered conductors. *Phys. Rev. Lett.*, 73(1):134–137, Jul 1994.
- [178] S. Ryu, C. Mudry, A. Furusaki, and A. W. W. Ludwig. Landauer conductance and twisted boundary conditions for dirac fermions in two space dimensions. *Phys. Rev. B*, 75(20):205344, May 2007.
- [179] A. Schuessler, P. M. Ostrovsky, I. V. Gornyi, and A. D. Mirlin. Full counting statistics in disordered graphene at the dirac point: From ballistics to diffusion. *Phys. Rev. B*, 82(8):085419, Aug 2010.
- [180] M. Titov, P. M. Ostrovsky, I. V. Gornyi, A. Schuessler, and A. D. Mirlin. Charge transport in graphene with resonant scatterers. *Phys. Rev. Lett.*, 104(7):076802, Feb 2010.
- [181] E. Abrahams, P. W. Anderson, P. A. Lee, and T. V. Ramakrishnan. Quasiparticle lifetime in disordered two-dimensional metals. *Phys. Rev. B*, 24(12):6783–6789, Dec 1981.
- [182] R. B. Lehoucq, D. C. Sorensen, and C. Yang. *ARPACK Users Guide: Solution of Large Scale Eigenvalue Problems by Implicitly Restarted Arnoldi Methods*. Society for Industrial and Applied Mathematics, Philadelphia, PA, 1998.
- [183] P. Amestoy, I. S. Duff, J. L’Excellent, and J. Koster. Mumps: A general purpose distributed memory sparse solver. In *Proceedings of the 5th International Workshop on Applied Parallel Computing, New Paradigms for HPC in Industry and Academia*, PARA ’00, pages 121–130, London, UK, 2001. Springer-Verlag.
- [184] P. R. Amestoy, I. S. Duff, J. Koster, and J.-Y. L’Excellent. A fully asynchronous multifrontal solver using distributed dynamic scheduling. *SIAM Journal on Matrix Analysis and Applications*, 23(1):15–41, 2001.

-
- [185] P. R. Amestoy, A. Guermouche, J.-Y. L'Excellent, and S. Pralet. Hybrid scheduling for the parallel solution of linear systems. *Parallel Computing*, 32(2):136–156, 2006.
- [186] J. Schulze. Towards a tighter coupling of bottom-up and top-down sparse matrix ordering methods. *BIT*, 41(4):800–841, 2001.
- [187] J. Y. L'Excellent. Mumps : a multifrontal massively parallel solver, 2010.
- [188] M. Fournié, N. Renon, Y. Renard, and D. Ruiz. Cfd parallel simulation using getfem++ and mumps. In *Proceedings of the 16th international Euro-Par conference on Parallel processing: Part II*, Euro-Par'10, pages 77–88, Berlin, Heidelberg, 2010. Springer-Verlag.
- [189] L. Grasedyck, W. Hackbusch, and R. Kriemann. Performance of h-lu preconditioning for sparse matrices. *Comp. Methods Appl. Math.*, 8(4):336–349, 2008.
- [190] G. Karypis and V. Kumar. A parallel algorithm for multilevel graph partitioning and sparse matrix ordering. *J. Par. Distr. Comp.*, 48:71–85, 1998.
- [191] G. Karypis, K. Schloegel, and V. Kumar. Parmetis: Parallel graph partitioning and sparse matrixordering library. Technical report, University of Minnesota, Department of Computer Science and Engineering, 1997.
- [192] F. Pellegrini and J. Roman. Scotch: A software package for static mapping by dual recursive bipartitioning of process and architecture graphs. In *Proceedings of HPCN'96, Brussels, Belgium*, volume 1067, pages 493–498. Springer, 1996.

List of publications

- *Elastic properties of graphene flakes: boundary effects and lattice vibrations*, S. Bera, A. Arnold, F. Evers, R. Naryanan and P. Wölfle. arXiv:1003.4429, Phys. Rev. B. **82**, 195445 (2010).
- *Diffusion and criticality in undoped graphene with resonant scatterers*, P. M. Ostrovsky, M. Titov, S. Bera, I. V. Gornyi, A. D. Mirlin. arXiv:1006.3299v1, Phys. Rev. Lett. **105**, 266803 (2010).
- *Wave function multifractality and dephasing at metal-insulator and quantum Hall transition*, I. S. Burmistrov, S. Bera, F. Evers, I. Gornyi and A. D. Mirlin, arxiv:1011.3616, Annals of Physics(N.Y) **326**, 1457(2011).
- *Highly efficient numerical implementation of Chalker-Coddington network model and applications* S. Bera, I. Kondov, and F. Evers., accepted as paper in the proceedings of the Workshop SimLab@KIT 2010, November 29-30, 2010, Karlsruhe.
- *Multifractality of conductance at the integer quantum Hall plateau transition*, H. Obuse, I. A. Gruzberg, S. Bera, F. Evers and A. W. W. Ludwig, preprint.

Acknowledgements

First of all, I want to express my sincere gratitude to my advisor Ferdinand Evers for giving me a chance to work with him for my PhD thesis. This is probably one of the best things that happened to me in my student life. I am eternally grateful for that. Along with this I should also mention about his family, who supported me enormously at my early days in Deutschland and also in course of my stay. Thank you everybody.

I would also like to thank Prof. Alexander Shnirman, who agreed to referee my thesis in a very short time.

Next, let me thank the people with whom I worked in close collaboration during my PhD. First of all I thank Prof. Alexander Mirlin with whom I always enjoyed discussing physics even in the coffee room. I also thank Igor Burmistrov, Igor Gornyi and Pavel Ostrovsky for allowing me to work with them in various different projects. I sincerely thank Rajesh Narayanan for first introducing me to Ferdinand. Since then it has been a great working with Ferdinand and Raj. I thank both of you again.

I would also like to give a special thanks to all our group members at INT. Specially, Alexej, Velimir, Michiel, Stephan, Hideaki, Victor, Arindam, Christian – all of you deserves a special thanks. I have always enjoyed discussing with you people during our group meeting as well as in the lunch time. I thank Ivan Kondov for helping me with numerics and finding me suitable to work with him during my PhD. It has been an excellent collaboration. Special mention goes to Christian Seiler, who painstakingly read all my thesis and helped me to correct it in all details. I also thank Michiel for helping me in this regard as well.

I thank all the members of TKM for providing such a natural atmosphere to work. I especially thank Prof. Peter Wölfle for allowing me to work in this wonderful department. And no acknowledgement will get over without acknowledging Rose. She is the heart of this institute and without whom I would have never been able to finish my PhD in a true sense. From the very first day till today she took care of all the official works that one could ever imagine and helped me throughout. I thank her once more.

Let me also acknowledge the support from CFN, from where I got my funding during my PhD and also for my visit to US. I thank Joel Moore, Berkeley, for allowing me to work with him during my short visit to University of California,

Berkeley. I also acknowledge the support from KHYS, KIT during my visit to US as well.

At last I want to mention my mother for invisibly being with me all the time. Also to my father, who supported me whole heartedly during my PhD. Finally let me thank all my friends, well wishers and my extended family members, whom I did not mention by name, you are not written here, but are always present in my heart and will be present in future as well.